

# Variations on Debris Disks III. Collisional Cascades and Giant Impacts in the Terrestrial Zones of Solar-type Stars

Scott J. Kenyon

*Smithsonian Astrophysical Observatory, 60 Garden Street, Cambridge, MA 02138*

e-mail: skenyon@cfa.harvard.edu

Benjamin C. Bromley

*Department of Physics, University of Utah, 201 JFB, Salt Lake City, UT 84112*

e-mail: bromley@physics.utah.edu

## ABSTRACT

We analyze two new sets of coagulation calculations for solid particles orbiting within the terrestrial zone of a solar-type star. In models of collisional cascades, numerical simulations demonstrate that the total mass, the mass in 1 mm and smaller particles, and the dust luminosity decline with time more rapidly than predicted by analytic models,  $\propto t^{-n}$  with  $n \approx 1.1$ – $1.2$  instead of 1. Size distributions derived from the numerical calculations follow analytic predictions at  $r \lesssim 0.1$  km but are shallower than predicted at larger sizes. In simulations of planet formation, the dust luminosity declines more slowly than in pure collisional cascades, with  $n \approx 0.5$ – $0.8$  instead of  $1.1$ – $1.2$ . Throughout this decline, giant impacts produce large, observable spikes in dust luminosity which last  $\sim 0.01$ – $0.1$  Myr and recur every 1–10 Myr. If most solar-type stars have Earth mass planets with  $a \lesssim 1$ – $2$  AU, observations of debris around 1–100 Myr stars allow interesting tests of theory. Current data preclude theories where terrestrial planets form out of 1000 km or larger planetesimals. Although the observed frequency of debris disks among  $\gtrsim 30$  Myr old stars agrees with our calculations, the observed frequency of warm debris among 5–20 Myr old stars is smaller than predicted.

*Subject headings:* planetary systems – planets and satellites: formation – protoplanetary disks – stars: formation – zodiacal dust – circumstellar matter

## 1. INTRODUCTION

Dense disks of debris surround many main sequence stars (e.g., Backman & Paresce 1993; Wyatt 2008; Matthews et al. 2014). In these systems, particles with radii  $r \approx 1 \mu\text{m}$  to 1 cm and temperatures  $T \approx 50\text{--}500$  K reradiate  $\sim 0.001\%$  to  $1\%$  of the light from the central star. Binary systems are almost as likely to harbor debris disks as apparently single stars (Trilling et al. 2007; Stauffer et al. 2010; Kennedy et al. 2012; Rodriguez & Zuckerman 2012; Rodriguez et al. 2015). Among A-type stars, the frequency of debris disks declines from  $\sim 50\%$  for ages of  $\sim 10$  Myr to  $\lesssim 5\%$  at  $0.5\text{--}1$  Gyr (e.g., Rieke et al. 2005; Currie et al. 2008; Carpenter et al. 2009a). FGK stars have somewhat lower debris disk frequencies of  $10\%$  to  $20\%$ , with excesses that decline more slowly with stellar age (Carpenter et al. 2009a,b; Kennedy & Wyatt 2013; Matthews et al. 2014). Several older stars also appear to have substantial and very luminous disks or rings of debris which may decline rapidly with time (e.g., Song et al. 2005; Rhee et al. 2008; Melis et al. 2010, 2012; Meng et al. 2015).

Debris disks are signposts of planet formation (e.g., Kenyon & Bromley 2002b; Zuckerman & Song 2004; Kenyon & Bromley 2008; Raymond et al. 2011, 2012). In current theory, protoplanets grow through mergers of smaller objects. Once they reach sizes of  $500\text{--}1000$  km, protoplanets stir nearby small objects to large velocities. Continued growth enables stirring over larger and larger volumes, generating a cascade of destructive collisions among small leftovers. This collisional cascade grinds the leftovers into a ring or disk of very small particles with luminosity comparable to the dust luminosities of many debris disks. As the cascade evolves, occasional ‘giant impacts’ between pairs of protoplanets produce clouds of small particles which interact with the rest of the disk (e.g., Agnor et al. 1999; Asphaug et al. 2006; Grigorieva et al. 2007; Genda et al. 2012). In some giant impact models, the dust luminosity roughly matches the very luminous disks associated with old G-type stars.

Interpreting observations of debris disks requires a robust theory of planet formation which predicts the time evolution of luminosity and the structure of solid material from  $\sim 0.1$  AU to beyond  $100$  AU. Analytic approaches specify an initial ensemble of solids with maximum size  $r_{max}$  orbiting the central star at high velocity with eccentricity  $e$ , inclination  $i$  and a range of semimajor axes  $a$  (e.g., Wyatt & Dent 2002; Dominik & Decin 2003; Krivov et al. 2006; Wyatt et al. 2007a,b; Löhne et al. 2008; Kobayashi & Tanaka 2010; Kennedy & Wyatt 2010; Wyatt et al. 2011). For an initial surface density  $\Sigma_0$ , several simplifying assumptions allow these models to predict the time evolution of the size distribution and total mass of the debris. Successful applications include matches to the time evolution of debris disks around A-type and G-type stars (Matthews et al. 2014). However, the approach fails to account for the frequency of giant impacts at late times.

Several numerical approaches place debris disks in the context of the long-term evolution

of a primordial disk of gas and dust (Kenyon & Bromley 2005, 2008, 2010; Weidenschilling 2010a; Raymond et al. 2011, 2012; Kobayashi & Löhne 2014). These studies adopt an initial mass and radial structure for the disk, establish prescriptions for the evolution and interactions of the gas and the solids, and derive  $a$ ,  $e$ ,  $i$ ,  $\Sigma$ , and other properties of the debris as a function of the initial conditions and the final architecture of the planetary system. With an accurate treatment for the long-term evolution of the cascade and the ability to follow dust production from giant impacts at late times, these calculations can match observations of the time evolution of the brightness and frequency of debris disks. However, the cpu intensive nature of this approach often limits their ability to identify how the evolution depends on uncertain input parameters.

Other numerical approaches extract plausible snapshots from detailed planet formation simulations and model a well-defined subset of the system (Grigorieva et al. 2007; Booth et al. 2009; Mustill & Wyatt 2009; Stark & Kuchner 2009; Jackson & Wyatt 2012; Nesvold et al. 2013; Kral et al. 2013). Using  $n$ -body dynamical calculations combined with semi-analytic results, these investigations derive the geometry and luminosity of the debris as a function of time. Aside from learning how these features depend on initial conditions, these investigations excel at matching observations of particular systems. These algorithms are also very cpu intensive and hinge on specifying a fairly small set of initial conditions from a very broad range of possibilities.

Weaving these investigations into a more robust theory for planet formation requires calculations which test and unify the different approaches. Here we consider results from two sets of coagulation calculations for swarms of particles orbiting at 1 AU from a solar-type star. The first set of simulations enables robust tests of analytic models for collisional cascades. The second set allows us to place collisional cascades in context with more detailed planet formation simulations. Comparisons between the two sets yield common features and differences which are useful for interpreting existing observations.

Our study begins in §2 with a brief discussion of the basic predictions of the analytic model. After describing the algorithms used in our numerical simulations (§3), we report outcomes for collisional cascades (§4.1) and the formation of planets (§4.2) at 1 AU. After a brief discussion (§5), we conclude with a short summary (§6). Readers uninterested in the details can skim the background in §2, glance through the figures in §4, read the discussion in §5, and finish with the summaries in §4.3 and §6.

## 2. ANALYTIC MODEL

Building on the collisional cascade models of Dohnanyi (1969) and Hellyer (1970), Wyatt & Dent (2002) and Dominik & Decin (2003) developed analytic models for the long-term collisional evolution of particles in a debris disk. Objects with radius  $r$ , mass  $m$ , and mass density  $\rho$  orbit within a cylindrical annulus with width  $\delta a$  centered at a distance  $a$  from a central star with mass  $M_\star$  and luminosity  $L_\star$ . All particles have the same orbital eccentricity  $e$  and inclination  $i$ . Destructive collisions generate a collisional cascade where the mass in solids gradually diminishes with time. For an upper mass limit  $m_{max}$  of the largest solid objects participating in the cascade, the analytic model yields a simple formula for  $N_{max}(t)$ , the number of these large objects as a function of time. Radiation pressure establishes  $m_{min}$ , a lower mass limit for solids with stable orbits around the central star. Between  $m_{min}$  and  $m_{max}$ , the cascade produces a power-law size distribution,  $N(r) \propto r^{-q}$  (e.g., Dohnanyi 1969; Hellyer 1970; Williams & Wetherill 1994; O’Brien & Greenberg 2003; Kobayashi & Tanaka 2010; Wyatt et al. 2011). Setting the slope  $q$  of this size distribution yields another simple formula for the time evolution of the dust luminosity  $L_d(t)$ .

### 2.1. Time Evolution of the Number Density

To derive expressions for  $N_{max}(t)$  and  $L_d(t)$ , we adopt a particle-in-a-box model, where kinetic theory sets the collision rate (Wyatt & Dent 2002; Dominik & Decin 2003). For an annulus with volume  $V$ , we consider an ensemble of mono-disperse particles with number density  $n_{max} = N_{max}/V$ , collision cross-section  $\sigma = 4\pi r_{max}^2$ , and relative velocity  $v$ . Every collision destroys two particles; the loss rate is  $\dot{N}_{max} = -2N_{max}n_{max}\sigma v$ .

To express this rate in terms of basic disk parameters, we define the initial number of particles  $N_{0,max}$ , initial surface density  $\Sigma_0 = N_{0,max}m_{max}/2\pi a\delta a$ , the vertical height of the annulus  $H$ , and the volume  $V = 4\pi a\delta aH$ . For solids orbiting with angular frequency  $\Omega$ , orbital period  $P = 2\pi/\Omega$ , vertical velocity  $v_z$ , and Keplerian velocity  $v_K$  within the annulus,  $H \approx v_z/\Omega$ ,  $i \approx e/2$ ,  $v_z \approx ev_K/2$ , and  $v \approx ev_K$  (e.g., Wetherill & Stewart 1993; Kenyon & Luu 1998).

We set the collision time as

$$t_c = \frac{r_{max}\rho P}{12\pi\Sigma_0} . \quad (1)$$

In this approach,  $t_c$  is the time to destroy one of the largest particles in the ensemble. Formally, collisions destroy two particles on the time scale  $2t_c$ . The collision rate then becomes

$$\dot{N}_{max} = -N_{max}^2/N_{0,max}t_c , \quad (2)$$

which has a simple solution

$$N_{max}(t) = \frac{N_{0,max}}{1 + t/t_c} . \quad (3)$$

In this derivation, the collision time depends only on properties of the largest objects in the swarm (see also Dominik & Decin 2003). In a real cascade, collisions with smaller particles in the swarm also remove mass from the largest particles (e.g., Wyatt & Dent 2002; Dominik & Decin 2003; Wyatt et al. 2007a,b; Kobayashi & Tanaka 2010; Kennedy & Wyatt 2011; Kennedy et al. 2011; Wyatt et al. 2011). In addition to completely destructive collisions with objects having  $m \gtrsim 0.25 m_{max}$ , cratering collisions with much smaller particles gradually chip away material from the largest objects. These ‘extra’ collisional processes modify the collision time by a factor  $\alpha \lesssim 3$ –4.

To estimate  $\alpha$  for an equilibrium cascade, we adopt results from Kobayashi & Tanaka (2010, and references therein). If  $Q_D^*$  is the collision energy required to eject half the mass from a pair of colliding objects and if  $Q_c$  is the center-of-mass collision energy, the largest object in the debris has mass  $m_l \approx 0.2 (Q_c/Q_D^*)^{-1}$ . For simplicity, we assume  $q \approx 3.5$  for the entire swarm throughout the evolution and for the debris from a single collision. Different choices have little impact on the results (Kobayashi & Tanaka 2010). Using the  $s_1 = 6.3$ ,  $s_2 = 38.1$ , and  $s_3 = 5.6$  parameters defined following eq. 25 of Kobayashi & Tanaka (2010),

$$\alpha \approx 3.6 \left( \frac{v^2}{2Q_D^*} \right)^{-5/6} . \quad (4)$$

For  $(v^2/2Q_D^*) \gg 1$ , eqs. 9–13 of Wyatt et al. (2007a) yield similar results. In most collisional cascades,  $(v^2/2Q_D^*) \gtrsim 4$ ; thus,  $\alpha \lesssim 1.8$  (see also Wyatt et al. 2011).

To complete this discussion, it is useful to estimate the collision time in a swarm of material at 1 AU. For solids with  $\rho = 3 \text{ g cm}^{-3}$  in a disk with  $\Sigma_0 = 10 \text{ g cm}^{-2}$  (comparable to the minimum mass solar nebula; e.g., Weidenschilling 1977; Hayashi 1981; Chiang & Youdin 2010),

$$t_c \approx 8 \times 10^4 \alpha \left( \frac{r_{max}}{100 \text{ km}} \right) \left( \frac{\Sigma_0}{10 \text{ g cm}^{-2}} \right)^{-1} \left( \frac{P}{1 \text{ yr}} \right) \text{ yr} . \quad (5)$$

Collision times are short,  $\sim 0.1$ – $1.0$  Myr for swarms consisting of particles with  $r_{max} \lesssim 100$ – $1000$  km at 1 AU.

## 2.2. Luminosity Evolution

With  $N(t)$  known, the dust luminosity follows. Destructive collisions of the largest objects produce a power-law size distribution extending from the largest objects with mass

$m_{max}$  to the smallest objects with mass  $m_{min}$ . The total mass  $M_d$  and cross-sectional area  $A_d$  of particles within the annulus are simple functions of the minimum size, the maximum size, and the slope  $q$  (e.g., Wyatt & Dent 2002; Dominik & Decin 2003; Kenyon et al. 2014). The stellar energy intercepted by the solids is  $L_d = A_d/4\pi a^2$ . If  $m_{min}$ ,  $m_{max}$ , and  $q$  never change, the initial dust luminosity  $L_{d,0}$  is a simple function of  $N_{max,0}$  and these parameters. The time evolution of the dust luminosity is then:

$$L_d(t) = \frac{L_{d,0}}{1 + t/t_c} . \quad (6)$$

Setting  $r_{min} = 1 \mu\text{m}$  and  $q = 3.5$  for the size distribution for an annulus with  $\delta a = 0.2a$  at 1 AU:

$$L_{d,0} = 7.9 \times 10^{-3} \left( \frac{\rho}{3 \text{ g cm}^{-3}} \right)^{-1} \left( \frac{r_{max}}{100 \text{ km}} \right)^{-1/2} \left( \frac{r_{min}}{1 \mu\text{m}} \right)^{-1/2} \left( \frac{\Sigma_0}{10 \text{ g cm}^{-2}} \right) L_\star . \quad (7)$$

The initial dust luminosity is independent of the collision time.

At late times ( $t \gg t_c$ ),  $L_d(t) \approx L_{d,0}t_c/t$ . Combining  $L_{d,0}$  and  $t_c$  into a new normalization factor  $L'_{d,0}$ ,

$$L_d(t) = L'_{d,0} \left( \frac{t}{1 \text{ Myr}} \right)^{-1} , \quad (8)$$

where

$$L'_{d,0} = 5.6 \times 10^{-4} \alpha \left( \frac{r_{max}}{100 \text{ km}} \right)^{1/2} \left( \frac{r_{min}}{1 \mu\text{m}} \right)^{-1/2} \left( \frac{P}{1 \text{ yr}} \right) L_\star . \quad (9)$$

Despite starting out with much smaller initial dust luminosity, old cascades with large  $r_{max}$  are easier to detect than those with small  $r_{max}$  (Wyatt 2008; Kobayashi & Tanaka 2010). At late times, the ability to detect a cascade is independent of the initial mass involved in the cascade. Through the parameter  $\alpha$ , the dynamics of the swarm also set the detectability.

### 2.3. Deriving $r_{min}$ and $r_{max}$

Maintaining a power-law size distribution for particles with  $m_{min} \lesssim m \lesssim m_{max}$  requires destructive collisions among roughly equal mass objects<sup>1</sup>. For impact velocity  $v$ ,  $Q_c = \mu v^2/2(m_1 + m_2)$ , where  $\mu = m_1 m_2/(m_1 + m_2)$  is the reduced mass for a pair of colliding

---

<sup>1</sup>Although cratering can also drive a cascade, the largest objects then probably grow with time. For simplicity, we focus here on systems where collisions reduce the masses of all objects. We return to this issue in §4.1.1.

planetesimals with masses  $m_1$  and  $m_2$ . For equal mass objects,  $Q_c = v^2/8$  (see also Wetherill & Stewart 1993; Williams & Wetherill 1994; Tanaka et al. 1996; Stern & Colwell 1997; Kenyon & Luu 1999; O’Brien & Greenberg 2003; Kobayashi & Tanaka 2010).

Following standard practice,

$$Q_D^* = Q_b r^{\beta_b} + Q_g \rho_p r^{\beta_g} \quad (10)$$

where  $Q_b r^{\beta_b}$  is the bulk component of the binding energy and  $Q_g \rho_p r^{\beta_g}$  is the gravity component of the binding energy (e.g., Benz & Asphaug 1999; Leinhardt et al. 2008; Leinhardt & Stewart 2009). For rocky objects,  $Q_b \approx 3 \times 10^7 \text{ erg g}^{-1} \text{ cm}^{-\beta_b}$ ,  $\beta_b \approx -0.40$ ,  $Q_g \approx 0.3 \text{ erg g}^{-2} \text{ cm}^{3-\beta_g}$ , and  $\beta_g \approx 1.35$  (see also Davis et al. 1985; Holsapple 1994; Love & Ahrens 1996; Housen & Holsapple 1999; Ryan et al. 1999; Arakawa et al. 2002; Gribbin et al. 2004; Burchell et al. 2005).

Setting  $Q_c \approx Q_D^*$  establishes constraints on the particles destroyed by an adopted collision velocity. For large objects with  $v \approx ev_K$  and  $\beta_g = 1.35$ , collisions destroy equal-mass particles with  $r \lesssim r_{c,max}$ , where

$$r_{c,max} \approx 300 \left( \frac{e}{0.1} \right)^{1.48} \left( \frac{v_K}{30 \text{ km s}^{-1}} \right)^{1.48} \left( \frac{\rho}{3 \text{ g cm}^{-3}} \right)^{-0.74} \left( \frac{Q_g}{0.3 \text{ erg g}^{-1}} \right)^{-0.74} \text{ km} . \quad (11)$$

For small objects,  $\beta_b = -0.4$ ; collisions destroy equal mass objects with  $r \gtrsim r_{c,min}$ , where

$$r_{c,min} \approx 0.02 \left( \frac{e}{0.1} \right)^{-2.5} \left( \frac{v_K}{30 \text{ km s}^{-1}} \right)^{-2.5} \left( \frac{Q_b}{10^7 \text{ erg g}^{-1}} \right)^{2.5} \mu\text{m} . \quad (12)$$

The first relation establishes that objects with  $r \lesssim 300 \text{ km}$  participate in the cascade. Because radiation pressure typically ejects dust grains with  $r \lesssim 1 \mu\text{m}$ , the second relation confirms that all objects smaller than 300 km participate in the cascade. Once the cascade begins, collisions maintain it forever.

Although collisions between equal-mass objects with  $r > r_{c,max}$  result in some net growth of one particle, cratering collisions with the rest of the swarm can gradually reduce the mass of these objects (e.g., Kobayashi & Tanaka 2010). As with estimates of the  $\alpha$  factor for the collision time (eq. 4), deriving the maximum size of particles which slowly lose mass requires integrating the collision rate over the mass distribution. When we examine results of our numerical simulations, we will illustrate how this maximum size depends on the properties of the swarm.

Once the cascade begins, the slope  $q$  of the power-law size distribution depends on the details of the  $Q_D^*$  relation (O’Brien & Greenberg 2003; Kobayashi & Tanaka 2010; Wyatt

et al. 2011). When  $Q_D^*$  is independent of  $r$ ,  $q = 3.5$ . For the standard  $Q_D^*(r)$  in eq. 10, the size distribution consists of two power laws, with  $q_s = (7 - \beta_b/3)/(2 - \beta_b/3) \approx 3.68$  for small particles and  $q_l = (7 + \beta_g/3)/(2 + \beta_g/3) \approx 3.04$  for large particles. The slope of the double power law changes where  $Q_D^*(r)$  reaches a minimum,  $r_Q \approx 0.1$  km for rocky objects with the parameters quoted after eq. 10.

## 2.4. Collisional Cascade at 1 AU

Solving eqs. 3–6 for the long-term evolution of the mass in solids and the dust luminosity requires initial conditions for the central star ( $M_\star$ ,  $L_\star$ ), the geometry of the annulus ( $a$ ,  $\delta a$ ,  $e$ , and  $i$ ), and the properties of the solid particles ( $r_{min}$ ,  $r_{max}$ ,  $N_{0,max}$ ,  $q$ , and  $Q_D^*$ ). To illustrate the long-term evolution, we consider a swarm of solid material orbiting a  $1 M_\odot$  star at 1 AU.

Fig. 1 shows the time evolution of the dust luminosity for particles with  $r_{min} = 1 \mu\text{m}$ , various  $r_{max}$ ,  $\Sigma_0 = 10 \text{ g cm}^{-2}$ ,  $e = 0.1$ ,  $i = e/2$ , and  $\alpha = 1$  orbiting in an annulus with  $\delta a = 0.2$  at  $a = 1$  AU around a central star with  $M_\star = 1 M_\odot$ ,  $L_\star = 1 L_\odot$ . When  $r_{max}$  is 10 km, the initial luminosity is large, but the collision time is short. Within 1 Myr, the luminosity falls by a factor of  $\sim 50$ . After  $\sim 30$  Myr, the relative luminosity falls below  $10^{-5}$ . When  $r_{max}$  is much larger, longer collision times allow the luminosity to remain large at later times. For  $r_{max} = 1000$  km, it takes 30–40 Myr (300–400 Myr) for the relative luminosity to fall below  $10^{-4}$  ( $10^{-5}$ ).

## 3. NUMERICAL MODEL

To perform numerical calculations of collisional cascades, we use *Orchestra*, an ensemble of computer codes for the formation and evolution of planetary systems. In addition to other algorithms, *Orchestra* includes a multiannulus coagulation code which derives the time evolution of a swarm of solid particles orbiting a central object (Kenyon & Bromley 2004a, 2008, 2012). Here, we use the coagulation code to follow the evolution of solids at 1 AU around a solar mass star.

### 3.1. Numerical Grid

To provide the closest representation of the analytic model, we conduct coagulation calculations within a single annulus with semimajor axis  $a$  and width  $\delta a$  around a star with mass  $M_\star = 1 M_\odot$ . Within this annulus, there are  $M$  mass batches with characteristic



mass  $m_k$  and radius  $r_k$  (Spaute et al. 1991; Wetherill & Stewart 1993; Weidenschilling et al. 1997; Kenyon & Luu 1998). Batches are logarithmically spaced in mass, with mass ratio  $\delta \equiv m_{k+1}/m_k$ . Each mass batch contains  $N_k$  particles with total mass  $M_k$  and average mass  $\bar{m}_k = M_k/N_k$ . Particle numbers  $N_k < 10^{15}$  are always integers. Throughout the calculation, the average mass is used to calculate the average physical radius  $\bar{r}_k$ , collision cross-section, collision energy, and other necessary physical variables. As mass is added and removed from each batch, the average mass changes (Wetherill & Stewart 1993).

For any  $\delta$ , numerical calculations lag the result of an ideal calculation with infinite mass resolution (see §A.1). In most cases, simulations with  $\delta = 1.05$ – $1.19$  yield better solutions to the evolution of the largest objects ( $r \gtrsim 1$  km) than calculations with  $\delta = 1.41$ – $2.00$ . Although simulations with  $\delta = 1.05$ – $1.10$  allow better tracking of the gradual reduction in mass of the largest objects during the cascade, the evolution of the size distribution and the dust luminosity is fairly independent of  $\delta$ . Thus, we consider a suite of calculations with  $\delta = 1.19$  ( $= 2^{1/4}$ ).

In this suite of calculations, we follow particles with sizes ranging from a minimum size  $r_{min} = 1 \mu\text{m}$  to the maximum size  $r_{max}$ . The algorithm for assigning material to the mass bins extends the maximum size as needed to accommodate the largest particles. When collisions produce objects with radii  $r < r_{min}$ , this material is lost to the grid.

### 3.2. Initial Conditions

All calculations begin with a swarm of particles with initial maximum size  $r_0$  and mass density  $\rho_p = 3 \text{ g cm}^{-3}$ . These particles have initial surface density  $\Sigma_0$ , total mass  $M_0$ , and horizontal and vertical velocities  $v_{h,0}$  and  $v_{z,0}$  relative to a circular orbit. The horizontal velocity is related to the orbital eccentricity,  $e^2 = 1.6 (v_h/v_K)^2$ , where  $v_K$  is the circular orbital velocity. The orbital inclination is  $\sin i = \sqrt{2}v_z/v_K$ .

For the simulations in this paper, we consider two different initial size distributions for solid objects. To follow the analytic model as closely as possible, one set of calculations begins with a power law size distribution,  $N(r) \propto r^{-q}$  and  $q = 3.5$ . To study whether our calculations produce this equilibrium size distribution, we begin a second set of calculations with a mono-disperse set of particles.

### 3.3. Evolution

The mass and velocity distributions of the solids evolve in time due to inelastic collisions, drag forces, and gravitational encounters. As summarized in Kenyon & Bromley (2004a, 2008), we solve a coupled set of coagulation equations which treats the outcomes of mutual collisions between all particles in all mass bins. We adopt the particle-in-a-box algorithm, where the physical collision rate is  $n\sigma v f_g$ ,  $n$  is the number density of objects,  $\sigma$  is the geometric cross-section,  $v$  is the relative velocity, and  $f_g$  is the gravitational focusing factor (Wetherill & Stewart 1993; Kenyon & Luu 1998). The collision algorithm treats collisions in the dispersion regime – where relative velocities are large – and in the shear regime – where relative velocities are small (Kenyon & Luu 1998; Kenyon & Bromley 2014). Within an annulus, massive protoplanets on nearly circular orbits are ‘isolated’; these objects can collide with smaller objects but cannot collide with other isolated objects (Wetherill & Stewart 1993; Kenyon & Luu 1998; Kenyon & Bromley 2015).

In every time step, our algorithm requires an integral number of collisions  $N_{kl,int}$  between mass bins  $k$  and  $l$ . For each derived  $N_{kl}$ , the algorithm compares the fractional part to a random number drawn for each  $(k, l)$  pair. When the random number exceeds the fractional part,  $N_{kl}$  is rounded down; otherwise  $N_{kl}$  is rounded up. Comparisons with a Runge-Kutta code (which allows fractional particles) and tests on systems with analytic solutions verify this approach (e.g., Kenyon & Luu 1998; Kenyon & Bromley 2015).

For these simulations, we consider two approaches to collision outcomes. Adopting  $Q_D^* = \text{constant}$  allows us to make the most direct comparison with analytic models. Calculations with the more standard  $Q_D^*(r)$  measure the sensitivity of the evolution to changes in  $Q_D^*$  and enable links to other published numerical simulations of collisional cascades. For the rocky solids in this study, we adopt  $Q_b = 3 \times 10^7 \text{ erg g}^{-1} \text{ cm}^{-\beta_b}$ ,  $\beta_b = -0.40$ ,  $Q_g = 0.3 \text{ erg g}^{-2} \text{ cm}^{3-\beta_g}$ , and  $\beta_g = 1.35$ . These parameters are broadly consistent with published analytic calculations and numerical simulations (e.g., Davis et al. 1985; Holsapple 1994; Love & Ahrens 1996; Housen & Holsapple 1999). At small sizes, they agree with results from laboratory experiments (e.g., Ryan et al. 1999; Arakawa et al. 2002; Giblin et al. 2004; Burchell et al. 2005).

For each pair of colliding planetesimals, the mass of the merged planetesimal is

$$m = m_1 + m_2 - m_{esc} , \quad (13)$$

where the mass of debris ejected in a collision is

$$m_{esc} = 0.5 (m_1 + m_2) \left( \frac{Q_c}{Q_D^*} \right)^{b_d} . \quad (14)$$

The exponent  $b_d$  is a constant of order unity (e.g., Davis et al. 1985; Wetherill & Stewart 1993; Kenyon & Luu 1999; Benz & Asphaug 1999; O’Brien & Greenberg 2003; Kobayashi & Tanaka 2010; Leinhardt & Stewart 2012). Here, we consider  $b_d = 1$  and  $9/8$ .

To place the debris in the grid of mass bins, we set the mass of the largest collision fragment as

$$m_{max,d} = m_{l,0} \left( \frac{Q_c}{Q_D^*} \right)^{-b_l} m_{esc} , \quad (15)$$

where  $m_{l,0} \approx 0.01$ – $0.5$  and  $b_l \approx 0$ – $1.25$  (Wetherill & Stewart 1993; Kenyon & Bromley 2008; Kobayashi & Tanaka 2010; Weidenschilling 2010b). When  $b_l$  is large, catastrophic collisions with  $Q_c \gtrsim Q_D^*$  crush solids into smaller fragments. Lower mass objects have a differential size distribution  $N(r) \propto r^{-q_d}$ . After placing a single object with mass  $m_{max,d}$  in an appropriate bin, we place material in successively smaller mass bins until (i) the mass is exhausted or (ii) mass is placed in the smallest mass bin. Any material left over is removed from the grid.

For calculations of collisional cascades, we assume that the orbital  $e$  and  $i$  are constant with time. When we consider how the growth of solids leads to a collisional cascade, we derive orbital evolution due to collisional damping from inelastic collisions and gravitational interactions. For inelastic and elastic collisions, we follow the statistical, Fokker-Planck approaches of Ohtsuki (1992) and Ohtsuki et al. (2002), which treat pairwise interactions (e.g., dynamical friction and viscous stirring) between all objects. We also compute long-range stirring from distant oligarchs (Weidenschilling 1989).

Our solutions to the evolution equations conserve mass and energy to machine accuracy. Typical collisional cascade calculations require a single run on a system with 16–32 cpus; over the  $10^6$  timesteps in a typical 2 Gyr run, calculations conserve mass and energy to better than a part in  $10^{10}$ . Planet formation calculations usually require 3–4 runs on 64 cpus. Over  $10^7$ – $10^8$  timesteps, our calculations conserve mass and energy to better than a part in  $10^7$ .

### 3.4. Other Approaches

Before describing our calculations, it is useful to place our numerical approach in context with other simulations. Starting with Safronov (1969), kinetic approximations to the particle collision rate and Fokker-Planck estimates of velocity evolution have a long history (e.g., Bandermann 1972; Greenberg et al. 1978; Wetherill 1980; Weidenschilling 1980; Greenberg et al. 1984; Ohtsuki & Nakagawa 1988; Wetherill & Stewart 1989; Spaute et al. 1991; Barge & Pellat 1991; Wetherill & Stewart 1993; Kokubo & Ida 1996; Weidenschilling et al. 1997; Grogan et al. 2001; Ohtsuki et al. 2002; Kokubo et al. 2006; Chambers 2008; Morbidelli et al.

2009; Kobayashi & Dauphas 2013; Glaschke et al. 2014; Shannon et al. 2015). In addition to our studies (e.g., Kenyon & Bromley 2002b, 2004a, 2008, 2010), Kobayashi & Tanaka (2010), Weidenschilling (2010b), and Kobayashi & Löhne (2014) follow the evolution of debris disks using a similar set of algorithms. Aside from various details of the implementation – e.g., single annulus (Kobayashi & Tanaka 2010) or multi-annulus (Weidenschilling 2010b) – these coagulation codes are similar to our multi-annulus coagulation code.

Several other techniques adopt the kinetic approximation for collisions but do not allow velocity evolution from gravitational interactions between mass bins. In addition to following the evolution of particle number in specific mass bins, Krivov et al. (2006) track bins in semimajor axis and orbital eccentricity (see also Löhne et al. 2008, 2012; Krivov et al. 2013). In these models, radiation pressure modifies the orbital parameters of grains ejected from collisions of larger particles (e.g., Burns et al. 1979). As an interesting variant of the particle-in-a-box model with discrete mass bins and integral numbers of particles, Gáspár et al. (2012a) derive the time evolution of the differential number density in a single annulus with collision rates inferred from the kinetic approximation. Although this technique does not track variations in  $a$  and  $e$ , Gáspár et al. (2012a) derive the impact of radiation pressure as in Krivov et al. (2006).

A third group of codes employs  $n$ -body techniques to evolve a collection of massless tracer particles (e.g., Grigorieva et al. 2007; Booth et al. 2009; Stark & Kuchner 2009; Jackson & Wyatt 2012; Nesvold et al. 2013; Kral et al. 2013). These codes solve the equations of motion for a swarm of massless tracers responding to the gravity and radiation pressure from a central star and the gravity of a few other massive planets orbiting the central star. These tracers serve as proxies for a mass distribution of particles; the surface density of tracers is input for estimating the collision rates between particles of different masses. Although the algorithms in each implementation are different, aspects of these codes are similar to  $n$ -body-based (e.g., Raymond et al. 2011, 2012; Levison et al. 2012) and hybrid (Weidenschilling et al. 1997; Bromley & Kenyon 2006, 2011a,b, 2013; Glaschke et al. 2014) codes for calculating the formation and evolution of planetary systems.

In this paper, we compare results from single annulus coagulation calculations to predictions of the analytic model (e.g., Wyatt et al. 2011) and (where possible) other numerical calculations using the kinetic approximation (e.g., Krivov et al. 2006; Kobayashi & Tanaka 2010; Gáspár et al. 2012a). Exploring outcomes as a function of  $Q_D^*$ ,  $b_d$ ,  $m_{l,0}$ ,  $b_l$  and  $q_d$  allow us to establish the sensitivity of observable quantities on unknown parameters. These results serve as a foundation for future multi-annulus calculations with tracer particles, which will yield comparisons with  $n$ -body approaches using tracer super-particles (e.g., Grigorieva et al. 2007; Stark & Kuchner 2009; Nesvold et al. 2013; Kral et al. 2013).

## 4. NUMERICAL CALCULATIONS

### 4.1. Collisional Cascades

#### 4.1.1. A Standard Model with Constant $Q_D^*$

To explore the long-term evolution of collisional cascades, we consider a ‘standard’ calculation of solids orbiting a solar-type star. Material with maximum initial radius  $r_0 = 100$  km,  $r_{min} = 1$   $\mu\text{m}$ , and  $\rho = 3$  g cm $^{-3}$  orbits with  $e = 0.1$  and  $i = 0.05$  ( $\approx 3^\circ$ ) inside an annulus with  $a = 1$  AU and  $\delta a = 0.2$  AU. The initial size distribution is either a power law with  $q = 3.5$  or a mono-disperse ensemble with  $r = r_0$ . All objects have a constant  $Q_D^* = 6 \times 10^7$  erg g $^{-1}$ . To assign collisional debris to mass bins, we set  $q_d = 3.5$  and examine results for various combinations of  $b_d$ ,  $m_{l,0}$ , and  $b_l$ . All calculations ignore Poynting-Robertson drag.

For all calculations with constant  $e$  and  $i$ , the size of the largest object gradually declines with time (Fig. 2). The timing of this decline depends on the initial size distribution. When the swarm is initially mono-disperse (upper panel), *all* collisions are catastrophic. As these fairly infrequent collisions produce smaller objects, cratering begins to chip away at the mass in all of the large objects. When the initial size distribution of the swarm is a power-law (lower panel), cratering collisions begin immediately. Thus,  $r_{max}$  initially declines more rapidly for calculations with an initial power law size distribution.

Once  $r_{max}$  begins to decline, the evolution is more dramatic in originally mono-disperse swarms. During the first 0.01–0.1 Myr of evolution, these swarms produce fewer particles with sizes smaller than 1  $\mu\text{m}$  which are lost to the grid. The swarms then have relatively more mass than swarms with an initial power law size distribution. More massive swarms have higher collision rates, resulting in a faster decline of  $r_{max}$  with time.

The time evolution of  $r_{max}$  also depends on the way we distribute debris into the mass bins. When  $b_d = 1$  (9/8), cratering (catastrophic) collisions with  $Q_c \lesssim 1$  ( $Q_c \gtrsim 1$ ) produce relatively more debris. For swarms with a power law size distribution from 1  $\mu\text{m}$  to 100 km, cratering collisions produce more debris than catastrophic collisions. Thus, calculations with  $b_d = 1$  reduce  $r_{max}$  more rapidly than those with  $b_d = 9/8$ . For any  $b_d$ , the mass of the largest object in the debris is smaller in calculations with  $b_l > 0$  than in those with  $b_l = 0$ . Thus,  $r_{max}$  declines more rapidly when  $b_l$  is larger than zero.

For any combination of  $b_d$ ,  $m_{l,0}$ , and  $b_l$ , the dramatic decline in  $r_{max}$  roughly follows a power-law. From  $\sim 1$  Myr to 1 Gyr,  $r_{max} \propto t^{-n}$  with  $n = 0.1$ –0.2. After 100 Myr, particles with  $r_{max} = 100$  km have lost from 97% (power law size distribution,  $b_l = 0$ ) to 99.9% (mono-disperse,  $b_l = 1$ ) of their initial mass.

To describe the evolution of the size distribution, we focus first on results for  $b_d = 1$  and  $b_l = 0$  (Fig. 3–4). Based on previous analyses, we expect a roughly power law size distribution with  $q = 3.5$  from  $1 \mu\text{m}$  to  $r_{max}$ . To minimize shot noise, we derive the cumulative size distribution,  $N(> r)$ , where the predicted slope is  $q_c = 2.5$ . To illustrate deviations from this prediction, we examine the relative cumulative size distribution,  $N(> r)/r^{-2.5}$ . The expected power law slope of this relative size distribution is then  $q_r = q_c - 2.5 = 0$ .

When swarms begin with a power law size distribution, collisional evolution rapidly transforms the system at all sizes (Fig. 3, see also Campo Bagatin et al. 1994). At the smallest sizes, we assume that radiation pressure ejects very small grains with  $r < 1 \mu\text{m}$  from the grid. Compared to a model which includes these very small particles, grains with  $r \approx 1\text{--}10 \mu\text{m}$  experience *fewer* destructive collisions, leading to a clear excess of these particles. With an excess of  $1\text{--}10 \mu\text{m}$  grains, particles with  $r \approx 10\text{--}100 \mu\text{m}$  experience *more* destructive collisions, producing a deficit of these particles (e.g., O’Brien & Greenberg 2003; Kral et al. 2013).

Collisional evolution also leads to excesses and deficits at  $r \gtrsim 1 \text{ km}$ . For  $r \approx 1 \text{ km}$  to  $r_{max}$ , destructive collisions gradually shift mass into lower mass bins. Without a corresponding addition in mass from bins with  $r \gtrsim r_{max}$ , there is a deficit in the mass distribution at  $r \approx r_{max}$ . This deficit enables an excess at smaller sizes,  $r \approx 10 \text{ km}$ .

Among intermediate sized particles ( $100 \mu\text{m}$  to  $1\text{--}3 \text{ km}$ ), there is a small wave about the expected power law. This wave is a function of the deficits and excesses of particles at smaller and larger sizes (see also §A.2; Campo Bagatin et al. 1994; Durda et al. 1998; O’Brien & Greenberg 2003). As cratering reduces the sizes of the largest particles, the peak of the wave at  $5\text{--}20 \text{ km}$  gradually shifts to smaller sizes. Over  $100 \text{ Myr}$ , the shape of the wavy power law remains roughly constant at smaller sizes.

For swarms starting with a mono-disperse size distribution, the system rapidly evolves to the ‘standard’ size distribution (Fig. 4). After  $\sim 0.1 \text{ Myr}$ , the relative size distributions of swarms with initially mono-disperse and power law size distributions are nearly identical from  $1 \mu\text{m}$  to  $10 \text{ km}$ . At  $0.1\text{--}100 \text{ Myr}$ , there is a clear excess of  $10\text{--}100 \text{ km}$  objects which is not visible in calculations starting with a power law size distribution of small objects. In mono-disperse calculations, infrequent collisions among the largest objects prevents reaching the equilibrium size distribution.

Overall, all approaches to fragmentation produce wavy structures in the relative cumulative size distribution (Fig. 5). However, the amplitudes and positions of the waves depend on  $b_d$  and  $b_l$ . When  $b_d = 9/8$  (instead of 1), the deficits at  $10 \mu\text{m}$  and  $10\text{--}30 \text{ km}$  are pronounced but somewhat smaller. Adopting  $b_l = 0.75\text{--}1.0$  reduces the amplitude of the wave

at small sizes but accentuates it at larger sizes.

To conclude this discussion of the standard model, Fig. 6 shows the time evolution of the dust luminosity  $L_d$ . When collisional cascades begin with a mono-disperse swarm of large objects,  $L_d \approx 0$ . As collisions produce small particles,  $L_d$  rises. In models with  $b_l > 0$ , collisions produce and eject small particles more rapidly, leading to a more rapid rise in  $L_d$  but a smaller peak  $L_d$ . Although the dust luminosity at late times depends on  $b_d$ ,  $m_{l,0}$ , and  $b_l$ , all models follow  $L_d \propto t^{-n}$  with  $n \approx 1.1$ – $1.2$ . Thus, the decline is slightly steeper than predicted from the analytic model.

When the cascade starts with a power-law size distribution, the initial  $L_d$  is much larger. As the size distribution establishes the standard wavy power law,  $L_d$  varies slowly before settling in on some constant value which depends on  $b_d$ ,  $m_{l,0}$ , and  $b_l$ . At late times,  $L \propto t^{-n}$  with  $n \approx 1.1$ – $1.2$ . Although the magnitude of  $L_d$  at  $t \gtrsim 1$  Myr is sensitive to the fragmentation parameters,  $L_d$  is independent of the initial size distribution.

#### 4.1.2. Evolution with Different $Q_D^*$

All analytic models for collisional cascades predict that the lifetime depends on the ratio  $v^2/Q_D^*$  (e.g., eq. 4; see also Wyatt et al. 2007a,b; Kobayashi & Tanaka 2010; Wyatt et al. 2011). In our numerical approach, collisions between pairs of equal mass particles with  $v^2/8Q_D^* \gtrsim 1$  convert more than half of the combined mass into debris. To test the analytic model, we consider a suite of calculations with constant  $v$ ,  $Q_D^* = 6 \times 10^7 - 6 \times 10^{10}$  erg g $^{-1}$ , and  $v^2/8Q_D^* = 0.2$ – $200$ . For comparison, eq. 10 with standard parameters for rocky objects predicts  $Q_D^* \approx 10^6$  erg g $^{-1}$  for 0.1 km particles.

Fig. 7 illustrates the evolution of  $r_{max}$  for calculations with  $b_d = 1$ ,  $m_{l,0} = 0.2$ ,  $b_l = 1$ , and either a mono-disperse (upper panel) or a power-law (lower panel) initial size distribution. When  $v^2/8Q_D^* \lesssim 1$ , the largest objects grow to sizes of 500–1000 km in 10–100 Myr. For larger ratios,  $v^2/8Q_D^* \approx 1$ – $200$ , catastrophic and cratering collisions gradually reduce the size of the largest objects.

The time scale for the largest objects to lose mass depends on  $Q_D^*$  and the initial size distribution. In this set of calculations, the loss time scales inversely with  $Q_D^*$  for  $v^2/8Q_D^* \approx 5$ – $200$ . For smaller  $v^2/8Q_D^*$ , the evolution time is fairly independent of  $Q_D^*$ . For any  $Q_D^*$ , swarms with an initial power-law size distribution begin to lose mass more rapidly than those with an initial mono-disperse set of large objects. At late times, however, originally mono-disperse swarms lose more mass (see §4.1.1).

Despite the different loss rates, all of these calculations yield nearly identical relative cumulative size distributions after 10–100 collision times. Systems with large  $Q_D^*$  tend to have somewhat smaller waves than those with smaller  $Q_D^*$ . Otherwise, the level and shape of the relative cumulative size distributions simply scale with the collision time.

Fig. 8 demonstrates that the evolution of the dust luminosity also scales with  $Q_D^*$ . When swarms begin with a power law size distribution, they have substantial  $L_d$ . Destructive collisions among mono-disperse swarms gradually build a comparable  $L_d$  over a few collision times. For this suite of calculations, the peak  $L_d$  is fairly independent of the ratio  $v^2/8Q_D^*$ .

At late times, all systems follow power law declines in  $L_d$  with time. Setting  $L_d \propto t^{-n}$ , this suite of calculations has  $n = 1.1$ – $1.2$ . There is some tendency for larger  $n$  at early times and smaller  $n$  at late times, but our sample size is too small to verify this behavior.

Throughout this evolution, systems with longer collision times have larger  $L_d$ . For  $v^2/8Q_D^* \gtrsim 10$ – $20$ ,  $L_d \propto (v^2/8Q_D^*)^{-1/2}$ . When  $v^2/8Q_D^* \approx 1$ – $5$ ,  $L_d \propto (v^2/8Q_D^*)^{-1}$ . Once  $v^2/8Q_D^* \lesssim 1$ , most of the solid mass ends up in large objects with negligible surface area. The dust luminosity is then close to zero.

When  $Q_D^*$  is independent of radius, all collisions either allow objects to grow (large  $Q_D^*$ ) or produce debris (small  $Q_D^*$ ). In real systems,  $Q_D^*$  is a function of particle size with a distinct minimum at intermediate sizes  $r \approx 10$ – $100$  m. To illustrate the evolution of  $r_{max}$  in a real system, we consider standard calculations using the  $Q_D^*$  relation in eq. 10.

Fig. 9 shows results of calculations for initially mono-disperse and power-law size distributions with  $b_d = 1$ ,  $m_{l,0} = 0.2$ ,  $b_l = 1$ , and  $r_0 = 100, 300, 500$ , and  $1000$  km. In swarms with a starting  $r_0 = 100$  km and  $300$  km, the largest objects slowly lose mass with time. Systems with smaller  $r_{max}$  evolve more rapidly and lose  $\sim 97\%$  ( $r_0 = 100$  km) to  $70\%$  ( $r_0 = 300$  km) of their original mass over  $1$  Gyr. As in §4.1.1, swarms with power-law size distributions evolve more rapidly than those with mono-disperse size distributions at early times. At later times, the mono-disperse swarms evolve more rapidly.

When  $r$  is larger than  $300$  km, collisions among equal mass objects produce larger merged objects. The evolution is then very sensitive to the starting size distribution of the swarm. Among originally mono-disperse swarms, the largest objects reach sizes of  $4500$ – $6000$  km fairly independently of the initial  $r_{max}$ . In swarms with  $r_0 = 500$  km and a power law size distribution, cratering collisions are almost frequent enough to prevent growth. After  $\sim 10$  Myr, growth overcomes cratering, but the largest objects only reach sizes of  $1000$ – $1500$  km instead of  $4000$ – $5000$  km. For swarms with a larger  $r_0$ , cratering is much less important (Fig. 9, purple curves).



These results follow from eq. 11. Among mono-disperse swarms, we expect growth when  $r_0$  exceeds 300 km; our numerical results confirm this estimate. When swarms start with a power-law size distribution, cratering collisions should prevent growth at some larger  $r_0$ . The numerical calculations suggest this limit is roughly 400 km.

Compared to ‘normal’ collisional cascades, systems where particles grow have much smaller  $L_d$  (Fig. 10). In mono-disperse swarms, the time scale for  $L_d$  to rise from zero scales with  $r_0$ . When the largest objects cannot grow, collisions distribute debris among smaller objects. Peak  $L_d$  is then fairly independent of  $r_0$  (e.g., Fig. 10, thick orange and magenta lines). In ensembles of growing large objects, collisions gradually concentrate more and more mass into larger and larger objects. Growth limits debris production. Peak  $L_d$  is then much smaller (e.g., Fig. 10, thick green and violet lines). At late times, the largest objects sweep up *all* of the remaining small particles;  $L_d$  then drops dramatically.

Systems with initial power-law size distributions exhibit similar behavior (Fig. 10, thin lines). All swarms begin with large  $L_d$ . As collisions destroy the largest objects ( $r_0 = 100$  km and 300 km),  $L_d$  slowly declines with time. At late times ( $t \gtrsim 10$  Myr), the evolution of  $L_d$  is independent of the initial size distribution. When the largest particles grow with time ( $r_0 = 500$  km and 1000 km), all collisions produce some debris; continuous debris production maintains a slow decline in  $L_d$ . Eventually growth dominates debris production;  $L_d$  then plummets. For  $r_0 = 1000$  km, the substantial fall in  $L_d$  begins at  $\sim 300$  Myr (somewhat later than the drop at  $\sim 100$  Myr for a mono-disperse system). When  $r_0 = 500$  km, a close balance between growth and debris production maintains large  $L_d$  past 1–2 Gyr. After a few more Gyr, the largest objects sweep up debris and  $L_d$  rapidly falls to zero.

Despite the different evolution in  $r_{max}$  and  $L_d$ , calculations with  $Q_D^*(r)$  still produce wavy size distributions about a standard power-law (Fig. 11). For the fragmentation parameters adopted here, the expected power law has slope  $q_c \approx 2.68$  (§2.3). The relative cumulative size distribution is then  $n(> r)/r^{-2.68}$ . Independent of the initial size distribution,  $b_d$ ,  $m_{l,0}$ , and  $b_l$ , model results for  $r \lesssim 0.1$  km follow this power law fairly closely, with the usual large excess of small particles and small amplitude waves at 0.01 cm to 0.1 km.

At large sizes ( $r \gtrsim 0.1$  km), model size distributions have a much shallower slope (see also §A.2; Wyatt et al. 2011). For ensembles with  $r_0 = 100$  km, cumulative size distributions at 10–100 Myr roughly follow a power-law from 0.1 km to 30–50 km with  $n(> r) \propto r^{-q_c}$  and  $q_c \approx 1.7$ –1.9 ( $q_r \approx -1.0$  to  $-0.8$ ). Oscillations about this power law have maxima at 1–3 km and minima at 10–40 km.

#### 4.1.3. Evolution with Different $q_d$

In Figs. 2–6, the evolution of the cascade clearly depends on the algorithms for deriving the amount of debris and for placing this debris in mass bins. To examine how the size distribution of the debris impacts the evolution, we consider calculations with a mono-disperse initial size distribution,  $b_d = 1$ ,  $m_{l,0} = 0.2$ ,  $b_l = 1$ , and  $q_d = 3.0, 3.5, 4.0, 4.5$ , and  $5.0$ . When  $q_d$  is small (large), most of the debris lands in bins with smaller (larger) average mass. Based on results from the standard model, we expect the pace of the cascade to depend on  $q_d$ .

Fig. 12 shows the time evolution of  $r_{max}$  as a function of  $q_d$ . For an initially mono-disperse size distribution, catastrophic collisions between the largest objects place debris throughout the mass grid. When  $q_d \approx 3$ , debris is concentrated among the smallest particles; collisions remove more mass from the grid. When  $q_d \approx 5$ , debris is concentrated among the largest particles with little mass lost from the grid. Concentrating more debris among large particles enables a larger rate of mass loss from the largest objects. Thus,  $r_{max}$  declines more rapidly when  $q_d = 5$  than when  $q_d = 3$ .

By the end of the calculation at 1 Gyr, catastrophic and cratering collisions substantially reduce the mass in the largest objects. When  $q_d = 3$  (5),  $r_{max} = 8$  km (6 km). Most of this reduction occurs during the first 1 Myr of the evolution. Once most of the mass in the grid has been converted into  $1 \mu\text{m}$  or smaller particles which are lost to the grid, the time variation of  $r_{max}$  is slow.

For each of these calculations, it takes roughly 0.1 Myr to reach the ‘standard’ wavy power-law size distribution. By 1 Myr, calculations with different  $q_d$  establish various wavy patterns at small particle sizes (Fig. 13). These patterns remain fixed for the rest of the evolution. When  $q_d = 3.5$ , there is a characteristic pattern of a large-amplitude wave at  $1\text{--}100 \mu\text{m}$ , several waves with diminishing amplitude at larger sizes, and a final wave of modest amplitude at  $r \lesssim r_{max}$  (see also Campo Bagatin et al. 1994; Durda et al. 1998; O’Brien & Greenberg 2003; Kral et al. 2013). For other values of  $q_d$ , the pattern for  $r \gtrsim 0.1\text{--}1$  cm is similar. At smaller sizes, however, there are a set of waves with smaller amplitude and shorter wavelength. Although the amplitudes of these waves appear to depend on  $q_d$ , the wavelengths seem independent of  $q_d$ .

Despite these curious differences in the size distribution at small sizes, the mass in the grid is a simple function of  $q_d$ . At a fixed time, cascades with larger  $q_d$  have less mass throughout the grid than cascades with smaller  $q_d$ . The origin of this result is clear. When  $q_d$  is small (large), collisions place more mass in smaller (larger) mass bins. Smaller particles remove less mass from the largest particles, which contain most of the mass in the grid. By

the end of the calculations at 1 Gyr, cascades with  $q_d = 3$  have 35% to 40% more mass than cascades with  $q_d = 5$ .

These calculations also reveal interesting differences in the evolution of the relative dust luminosity  $L_d$  as a function of  $q_d$  (Fig. 14). At the onset of the cascade, infrequent and random collisions (e.g., shot noise) set the population of the small particles which contain most of the surface area. Thus, the timing of the abrupt rises in  $L_d$  is random and fairly independent of  $q$ . During this phase of evolution, however, cascades with small  $q_d$  lose more mass from the grid than cascades with large  $q_d$ . Once cascades establish the ‘standard’ size distribution, those with smaller  $q_d$  have less mass than those with larger  $q_d$ . Thus, the peak  $L_d$  is smaller in systems with smaller  $q_d$ . This difference is substantial: cascades with  $q_d = 5$  are 2.5 times brighter at peak  $L_d$  than cascades with  $q_d = 3$ .

The timing of maximum  $L_d$  also depends on  $q_d$ . When  $q_d$  is large, erosion of the largest particles is more rapid (Fig. 7). More rapid erosion tends to produce a larger ensemble of small particles. Thus, cascades with large  $q_d$  reach maximum  $L_d$  earlier than cascades with small  $q_d$ . This conclusion is independent of the timing of the first rise in  $L_d$ . In Fig. 8, the calculation with  $q_d = 4$  rises before those with  $q_d = 4.5$  or 5, but still reaches a smaller maximum  $L_d$ .

At late times,  $L_d$  also correlates with  $q_d$ . Systems with larger  $q_d$  have larger  $L_d$  at late times. Although somewhat counterintuitive, this outcome has a simple physical explanation. When  $q_d$  is large, more erosion of the largest particles yields a larger maximum  $L_d$  with a somewhat smaller total mass. Cascades with smaller masses and larger  $q_d$  evolve more slowly (due to fewer collisions) and retain debris for somewhat longer (due to larger  $q_d$ ). Thus, these systems tend to maintain their larger  $L_d$  at later times.

In all calculations,  $L_d$  declines somewhat more rapidly than predicted by the analytic model. Our results follow  $L_d \propto t^{-n}$  with  $n = 1.1$ – $1.2$  instead of the analytic  $n = 1$ . The slow decline of  $r_{max}$  with time is responsible for this difference. When  $r_{max}$  is fixed as in the analytic model,  $n$  must be unity as outlined in §2. When  $r_{max}$  declines with time, the collision time becomes progressively shorter with time (eq. 1). As the collision time becomes shorter, the luminosity declines more rapidly.

#### 4.1.4. Model Comparisons

Our analysis suggest several clear differences between predictions of the standard analytic model and the results of numerical simulations with  $Q_D^* = \text{constant}$  (Figs. 2–8, 12–14). For material orbiting with  $e = 0.1$  inside an annulus with  $\Sigma = 10 \text{ g cm}^{-2}$  at 1 AU, (i) the

radius (mass) of the largest object declines by a factor of 12–16 (2000–4000) in 1 Gyr, (ii) the size distribution is a power law which generally follows the  $N(r) \propto r^{-3.5}$  of the analytic model but has large amplitude waves at large and small sizes, and (iii) the evolution of the luminosity at late times is somewhat steeper than the predicted  $L_d \propto t^{-1}$ .

When  $Q_D^*$  is a function of  $r$ , the numerical calculations provide other tests of the analytic model. For  $e = 0.1$  and  $i/e = 0.5$  at  $a = 1$  AU, swarms with  $r_0 = 100$ –400 km follow the evolution of the constant  $Q_D^*$  models fairly closely. Over 2 Gyr, (i) the largest objects lose from 75% to 99% of their initial mass and (ii) the dust luminosity declines as  $L_d \propto t^{-n}$  with  $n \approx 1.1$ –1.2. At late times, the size distribution for  $r \lesssim r_Q = 0.1$  km roughly tracks a power law with the  $q \approx 3.68$  predicted by the analytic model. Dynamical ejection of particles with  $r \lesssim 1 \mu\text{m}$  leads to an excess (deficit) of particles with  $r \approx 1$ –10  $\mu\text{m}$  (10–100  $\mu\text{m}$ ). Among larger particles with  $r \gtrsim r_Q$ , the power law slope is smaller and has a broader range,  $q \approx 2.7$ –2.9, relative to the predicted  $q \approx 3.04$ . With no supply of debris from much larger particles with  $r \gtrsim r_0$ , there are large-amplitude waves about the average power law at large sizes.

Calculations with  $r_0 = 500$ –1000 km evolve differently. When  $e \approx 0.1$ , the largest particles grow with nearly every collision. Although collisions remove mass from smaller particles, growth concentrates the debris from these collisions into the largest objects. Thus, the mass (dust luminosity) of the swarm declines more slowly (rapidly) with time. For this set of calculations, the mass (luminosity) varies with time as  $M_d \propto t^{-n}$  with  $n \lesssim 0.2$  ( $L_d \propto t^{-n}$  with  $n \approx 1.5$ –2.5). Although these results allow no test of the analytic model, they provide useful context for the planet formation calculations in §4.2.

To evaluate other results in the context of a specific analytic model, we consider the size distribution, the mass in small particles, the mass loss rate through the grid, and the dust luminosity in more detail. In analytic models for collisional cascades, each range of sizes loses mass at the same rate which declines as  $\dot{M} \propto t^{-2}$  (e.g., Kobayashi & Tanaka 2010; Wyatt et al. 2011). This behavior allows the cascade to maintain an invariant size distribution. In our calculations, the shape of the size distribution is nearly fixed in time (Fig. 3–4), matching a basic prediction of the analytic model.

When  $Q_D^* = \text{constant}$  over a finite range of particle sizes, analytic models predict a set of waves superposed on a power-law size distribution (Wyatt et al. 2011). Our calculations match the predicted slope and the amplitude of the primary wave close to the small size cutoff at 1  $\mu\text{m}$  (see §A.2). The numerical simulations produce (i) waves with longer wavelengths and smaller amplitudes at 0.1 mm to 1 km and (ii) a larger wave at 1–100 km which are not present in the analytic model.

When  $Q_D^*$  is a function of radius, the numerical calculations match (i) the predicted slope of the power law from  $1\ \mu\text{m}$  to  $0.1\ \text{km}$ , (ii) the amplitude of the wave at the smallest sizes, (iii) the distinctive rise in the relative cumulative size distribution at  $0.1\ \text{km}$ , and (iv) the general shape of the relative size distribution from  $0.1\ \text{km}$  to  $10\text{--}30\ \text{km}$  (see §A.2). However, the level of waviness at  $0.1\ \text{mm}$  to  $0.1\ \text{km}$  is larger than predicted; the slope of the size distribution for  $r \gtrsim 0.1\ \text{km}$  is shallower than predicted.

Overall, this good level of agreement is encouraging. The gradual reduction in the sizes of the largest objects probably produces differences between the analytic model and the simulations at the largest sizes. We suspect that cratering collisions change the level of waviness at smaller sizes. We plan to investigate these possibilities in future studies.

The mass in  $1\ \text{mm}$  and smaller particles provides another test (e.g., Wyatt et al. 2011, and references therein). We define the relative dust mass  $\xi$  as the ratio of the mass in small particles to the total mass. In models with fixed  $Q_D^*$ ,  $r_0 = 100\ \text{km}$ ,  $r_{\min} = 1\ \mu\text{m}$ , and  $q = 3.5$ ,  $\xi = 10^{-4}$ . When  $Q_D^*$  is a function of particle size,  $q = 3.68$  (3.04) for  $r \lesssim r_Q$  ( $r \gtrsim r_Q$ ); with  $r_Q = 0.1\ \text{km}$ ,  $\xi \approx 10^{-4}$ .

Fig. 15 illustrates the behavior of  $\xi$  for a set of cascade models with  $r_0 = 100\ \text{km}$ . When the swarm has an initial power law size distribution,  $\xi \approx 10^{-4}$ . As systems with constant  $Q_D^*$  evolve (Fig. 15, thin black and green curves), the relative dust mass gradually grows with time and reaches  $\xi \approx 2 - 3 \times 10^{-4}$  at  $t = 1\text{--}2\ \text{Gyr}$ . When  $Q_D^*$  is a function of particle size (thin orange and magenta lines),  $\xi$  declines to  $2 - 3 \times 10^{-5}$  at  $0.1\text{--}1\ \text{Myr}$  and then slowly recovers to  $4 - 8 \times 10^{-5}$  at  $t = 1\text{--}2\ \text{Gyr}$ . Swarms with mono-disperse initial size distributions follow similar paths. Once collisions begin to produce dust, the relative dust mass grows to  $\xi \approx 10^{-4}$  (for constant  $Q_D^*$  swarms) or  $\xi \approx 2 - 3 \times 10^{-5}$  (for swarms with  $Q_D^*(r)$ ). The relative dust mass then grows slowly with time.

For swarms with constant  $Q_D^*$ , gradual reductions in  $r_{\max}$  explain the evolution of the relative dust mass. After  $1\text{--}2\ \text{Gyr}$  of evolution,  $r_{\max} \approx 6\text{--}10\ \text{km}$ . For a system with  $q = 3.5$ , the expected relative dust mass is  $\xi \approx 3 - 4 \times 10^{-4}$ . Allowing for small differences in dust mass and total mass due to the wavy size distribution (Fig. 5), the  $\xi \approx 2 - 3 \times 10^{-4}$  from our calculations is close to the expected value.

When  $Q_D^*$  is a function of  $r$ , the change in the size distribution at large sizes is as important as the reduction of  $r_{\max}$  with time. For swarms with a double power-law size distribution and a break at  $r_Q \approx 0.1\ \text{km}$ ,

$$\xi \approx \left( \frac{4 - q_l}{4 - q_s} \right) \left( \frac{r_d^{4 - q_s}}{r_{\max}^{4 - q_l}} \right) r_Q^{q_s - q_l} , \quad (16)$$

where  $r_d = 1\ \text{mm}$  is the radius of the largest dust particle and  $q_s, q_l$  are the slopes of the size

distribution for large and small particles. In our calculations, the slope of the size distribution for small particles –  $q_s \approx 3.68$  – is close to expectation. At large sizes, however, the slope is shallower than predicted,  $q_l \approx 2.7$ – $2.9$  instead of  $q_l \approx 3.04$ . The shallower slope lowers the predicted relative dust mass to  $\xi \approx 1 - 4 \times 10^{-5}$  for  $r_{max} = 100$  km and  $\xi \approx 3 - 9 \times 10^{-5}$  for  $r_{max} = 50$  km. Our calculations match these expectations.

For the time evolution of  $\dot{M}$  and  $L_d$  in the analytic model, we derive an estimate for the collision time from eq. 5 with  $\alpha = 1$ . Adjusting  $\alpha$  allows us to match the analytic  $\dot{M}_0 = M_0/t_c$  at  $t = 0$  with the initial production rate for  $1 \mu\text{m}$  and smaller objects from our numerical simulations. This mass loss rate then declines with time as

$$\dot{M} = t_c^{-1} \frac{M_0}{(1 + t/t_c)^2} . \quad (17)$$

Adopting an initial power law size distribution with  $q = 3.5$  for  $Q_D^* = \text{constant}$  and  $r \leq r_{max}$  yields the initial  $L_d$  which then evolves as in eq. 6.

Fig. 16 compares  $\dot{M}$  derived from our baseline calculations with predictions of the analytic model for  $\alpha = 0.01, 0.1$ , and  $1.0$ . At  $t = 0$ , the numerical calculations match the analytic model for  $\alpha \approx 0.1$ . As the calculations proceed, the derived  $\dot{M}$  declines slightly more rapidly than the analytic prediction. By the end of the calculation, the mass loss rate is similar to analytic model predictions for  $\alpha \approx 0.01$ .

To test the analytic model in more detail, we consider a set of calculations with a range in  $Q_D^*$  (e.g., Fig. 7). At late times,  $\dot{M} \approx M_0 t_c t^{-2}$ . From eq. 5,  $t_c \approx t_0 \alpha$  with  $t_0 \approx 8 \times 10^4$  yr. Substituting this result into the expression for  $\dot{M}$  yields  $\alpha \approx \dot{M} t^2 / M_0 t_0$ . Numerical results for  $\dot{M}(t)$  thus yield  $\alpha(t)$ . For models with  $Q_D^* = 6 - 600 \times 10^7 \text{ erg g}^{-1}$ , we infer:

$$\alpha \approx 12 \left( \frac{v^2}{2Q_D^*} \right)^{-1} \left( \frac{t}{1 \text{ Gyr}} \right)^{-0.13} . \quad (18)$$

At  $0.1$ – $1$  Gyr, the numerical calculations evolve roughly 3 times more slowly than the analytic model (e.g., eq. 4) when  $v^2/2Q_D^* \approx 1$  and approximately in step with the analytic model when  $v^2/2Q_D^* \approx 200$ .

In addition to the steady decline, the calculations exhibit clear spikes in the mass loss rate. Stochastic variations in the collision rate cause this behavior. To try to mimic real collisional systems, we require an integral number of collisions every time step. For infrequent collisions between the largest objects, our algorithm rounds a fractional number of collisions down or up to the nearest integer. When the algorithm rounds up, it produces a clear spike in  $\dot{M}$ .

Fig. 17 compares the baseline  $L_d$ 's for the simulations with the analytic model. At early times, the number of small particles in the calculations oscillates about a constant value as

the system establishes an equilibrium size distribution. This constant is a factor of 4–5 larger than the prediction of the analytic model. At  $\sim 0.01$  Myr, the luminosity in the analytic and numerical calculations starts to fall. Because  $L_d$  in the numerical model declines faster than predicted by the analytic model,  $L_d$  from the numerical models eventually falls below the analytic prediction.

In the numerical models, the excess of small particles at  $r \approx r_{min}$  produces the larger  $L_d$ . Although these particles remove larger particles from the size distribution, the excess surface area from the small particles more than compensates for the deficit in surface area at somewhat larger sizes. Thus, the numerical models have larger  $L_d$  than the analytic model.

Despite the spikes in the mass loss rate, the numerical models show no spikes in  $L_d$ . When  $r_{max} \approx 100$ –300 km, every spike in  $\dot{M}$  sprinkles debris throughout the grid, with no impact on the shape of the size distribution and little impact on the total mass in the grid. Thus, there is negligible change in surface area and  $L_d$ . In §4.3, we describe how collisions in systems with larger  $r_{max}$  produce clear spikes in  $L_d$ .

Results for models where  $Q_D^*$  depends on particle size yield similar results. The dust luminosity and the mass loss rate from the grid generally follow the trends established in calculation with constant  $Q_D^*$ : (i) a plateau in  $\dot{M}$  or  $L_d$  followed by a decline and (ii) occasional spikes in  $\dot{M}$  (but not  $L_d$ ) as the system evolves.

## 4.2. Planet Formation

Our analysis pinpoints several clear differences between the analytic model and detailed coagulation calculations of collisional cascades. However, real cascades do not occur in isolation. Within planet formation theory, cascades begin as the gravity of growing or fully-formed planets stirs up surrounding smaller particles (e.g., Kenyon & Bromley 2002b; Mustill & Wyatt 2009). As these systems evolve, the collisional cascade converts a fraction  $f_c$  of these small particles into dust grains which are ejected by radiation pressure from the central star. Massive planets accrete or dynamically eject the rest of the small particles. Deriving  $f_c$  and making a more robust link between the theories of collisional cascades and planet formation requires more detailed sets of calculations.

To begin to make this link, we consider a suite of planet formation calculations. Within a single annulus, the initial swarm consists of a set of mono-disperse particles with total mass  $M_d = 0.5 M_\oplus$ , surface density  $\Sigma_0 = 10 \text{ g cm}^{-2}$ , and initial radius  $r_0 = 10^n$  ( $n = 0, 1, 2, \dots, 8$ ). Particles have  $e_0 = 10^{-5}$  ( $r_0 = 1$ –10 cm),  $10^{-4}$  ( $r_0 = 1$ –100 m),  $10^{-3}$  ( $r_0 = 1$ –10 km),  $10^{-2}$  ( $r_0 = 1$ –100 km), and  $i_0 = e_0/2$ . As particles grow, collisional damping, dynamical

friction, and viscous stirring modify  $e$  and  $i$  for each mass bin. All calculations ignore gas drag and Poynting-Robertson drag.

Although the initial conditions strongly favor growth through mergers, every collision produces a modest amount of debris. To specify the amount and size distribution of the debris, we adopt the standard  $Q_D^*(r)$  relation with parameters specified after eq. 10 and set  $b_d = 1$ ,  $m_{l,0} = 0.2$ , and  $b_l = 1$  in eqs. 14–15. Modest changes in these assumptions have little impact on the results.

To quantify the diversity of outcomes, we perform  $\sim 5$  calculations for each set of initial conditions. Within a set of calculations, each run begins with a different random number seed. During each timestep, *Orchestra* uses a random number generator to decide whether to round up (or down) a fractional number of collisions to an integer. Randomness in the collision rates generates a dispersion in outcomes.

Despite some intrinsic diversity, all calculations follow a standard pattern. Initially, particles grow through mergers. As particles grow, collisional damping and gravitational interactions modify  $e$  and  $i$  for each mass bin. Damping reduces  $e$  and  $i$  for small particles,  $r \lesssim 1\text{--}10$  cm. Dynamical friction transfers orbital kinetic energy from the largest particles to the smallest particles. Once particles have  $r \gtrsim 1\text{--}10$  km, viscous stirring raises  $e$  and  $i$  for all particles.

As  $e$  and  $i$  evolve, the largest particles step through several stages of growth. At the start of each calculation, gravitational focusing factors  $f_g$  are small. Growth is slow and steady. Damping and dynamical friction enhance  $f_g$ , enabling a phase of runaway growth where the largest particles gain mass much more rapidly than smaller particles. Once viscous stirring dominates collisional damping and dynamical friction, gravitational focusing factors for the largest particles drop. Oligarchic growth – where large particles add mass more slowly – begins.

Rising viscous stirring rates also initiate the collisional cascade. Collisions among particles close to the minimum in  $Q_D^*$  – at roughly  $r_Q \approx 0.1$  km – eject copious amounts of debris into the swarm. As viscous stirring continues to raise  $e$  and  $i$  for small particles, collisions destroy particles which are smaller and larger than  $r_Q$ . With  $Q_D^* \propto r^{-0.4}$  for  $r < r_Q$  and  $Q_D^* \propto r^{1.35}$  for  $r > r_Q$ , it is easier for collisions with fixed kinetic energy to destroy particles with  $r \ll r_Q$  than those with  $r \gg r_Q$ . These collisions produce debris with sizes  $r \lesssim 100$  cm.

As the debris accumulates, there are two possible outcomes (Kenyon & Bromley 2015, and references therein). If collisional damping dominates the loss of particles from destructive collisions, small particles have very small  $e$  and  $i$ . Damping then limits the collisional cascade. Large gravitational focusing factors initiate a second phase of runaway growth, where the



largest objects accrete most of the mass in small particles. If damping is ineffective, small particles remain at large  $e$  and  $i$ ; the collisional cascade proceeds unabated.

Fig. 18 illustrates the growth of the largest particles as a function of  $r_0$ . From eq. 1, small particles evolve more rapidly than large particles. The ensemble of 1 cm particles requires less than a year to reach sizes of 30 cm; after another 20 yr, the largest particles have radii of 1 km. By  $\sim 10^4$  yr, the radii of the largest protoplanets surpass  $10^3$  km. As the evolution slows, occasional collisions among these objects eventually yields a single planet with a radius of roughly 6000 km. In contrast, sets of 100 km or 1000 km particles take more than 0.1 Myr for the largest objects to double in mass. Despite the delay, protoplanets still achieve radii of roughly 6000 km on a time scale of 1 Myr.

Throughout this evolution, changes in the relative cumulative size distribution follow a fairly standard pattern (Fig. 19). For a swarm of particles with  $r_0 = 10$  cm, mergers rapidly produce a swarm of particles with  $r \approx 1$ –10 m. The largest particles then begin to grow faster than their smaller counterparts. After  $\sim 100$  yr, the size distribution has three main pieces: (i) an exponential at large sizes, (ii) a plateau at intermediate sizes, and (iii) a debris tail at small sizes. Over the next  $10^4$  yr, the exponential and the small peak at the small size end of the plateau shift to larger and larger sizes. Large particles sweep up the smallest particles, gradually diminishing the population of the debris tail.

From  $\sim 10^4$  yr to  $\sim 10^5$  yr, the system makes a transition from runaway growth to oligarchic growth. During oligarchic growth, the size distribution develops a small rise at  $r \approx 1000$  km. Once viscous stirring raises the velocities of the smallest particles, collisions destroy particles with  $r \approx r_Q \approx 0.1$  km. The relative cumulative size distribution develops a sharp dip at these sizes. Debris from destructive collisions adds mass to the debris tail.

As the evolution proceeds, the largest objects gradually accumulate most of the mass in the annulus. With most mass already concentrated in 1-100 km objects, this behavior produces (i) an abrupt rise in the size distribution from 1000 km to larger sizes and (ii) a smaller plateau at 1–1000 km. For somewhat smaller particles ( $r \gtrsim 1$  cm), stirring continues to raise collision velocities, enabling the destruction of smaller and smaller objects. The minimum in the relative cumulative size distribution expands from 0.01–1 km at 0.1 Myr to 5 cm to 2 km at 1 Myr to 1 cm to 3 km at 10 Myr. The minimum of this dip shifts to smaller sizes and deepens considerably. After  $\sim 100$  Myr, the size distribution consists of a steeply rising piece for  $r \gtrsim 10$  km and a fairly flat piece for  $r \lesssim 10$  km. By 1 Gyr, accretion by 1–2 large objects and destruction by the collisional cascade remove all small particles from the annulus.

The sharp minimum at  $r \approx 1$ –100 m is a newly identified feature in the size distributions

of evolving swarms of particles (Kenyon & Bromley 2015). At the small size end of the minimum, there is a discontinuity where the relative number of particles increases by 2–4 orders of magnitude. This collisional damping front separates the swarm into two distinct velocity regimes at a radius  $r_{damp}$ . Defining  $e_H = (m_{max}/3M_\odot)^{1/3}$  as the Hill eccentricity of the largest object with mass  $m_{max}$ , we express particle eccentricities as

$$e_{rel} = e/e_H . \quad (19)$$

Particles with  $r \gtrsim r_{damp}$  have  $e_{rel} \approx 5\text{--}30$ ; small objects with  $r \lesssim r_{damp}$  have  $e_{rel} \approx 1$ .

This large difference in  $e_{rel}$  between small and large particles tempers the collisional cascade. Although collisions between particles with  $r \gtrsim r_{damp}$  produces substantial debris, collisions among smaller particles often yield larger merged objects. As material cycles between small and large objects, the largest objects accrete solids from both reservoirs. Eventually,  $\sim 90\%$  of the initial mass ends up in the largest objects. The collisional cascade converts only  $\sim 10\%$  of the initial mass into  $1\ \mu\text{m}$  and smaller particles.

Despite significantly different evolution times for systems with different  $r_0$  (Fig. 18), all systems have similar size distributions at 0.1–1 Gyr (Fig. 20). Every swarm has one or two objects which contain nearly all of the mass. For  $r \gtrsim 10\ \text{km}$ , the cumulative size distribution approximately follows a power law with  $N(> r) \propto r^{-q_c}$  and  $q_c \approx 4.0\text{--}4.3$ . At intermediate sizes ( $r \approx 0.1\ \text{cm}$  to  $10\ \text{km}$ ), the cumulative size distribution has a much shallower slope with a waviness that is similar to the size distributions of collisional cascades (e.g., Fig. 5). Among smaller particles with  $r \approx 1\ \mu\text{m}$  to  $1\ \text{cm}$ , the size distributions are steeper with more pronounced waviness. This feature depends on the timing of the last large collision between objects with  $r \gtrsim 100\ \text{km}$ . Systems with more recent large collisions have larger rises to small sizes and more waviness along this rise.

To examine the observable consequences of this evolution, we consider the dust luminosity  $L_d$  (Fig. 21). At early times, growth concentrates mass into objects with smaller surface area;  $L_d$  declines with time. Once the collisional cascade produces sufficient debris,  $L_d$  rises. For systems with  $r_0 \lesssim 0.1\ \text{km}$ , dust production rates rise at  $\sim 10^4\ \text{yr}$ . Among swarms with larger  $r_0$ , the rise in  $L_d$  occurs at progressively later times, reaching  $\sim 1\ \text{Myr}$  when  $r_0 = 100\ \text{km}$  and  $5\text{--}10\ \text{Myr}$  when  $r_0 = 1000\ \text{km}$ .

For our calculations, the peak relative dust luminosity,  $L_d/L_\star \approx 2\text{--}3 \times 10^{-4}$  is relatively independent of  $r_0$ . Close to the peak, stochastic variations in the collision rate produce 50% variations in  $L_d$ . The magnitude of these variations is independent of  $r_0$ . Repeat calculations with identical initial conditions (but different random number seeds) yield similar variations and similar peak  $L_d$ .

When  $r_0 \gtrsim 1000\ \text{km}$ , peak dust luminosity is much smaller. In these systems, most of

the initial mass ends up in protoplanets with  $r \gtrsim 2000$  km which are hard to break. Binary collisions then produce little debris. Within this debris, collisional damping of small objects is negligible. Thus, the collisional cascade grinds all of the debris into small particles which are eventually ejected from the swarm.

After 1–10 Myr, the  $L_d$  for all swarms gradually declines. As the systems decline, fluctuations – including large spikes in  $L_d$  – become more pronounced. The magnitude and frequency of the spikes is independent of  $r_0$ ; however, the spikes are clearly more obvious at later times. Although the overall evolution of  $L_d$  results from countless collisions of 1–100 km objects, binary collisions between 300–1000 km objects produce the large spikes. These giant impact events release dust masses comparable to (and sometimes exceeding) the total dust mass in the rest of the swarm.

With few large objects in the swarm, impact events are rare and random (see also Genda et al. 2015). The typical spacing between large collisions is  $\sim 1$  Myr at 10 Myr and  $\sim 1$  Myr at 100 Myr. Collisions between the largest objects produce more dust but are less common. As summarized in KB05, it takes 25–50 yr for the debris from a giant impact to spread into a ring which merges with the rest of the swarm. As the debris spreads, we expect variations in the emission on time scales of months to years (e.g., Melis et al. 2012; Meng et al. 2012, 2014, 2015). Relative to the long-term evolution of the collisional cascade, the elevated emission from the debris ejected during a single giant impact lasts 0.01–0.1 Myr. At later times, when the mass in the rest of the swarm is relatively small, elevated levels of dust emission last much longer,  $\gtrsim 1$  Myr (see also Genda et al. 2015). Overall, the likelihood of observing a giant impact in the terrestrial zone of any solar-type star is small,  $\lesssim 0.1\%$  to  $0.2\%$  for detecting any dust from a giant impact and  $\lesssim 0.001\%$  of detecting emission within 25–50 yr of the impact. In a large ensemble of stars, however, detecting debris from giant impacts is possible. For example, KB05 estimate that the *Kepler* satellite might identify 1–2 transit events from impact debris during the lifetime of the satellite.

To develop a better understanding of the spikes in  $L_d$ , we define the break radius  $r_{brk}$  as the maximum size for a particle destroyed in a collision between equal mass objects. In our approach,  $Q_c = v^2/8$  is the center of mass collision energy for a pair of equal mass objects and  $Q_D^*$  is the collision energy required to eject half the mass of the colliding pair to infinity. As the largest objects grow, their gravity stirs up smaller objects to larger and larger  $e$  and  $i$ . Particles with larger  $e$  collide with larger velocities. For fixed  $r$ , the ratio  $Q_c/Q_D^*$  grows with time; collisions among pairs of objects with identical  $r$  eject more mass at later times. Fixing  $Q_c/Q_D^* = 1$ , larger collision velocities result in collisions that destroy pairs of objects with larger and larger  $r_{brk}$  as the system evolves.

Fig. 22 shows the time evolution of  $r_{brk}$  for swarms with  $r_0 = 1$  cm to 1000 km. After

$10^4$  yr, all systems follow the same pattern:  $r_{brk}$  gradually grows from roughly 1 km at 0.01 Myr to roughly 1000 km at 10 Myr. After 10 Myr, one or two objects contain nearly all of the mass. Stirring of  $e$  and  $i$  effectively ceases;  $r_{brk}$  remains roughly constant with time.

This behavior has a profound impact on  $L_d$  (Fig. 21). When  $r_{brk}$  is small, every collision among roughly equal mass objects yields a merger (for large objects) or a small amount of debris (for small objects). This debris has little impact on  $L_d$ . As  $r_{brk}$  grows, binary collisions among objects with  $r \approx r_{brk}$  produce more and more debris. At peak  $L_d$ , these collisions cause modest fluctuations in  $L_d$ . As  $L_d$  declines, collisions among larger and larger objects disperse more and more debris, resulting in more prominent spikes in  $L_d$ . By the end of the calculation, giant impacts among 1000 km objects lead to factor of 5–10 changes in  $L_d$ .

Repeat calculations confirm this behavior. Modest changes in  $e_0$  and  $i_0$  have little impact on the results. Over 2 Gyr of evolution, the collisional cascade converts  $10\% \pm 3\%$  of the initial mass into  $1 \mu\text{m}$  and smaller particles. The rest of the initial mass lies in 1–2 large objects with radii of 5000–6000 km. During the early stages of the cascade (0.1–10 Myr), the peak dust luminosity is  $L_d/L_\star \approx 2 - 3 \times 10^{-4}$ . Near peak brightness, factor of 1.5–2 fluctuations in  $L_d$  are typical. For older systems (10–100 Myr), a slow decline in  $L_d$  is occasionally interrupted by factor of 2–10 spikes in the dust luminosity. As collisions destroy larger and larger objects, the amplitudes of these spikes gradually grow with time. After  $\sim 100$  Myr, the dust luminosity drops by several orders of magnitude. The timing of this decline has a broad range, 100–300 Myr, and is fairly independent of  $r_0$  and  $e_0$ .

### 4.3. Summary

Our suite of numerical calculations yields several interesting insights into the evolution of collisional cascades.

For ‘pure’ cascade models with constant  $e$  and  $i$ , we confirm several aspects of the analytic model. Throughout the evolution of systems where  $Q_D^\star$  is independent of  $r$ , the size distribution generally follows the expected  $N(r) \propto r^{-3.5}$ . When  $Q_D^\star$  is a function of  $r$ , the size distribution follows the predicted  $N(r) \propto r^{-3.68}$  for  $r \lesssim r_Q \approx 0.1$  km. For  $r \gtrsim r_Q$ , the typical slope of  $q \approx 2.7$ – $2.9$  is smaller than the analytic result  $q \approx 3.04$ . As in previous studies, the numerical results show a waviness of modest amplitude about these power laws (§A.2, see also Campo Bagatin et al. 1994; O’Brien & Greenberg 2003; Wyatt et al. 2011; Kral et al. 2013).

The long-term evolution of cascades is close to the predictions of the analytic model. In

our calculations, the decline is somewhat faster –  $L_d, M_d \propto t^{-n}$  and  $n = 1.1\text{--}1.2$  – than the analytic solution, where  $L_d, M_d \propto t^{-1}$ . The ratio  $\xi$  of the dust mass to the total mass slowly grows with time,  $\xi \propto t^n$  and  $n = 0.05\text{--}0.15$ . For fixed  $e$  and  $i$ , the collision time scale for the numerical simulations –  $t_c \propto (v^2/2Q_D^*)^{-1}$  – is reasonably close to the analytic result where  $t_c \propto (v/2Q_D^*)^{-5/6}$ .

A major difference between analytic and numerical models for collisional cascades is the evolution of  $r_{max}$ . Analytic models assume constant  $r_{max}$ . In the numerical calculations,  $r_{max}$  either grows ( $v^2/8Q_D^* \lesssim 1$ ) or declines ( $v^2/8Q_D^* \gtrsim 1$ ) with time. After 1 Gyr of evolution, factor of 2–10 changes in  $r_{max}$  are typical. In systems where  $r_{max}$  declines with time, our results yield  $r_{max} \propto t^{-n}$  with  $n = 0.1\text{--}0.2$ . With  $t_c \propto r_{max}$ , we then expect  $L_d \propto t^{-n}$  with  $n = 1.1\text{--}1.2$ . Thus, the gradual decline of  $r_{max}$  with time accounts for the more rapid decline of  $L_d$  with time. A changing  $r_{max}$  is likely responsible for other, more subtle differences between the analytic and numerical model.

Planet formation simulations yield important insights into the onset and evolution of real collisional cascades. At 1 AU, systems of small particles with  $\Sigma_0 \approx 10 \text{ g cm}^{-2}$  evolve into a few large oligarchs in 0.1–1 Myr. The time scale to produce 2000–4000 km oligarchs is fairly independent of  $r_0$ . For  $t \gtrsim 10\text{--}100$  Myr, the size distribution of small particles and the dust luminosity also have little memory of  $r_0$ .

For collisional cascades, the unique feature of planet formation simulations is the steady evolution of  $r_{brk}$ , the maximum particle size destroyed in collisions of equal mass objects. In analytic models,  $r_{brk} = r_{max} = \text{constant}$ . In numerical simulations of planet-forming disks, growing oligarchs gradually stir up the orbits of smaller solid particles;  $r_{brk}$  grows persistently with time. As  $r_{brk}$  evolves, more and more material becomes involved in the collisional cascade. Thus,  $L_d$  and  $M_d$  decline more slowly with time.

The relative dust mass  $\xi$  also evolves differently in planet formation calculations. In cascades with  $r_0 \approx 100\text{--}300$  km,  $\xi$  gradually grows over time (Fig. 15). In cascades with  $r_0 = 500\text{--}1000$  km and in planet formation calculations, the relative dust mass is usually much smaller ( $\xi \approx 10^{-6} - 10^{-5}$ ) and fluctuates by a factor of 2–20 when giant impacts add debris to the swarm. As the largest objects sweep up debris, planet formation calculations exhibit large drops in  $\xi$  which do not occur in cascade calculations.

To focus on observable differences between numerical calculations of planet formation and pure cascades, Fig. 23 compares the evolution of  $L_d/L_\star$  for two collisional cascade calculations and two planet formation calculations. For the cascade calculations, we set  $r_{max} = 100$  km and  $e_0 = 0.1$  (black curve) and  $r_{max} = 1000$  km and  $e_0 = 0.25$  (violet curve). For these cascades, we set the initial mass  $M_0 = 0.05 M_\oplus$ , the mass typically lost from the

planet formation calculations. Tracks for the two planet formation calculations repeat those from Fig. 21 for  $r_0 = 10$  cm (magenta curve) and  $r_0 = 1$  km (cyan curve).

The four sequences show several similarities in the time evolution of  $L_d$ . All have roughly the same peak luminosity,  $L_d/L_\star \approx 1 - 3 \times 10^{-4}$ . The rise time for the 100 km collisional cascade model is similar to rise times for the two planet formation calculations. The large spikes in  $L_d$  for the 1000 km collisional cascade model are similar to those in the two planet formation calculations.

Several differences in the evolution are also apparent. When  $r_{brk} \approx 100$  km in the two planet formation calculations (0.1–1 Myr),  $L_d$  shows significant fluctuations not visible in the collisional cascade calculation with  $r_0 = 100$  km. When  $r_{brk}$  evolves well past 100 km in the planet formation calculations, the decline in  $L_d$  is much slower than in the collisional cascade calculation with  $r_0 = 100$  km. Finally, when the largest object in the planet formation calculations has accreted most of the mass in the annulus,  $L_d$  plummets. In contrast, both collisional cascade calculations maintain a  $t^{-1.1}$  decline for much longer time scales.

## 5. DISCUSSION

### 5.1. Theoretical Issues

To follow the evolution of a swarm of planetesimals into a planetary system, coagulation calculations include a broad set of physical processes (e.g., Greenberg et al. 1978; Wetherill & Stewart 1993; Weidenschilling et al. 1997; Kenyon & Luu 1999; Kenyon & Bromley 2008; Kobayashi et al. 2010; Ormel et al. 2010; Raymond et al. 2011; Glaschke et al. 2014; Shannon et al. 2015; Johansen et al. 2015, and references therein). Modeling each physical process involves several assumptions and choices for various input parameters. Here, we consider how these decisions impact our results and conclusions.

For this study, we ignore interactions between solid particles and a gaseous disk. Although gaseous circumstellar disks are a major component in planet formation models (e.g., Youdin & Kenyon 2013), all analytic models of collisional cascades assume the gas has already dissipated. Neglecting the gas allows us to pinpoint common features in numerical calculations of collisional cascades and planet-forming disks.

Although we consider radiation pressure from the central star to set  $r_{min}$ , we do not include Poynting-Robertson drag. For  $1 \mu\text{m}$  particles at 1 AU, the collision time is shorter than the time scale for Poynting-Robertson drag when  $L_d/L_\star \gtrsim 10^{-7}$  (e.g., Backman & Paresce 1993; Wyatt 2008). In most of the calculations reported here, the dust luminosity

meets this limit.

Unlike several numerical algorithms (e.g., Krivov et al. 2006; Gáspár et al. 2012a; Kral et al. 2013), our calculations also neglect the radiation force on fragments ejected from a collision. Defining  $\beta$  as the ratio of the radiation force to the gravitational force, debris particles have orbits with semimajor axis  $a' = (\frac{1-\beta}{1-2\beta})a$  and eccentricity  $e' = \beta/(1-\beta)$  (e.g., Burns et al. 1979). Unbound particles with  $\beta \gtrsim 1/2$  and  $r \lesssim 1 \mu\text{m}$  leave the swarm on a time scale comparable to the orbital period. For swarms with  $\Sigma = 10 \text{ g cm}^{-2}$  at 1 AU, collisions between bound and unbound particles are rare. Particles with  $\beta \approx 0.08\text{--}0.5$  ( $r \approx 1\text{--}6 \mu\text{m}$ ) remain bound to the central star but lie outside the single annulus in our calculations.

Despite its absence from current analytic models, it is worth estimating the impact of high- $\beta$  particles on our planet formation simulations. With larger  $a$  and  $e$ , these particles have longer lifetimes than particles inside our single annulus (Wyatt et al. 2010). Fewer collisions tend to increase the population of particles with (i)  $r \gtrsim 6 \mu\text{m}$  inside the annulus and (ii)  $r \lesssim 6 \mu\text{m}$  outside the annulus. Despite producing a steeper size distribution at small sizes, the impact on  $L_d$  is probably small (Wyatt et al. 2010). With negligible total mass, the abundance and orbits of this population have little impact on the growth of the largest objects. We plan multiannulus calculations to investigate these possibilities in more detail.

To calculate collisional processes, we specify a variety of parameters for collisional damping, the cross-section, gravitational stirring, and fragmentation. Comprehensive analytic and  $n$ -body calculations verify the algorithms for collisional damping, the collision cross-section, and stirring (e.g., Greenzweig & Lissauer 1990; Spaute et al. 1991; Ohtsuki 1999; Lee 2000; Ohtsuki et al. 2002; Goldreich et al. 2004; Levison & Morbidelli 2007; Kobayashi & Tanaka 2010; Kenyon & Bromley 2015). Within the fragmentation algorithm, we derive material lost from ‘cratering’ and ‘catastrophic disruption’ using the expressions in eq. 10, eqs. 14–15, and a power law size distribution for the debris. For cratering collisions where the mass of one component (the ‘projectile’) is much smaller than the other (the ‘target’), results for the ejected mass agree with detailed analyses of laboratory measurements (see the discussion in §3.2.1 of Kenyon et al. 2014, and references therein). Criteria for catastrophic disruption are consistent with comprehensive  $n$ -body simulations (e.g., Benz & Asphaug 1999; Leinhardt & Stewart 2009, 2012). At present, these algorithms are state-of-the-art.

For cascade models, Fig. 8 illustrates the impact of changing  $Q_D^*$  on the collision time and the dust luminosity. For fixed  $e$  and  $i$ , systems where  $Q_D^*$  is small evolve more rapidly than systems where  $Q_D^*$  is large. Within a suite of planet formation calculations, the impact of  $Q_D^*$  is less dramatic (e.g., Kenyon & Bromley 2008, 2010, 2012). Although small particles with  $r \lesssim 1 \text{ km}$  can be strengthless rubble piles (e.g., Weidenschilling 1994; Asphaug & Benz 1996; Holsapple & Housen 2007), large reductions in  $Q_b$  and  $\beta_b$  probably have little impact

on the evolution (e.g., Kenyon & Bromley 2008). Among larger objects with  $r \gtrsim r_Q$ , self-gravity limits the ability to change  $Q_D^*$  (e.g., Benz & Asphaug 1999; Leinhardt & Stewart 2012). However, even large changes in  $Q_g$  and  $\beta_g$  may not change  $L_d$  significantly (e.g., Kenyon & Bromley 2012).

Once a few large objects contain most of the mass in the annulus, the approximations used in our statistical estimates for collision rates and stirring begin to break down. As the largest protoplanets continue to accrete material from the rest of the swarm, their dynamical interactions become stronger and more chaotic. Among these large objects, our calculations then tend to overestimate the growth rate and underestimate  $e$  and  $i$ .

To avoid these issues in several previous investigations, we promote the largest objects into the  $n$ -body component of *Orchestra*, where we follow the orbits of each large protoplanet (e.g., Kenyon & Bromley 2006; Bromley & Kenyon 2011a; Kenyon & Bromley 2014). In this study, our main focus is on the evolution of the collisional cascade instead of the final orbits of the largest objects. To save cpu time for a broad suite of simulations, we therefore chose not to promote the largest protoplanets. When these protoplanets contain nearly all of the mass, calculations for the rest of the swarm – including the flow of mass from  $r_{brk}$  to  $r_{min}$  and the accretion of small objects by the largest objects – remain accurate. The evolution of the largest objects then have little impact on the evolution of the mass and luminosity of the small particles.

In multiannulus calculations of terrestrial planet formation, promotion into the  $n$ -body code is more important (e.g., Kenyon & Bromley 2006; Raymond et al. 2011, 2012). When protoplanets contain more than half the mass, they undergo a period of chaotic growth where the largest protoplanets scatter smaller objects throughout the terrestrial zone. Giant impacts are then more frequent and occur at higher velocity than in pure coagulation calculations (see also Asphaug et al. 2006; Genda et al. 2015). Thus, our single annulus calculations probably somewhat underestimate the number and magnitude of large spikes in dust luminosity on time scales  $\gtrsim 10$  Myr. Our main conclusion – that the dust luminosity in coagulation calculations declines more slowly than in collisional cascade calculations – is unchanged.

## 5.2. Comparison with Other Calculations

In the past 10–15 yr, there have been many numerical studies of collisional cascades and planet-forming disks using coagulation and related techniques. Most investigations concentrate on the evolution at large distances, 10–200 AU, from the host star (e.g., Kenyon



& Bromley 2002a; Krivov et al. 2006; Thébault & Augereau 2007; Löhne et al. 2008; Gáspár et al. 2013; Kral et al. 2013; Kobayashi & Löhne 2014). Where possible, we compare our results with these studies and the few analyses which focus on the long-term evolution of fairly massive disks in the terrestrial zone.

In systems with large  $v^2/2Q_D^*$  and short  $t_c$ , the linear decline of mass with time is a basic feature of the analytic model for collisional cascades (e.g., Wyatt & Dent 2002; Dominik & Decin 2003; Wyatt 2008; Kobayashi & Tanaka 2010). Aside from Kobayashi & Tanaka (2010), results from other studies do not test this prediction: the largest objects (i) are allowed to grow or (ii) have very long collision times (e.g., Krivov et al. 2006; Löhne et al. 2008; Gáspár et al. 2012b, 2013; Kral et al. 2013).

For all of our calculations, the disk mass declines with time somewhat more rapidly than the analytic prediction:  $M_d \propto t^{-n}$  with  $n = 1.1\text{--}1.2$  instead of 1. In every calculation, catastrophic and cratering collisions slowly reduce the size of the largest objects. As the radius of the largest objects grows smaller, the collision time also decreases (eq. 1). Shorter collision times speed up the evolution, resulting in a larger mass loss rate per unit time. Thus, the slow reduction in  $r_{max}$  produces a faster evolution of  $M_d$ . Calculations with other codes (e.g., Löhne et al. 2008; Kobayashi & Tanaka 2010; Kral et al. 2013) could test this result.

Tests of the variation of  $t_c$  with  $Q_D^*$  are currently ambiguous. The numerical simulations of Kobayashi & Tanaka (2010) confirm the analytic result,  $t_c \propto (v^2/Q_D^*)^{-5/6}$ . However, Löhne et al. (2008) quote  $t_c \propto (v^2/Q_D^*)^{-9/8}$ . Our result,  $t_c \propto (v^2/Q_D^*)^{-1}$ , lies roughly midway between these two extremes.

All calculations produce wavy size distributions (e.g., Krivov et al. 2006; Löhne et al. 2008; Gáspár et al. 2012b; Kral et al. 2013). For small particles and intermediate mass particles with  $r \lesssim 1$  km, various approaches yield fairly similar results (see also Campo Bagatin et al. 1994; O’Brien & Greenberg 2003). Among larger particles, different treatments of the evolution of the largest particles produce waves with somewhat different amplitudes and positions. However, these differences seem small compared to changes in  $r_{max}$  and the slope of the size distribution as a function of time.

When numerical simulations consider the long-term evolution of objects with  $r \gtrsim 300\text{--}500$  km and  $v^2/8Q_D^* \gtrsim 1$ , giant impacts which release copious amounts of dust are inevitable (e.g., Agnor et al. 1999; Agnor & Asphaug 2004; Genda et al. 2015). The giant impact events in our calculations are similar to those in Weidenschilling (2010a) and Raymond et al. (2011).

To conclude this section, our results for planet formation time scales in the inner solar system are similar to those reported previously (e.g., Kominami & Ida 2002; Kenyon &

Bromley 2004b; Nagasawa et al. 2005; Raymond et al. 2005; Kenyon & Bromley 2006; O’Brien et al. 2006; Kokubo et al. 2006; Chambers 2008; Raymond et al. 2014, and references therein). Typically, it takes  $10^4 - 10^5$  yr to produce lunar mass protoplanets. Collisions combine these objects into a few 3000–6000 km objects over 10–100 Myr. Because we neglect gas drag, our calculations take a factor of  $\sim 2$  longer to form lunar mass objects (e.g., Youdin & Kenyon 2013). Gas drag has little impact on the evolution of 100–1000 km objects; the growth of these objects in our simulations agree with rates established by other investigations.

### 5.3. Observational Issues

Based on a set of multiannulus coagulation calculations at 0.68–1.32 AU, Kenyon & Bromley (2004b, hereafter KB04) first predicted the detectability of warm dust ( $T \approx 200$ –300 K) from terrestrial planet formation. Kenyon & Bromley (2005, hereafter KB05) later described results for a larger disk covering 0.4–2 AU and suggested the possibility of detecting debris ejected from individual giant impacts of 1000 km and larger objects<sup>2</sup>. In these studies, the predicted mid-IR (10–25  $\mu\text{m}$ ) emission from dust reaches a peak relative flux  $F_d/F_\star \approx 10$ –20 at 0.1–1 Myr and gradually falls to  $F_d/F_\star \approx 2$ –3 at  $\sim 10$  Myr. Superimposed on this decline, spikes from giant impacts raise the relative flux by factors of 3–10. Rapid variability of dust production on 1–100 yr time scales is another characteristic of these calculations.

Recent investigations confirm these results (e.g., Weidenschilling 2010a; Raymond et al. 2011, 2012; Jackson & Wyatt 2012; Genda et al. 2015). Once 500–1000 km objects form, destructive collisions produce copious amounts of debris throughout the terrestrial zone. Giant impacts, including those capable of producing the Earth-Moon system, generate additional debris. As the overall level of debris declines, sporadic spikes in emission from the giant impacts become more prominent. At late times, these spikes dominate dust production.

Although the new calculations in §4.2 yield luminous debris disks at 0.1–100 Myr as in KB04 and KB05, the long-term evolution of systems with  $r_0 \lesssim 100$  km is somewhat different. By explicitly following the dynamical evolution of 1  $\mu\text{m}$  to 1 m particles, we now identify an evolutionary phase at 1–10 Myr where collisional damping among mm- and cm-sized particles overcomes viscous stirring by large oligarchs. During this epoch, the lack of destructive collisions among small particles effectively halts the cascade. With a slower cascade, these systems lose a smaller fraction of their initial mass and are 2–3 times fainter at peak brightness than the debris disks in KB04 and KB05. However, the disks also remain brighter for a factor of 2–3 longer, allowing the debris from terrestrial planet formation to

---

<sup>2</sup>KB05 also predicted levels for warm dust emission in the terrestrial zones of A-type stars.

remain detectable among older stars.

Scaling the results of the single 0.9–1.1 AU annulus in §4.2 to the KB05 multiannulus calculations at 0.4–2 AU, the new calculations predict typical peak relative fluxes  $F_d/F_\star \approx 2$ –3 at 10–12  $\mu\text{m}$  and  $F_d/F_\star \approx 3$ –5 at 20–25  $\mu\text{m}$ . Occasional bright spikes from giant impacts can raise the peak flux by a factor of 3–10. Although the bulk emission usually declines below detectable levels at 10–20 Myr, giant impacts occasionally raise the system above current detection limits until  $\sim 100$  Myr (see also Raymond et al. 2011, 2012; Jackson & Wyatt 2012; Genda et al. 2015).

Calculations with  $r_0 \gtrsim 1000$  km yield very different outcomes. Viscous stirring from the largest objects dominates the evolution; collisional damping of small particles is unimportant. Although the largest protoplanets still reach sizes of 4000–6000 km, the dust luminosity always remains very low. The systems are not detectable with *Spitzer* or *WISE*.

Despite the identification of many cold debris disks around solar-type stars, initial attempts to detect warm emission with *IRAS* and ground-based data were discouraging (e.g., Weinberger et al. 2004; Mamajek et al. 2004). Song et al. (2005) then discovered a very luminous debris disk associated with the old field star BD+20° 307. *IRAS* also measured a significant 12  $\mu\text{m}$  excess associated with HD 23514, a member of the Pleiades cluster; confirmation as a warm debris disk required data from *ISO*, *Spitzer*, and ground-based telescopes (Spangler et al. 2001; Rhee et al. 2008).

Over the past decade, data from *AKARI*, *Spitzer*, and *WISE* have enabled many surveys for 12–25  $\mu\text{m}$  emission from debris orbiting solar-type main sequence stars (e.g., Stauffer et al. 2005; Silverstone et al. 2006; Beichman et al. 2006; Siegler et al. 2007; Gorlova et al. 2007; Currie et al. 2007; Meyer et al. 2008; Trilling et al. 2008; Carpenter et al. 2009a,b; Moór et al. 2009; Stauffer et al. 2010; Beichman et al. 2011; Chen et al. 2011; Smith et al. 2011; Zuckerman et al. 2011; Luhman & Mamajek 2012; Ribas et al. 2012; Urban et al. 2012; Kennedy & Wyatt 2012; Zuckerman et al. 2012; Fujiwara et al. 2013; Kennedy & Wyatt 2013; Cloutier et al. 2014). Current compilations include stars with ages ranging from  $\sim 10$  Myr to  $\gtrsim 1$  Gyr and relative fluxes of  $F_d/F_\star \approx 0.5$ –100 at 8–24  $\mu\text{m}$ . In some systems, high quality spectra and imaging data confirm the presence of silicate dust orbiting within 1–3 AU of the central star (e.g., Smith et al. 2008; Currie et al. 2011; Olofsson et al. 2012; Smith et al. 2012; Schneider et al. 2013; Ballering et al. 2014). For several others, short time scale variations in  $F_d/F_\star$  suggest rapid changes in the typical sizes and total mass of small particles (e.g., Melis et al. 2012; Meng et al. 2012, 2014, 2015). Interferometric observations further reveal 300 K or hotter dust in some systems (e.g., Absil et al. 2013; Ertel et al. 2014; Mennesson et al. 2014; Defrère et al. 2015).

Taken together, the complete set of data suggest a fairly low warm dust frequency for solar-type stars (see also Stauffer et al. 2005; Gorlova et al. 2007; Carpenter et al. 2009a,b; Chen et al. 2011; Luhman & Mamajek 2012; Ribas et al. 2012; Fujiwara et al. 2013; Kennedy & Wyatt 2013; Patel et al. 2014; Cloutier et al. 2014). Among older stars with ages  $\gtrsim 100$  Myr, only  $\sim 0.01\%$  have debris disks with  $F_d/F_\star \gtrsim 0.2\text{--}0.5$  at  $10\text{--}12\ \mu\text{m}$ . For younger stars, the frequency is  $\sim 1\%$  for 100 Myr-old stars and  $\sim 2\%$  to  $3\%$  for  $10\text{--}20$  Myr stars.

These statistics are generally consistent with the standard theoretical picture where a collisional cascade and occasional giant impacts generate a large population of small particles in the terrestrial zone (see also Raymond et al. 2011; Fujiwara et al. 2013; Kennedy & Wyatt 2013; Genda et al. 2015). As in Fig. 23, emission from the cascade gradually declines with time from  $1\text{--}10$  Myr to  $\sim 100\text{--}150$  Myr. Throughout this period and beyond, giant impacts are responsible for large spikes in dust emission (see also Fig. 6 of Genda et al. 2015). Typical predictions for the level of dust emission are close to those observed.

To make a basic quantitative comparison of our calculations with observations, we scale the dust emission from the  $0.9\text{--}1.1$  AU annulus to an annulus at  $0.4\text{--}2$  AU and derive the fraction of time spent above the *Spitzer* and *WISE* detection limits ( $F_d/F_\star \approx 0.2\text{--}0.5$  at  $8\text{--}12\ \mu\text{m}$ ). Based on current planet detection statistics, we assume  $50\%$  of solar-type stars have at least one Earth-mass planet at  $0.4\text{--}2$  AU (e.g., Youdin 2011; Petigura et al. 2013; Foreman-Mackey et al. 2014; Burke et al. 2015). For these systems, the initial surface density distribution adopted in our calculations is a reasonable choice (e.g., Chambers 2001; Kominami & Ida 2004; Nagasawa et al. 2005; Kenyon & Bromley 2006; Kokubo et al. 2006; O’Brien et al. 2006; Chambers 2008; Fogg & Nelson 2009; Lunine et al. 2011; Raymond et al. 2011, 2012; Hansen & Murray 2012, 2013).

Among this set of calculations, the expected detection frequency  $f_d$  depends on stellar age and  $r_0$ , the maximum size of solid objects at the start of the calculation. For any  $r_0$ ,  $f_d \lesssim 1\%\text{--}10\%$  for stellar ages of  $30\text{--}100$  Myr;  $f_d \lesssim 1\%\text{--}2\%$  for stars older than  $100$  Myr. These predictions are consistent with observations derived from *Spitzer* and *WISE*.

Observations of dust emission for younger stars appear to rule out the possibility that a large fraction of planetary systems produce Earth-mass planets starting from  $1000$  km or larger objects. When  $r_0 \gtrsim 1000$  km, our calculations predict  $f_d \lesssim 1\%\text{--}2\%$  for all stellar ages. Thus, these systems simply produce too little dust at ages when observations suggest at least some systems produce dust. Data for the size distribution of asteroids in the solar system also favor swarms with smaller initial planetesimal sizes (e.g., Morbidelli et al. 2009; Weidenschilling 2011; Johansen et al. 2015).

Compared to observations of stars with ages of  $1\text{--}30$  Myr, calculations with  $r_0 \lesssim 500$  km

tend to produce too much dust. Among the youngest stars (1–5 Myr), the predicted  $f_d$  is a strong function of  $r_0$ , ranging from  $f_d \approx 15\text{--}50\%$  when  $r_0 \lesssim 100$  km to  $f_d \lesssim 5\%$  for  $r_0 \approx 500$  km. For older stars with ages of 5–10 Myr (10–30 Myr),  $f_d \approx 30\%\text{--}40\%$  (5%–10%) independent of  $r_0$ . Given current constraints on warm dust for stars with ages of 1–30 Myr, our predictions agree with observations for 20–30 Myr old stars but are too large by factors of 2–5 for younger stars. The differences between theory and observations for these young stars are fairly independent of  $r_0$ .

Among younger stars, the difference between theory and observations is probably less extreme than indicated by these statistics. In our simulations, the typical level of dust emission at 1–10 Myr is only a factor of  $\sim 2\text{--}3$  larger than current detection limits. Modest reductions in the population of small particles are possible if (i) the smallest particles emit less efficiently than blackbodies (e.g., Backman & Paresce 1993), (ii) the total mass in solids is somewhat smaller at 0.4–2 AU, (iii) the radiation field or the stellar wind of young solar-type stars removes particles with  $r \gtrsim 1 \mu\text{m}$  (Plavchan et al. 2005; Wurz 2012), (iv) small particles are much weaker than assumed, (v) collisional damping is more effective among small particles, or (vi) protoplanets accrete small particles more efficiently. Although investigating these possibilities is beyond the scope of this paper, we plan to analyze their likelihood in future studies. Better limits on the frequency of debris disks with relative fluxes 3–5 times smaller than current detection limits would help to guide this analysis.

## 6. SUMMARY

We analyze a suite of coagulation calculations to examine the long-term evolution of collisional cascades in a ring of solid material with surface density  $\Sigma_0 \approx 10 \text{ g cm}^{-2}$  at 1 AU from a solar-mass star. In pure cascade models where the orbital  $e$  and  $i$  of the solids remain constant with time, destructive collisions slowly reduce the size of the largest objects by factors of 3–20. Over 1–2 Gyr, the total mass, the mass in small particles ( $r \lesssim 1$  mm), and the luminosity decline as  $t^{-n}$ , with  $n = 1.1\text{--}1.2$ . The ratio  $\xi$  of the mass in small particles to the total mass grows by a factor of 2–3 from 1 Myr to 2 Gyr. After 1 Myr, the shape of the size distribution for  $r \gtrsim 1 \mu\text{m}$  is fairly constant in time and approximately follows a power law,  $N(r) \propto r^{-q}$ . The slope  $q$  depends on the form of the relation for the binding energy  $Q_D^*$ : for constant  $Q_D^*$ ,  $q = 3.5$ ; for  $Q_D^*(r)$ ,  $q_s = 3.68$  at small sizes and  $q_l \approx 2.7\text{--}2.9$  at large sizes. Waves superimposed on the power law have modest amplitude and are most pronounced at the smallest and largest sizes in the cascade.

Comparison of these results with the predictions of analytic models highlights several robust outcomes. For the size distribution, analytic estimates for  $q_s$ , the overall level of

waviness, and the approximately invariant shape from  $1\ \mu\text{m}$  to 6–30 km agree with results from the coagulation calculations. Analytic models underestimate the mass lost from destructive collisions. Coagulation calculations have smaller total mass, dust mass, and dust luminosity than analytic models. These differences between analytic models and numerical calculations probably stem from the variation of the size of the largest object with time. In the coagulation calculations, large reductions in  $r_{max}$  shorten the collision time and speed up the evolution.

To place the collisional cascade calculations in context with planet formation models, we examine a suite of coagulation calculations where gravitational interactions among the solids yield an internally consistent  $e$  and  $i$  as a function of particle size. For swarms with  $\Sigma_0 = 10\ \text{g cm}^{-2}$ ,  $r_0 = 10^n$ , and  $n = 0, 1, 2, \dots, 8$ , it takes 0.1–1 Myr for the largest objects to reach sizes of 2000–4000 km. As these protoplanets grow, their gravity stirs up the  $e$  and  $i$  for smaller particles, initiating a collisional cascade. From 0.1–10 Myr, the sizes of the largest objects that suffer catastrophic collisions grows from  $r_{brk} \approx 10\text{--}20\ \text{km}$  to  $r_{brk} \approx 1000\ \text{km}$ . When  $r_0 \lesssim 100\ \text{km}$ , the dust luminosity reaches a peak  $L_d/L_\star \approx 2 - 3 \times 10^{-4}$  and then slowly declines. During this decline, giant impacts between 300–1000 km and larger objects release large amounts of debris, producing pronounced spikes in  $L_d$ . Eventually, accretion by large objects and destructive collisions among smaller objects eliminate all of the smaller particles. The dust luminosity then drops to zero.

Compared to analytic and numerical models of pure collisional cascades, the planet formation calculations reveal several stark differences. In planet formation calculations, the persistent growth in  $r_{brk}$  involves larger and larger objects in the cascade;  $r_{brk}$  is constant in pure cascades. Until the precipitous drop in  $L_d$  when protoplanets achieve their final masses, the decline of  $L_d$  in planet formation models is slower in time. Throughout the evolution, these models also produce a higher frequency of spikes in  $L_d$ . Despite the similar maximum  $L_d$ , planet formation models typically have a factor of 3–10 less mass in small particles ( $r \lesssim 1\ \text{mm}$ ) than pure cascade models.

Observations of known debris disks around solar-type stars provide interesting tests of these calculations. Measurements of the frequency and relative fluxes as a function of stellar age suggest dust produced in collisional cascades and giant impacts contribute to the debris. The lack of dust from planet formation calculations with  $r_0 \gtrsim 1000\ \text{km}$  suggests terrestrial planets grow out of disks with 300–500 km or smaller planetesimals. For older stars with ages exceeding 20–30 Myr, the predicted detection frequency agrees with observations. However, the observed detection frequency for 5–20 Myr old stars is much smaller than expected. Investigations into the accretion, collisional damping, and the strength of small particles might lead to calculations which produce somewhat less dust emission. Better constraints

on the frequency of (i) Earth-mass planets at 1–2 AU and (ii) debris disks with  $L_d/L_\star \ll 10^{-4}$  would allow more stringent tests of the calculations.

We acknowledge a generous allotment of computer time on the NASA ‘discover’ cluster. Comments from M. Geller, G. Kennedy, J. Najita, and an anonymous referee improved our presentation. Portions of this project were supported by the NASA *Astrophysics Theory* and *Origins of Solar Systems* programs through grant NNX10AF35G and the NASA *Outer Planets Program* through grant NNX11AM37G.

## A. Appendix

To test the algorithms used in *Orchestra*, we compare numerical results with analytic solutions to the coagulation equation (Kenyon & Luu 1998; Kenyon & Bromley 2015) and published results from other investigators (Kenyon & Bromley 2001; Bromley & Kenyon 2006; Kenyon & Bromley 2008; Bromley & Kenyon 2011a; Kenyon & Bromley 2015). Here, we examine how *Orchestra* performs for collisional cascades.

### A.1. The Mass Spacing Parameter

The accuracy of coagulation calculations depends on the mass spacing parameter between adjacent mass bins,  $\delta_k = m_{k+1}/m_k$  (e.g., Wetherill 1990; Kenyon & Luu 1998; Kenyon & Bromley 2015). At the start of each calculation, we set the typical mass  $m_k$  and the boundaries  $m_{k-1/2}$  and  $m_{k+1/2}$  of each mass bin. These parameters remain fixed throughout a calculation. The initial average mass within each bin is  $\bar{m}_k = M_k/N_k$ ; typically  $\bar{m}_k = m_k$ . As the calculation proceeds, collisions add and remove material from all bins; the average mass in a bin  $\bar{m}_k$  and the average physical radius of particles in the bin  $\bar{r}_k = (3\bar{m}_k/4\pi\rho_p)^{1/3}$  then change with time.

To illustrate how the evolution depends on  $\delta$ , we consider an annulus centered at  $a = 1$  AU. The annulus has a width  $\Delta a = 0.2a$ ; thus the inner and outer radii are  $a_{in} = 0.9$  AU and  $a_{out} = 1.1$  AU. We seed the annulus with particles having mass density  $\rho_p = 3$  g cm $^{-3}$ ,  $e = 0.1$ , and  $i = e/2$ . The annulus has surface density  $\Sigma_0 = 10.6$  g cm $^{-2}$  and total mass  $M_0 = 0.5 M_\oplus$ .

Fig. 24 shows the time-variation of  $r_{max}$  (the radius of the largest object) for calculations with a mono-disperse set of 100 km objects and five different values of  $\delta$ . All curves have the same general shape: after a brief,  $\sim 10^5$  yr period where  $r_{max}$  is roughly constant, the size

of the largest objects declines monotonically with time. Tracks with larger  $\delta$  decline faster.

Along each track, the evolution consists of a gradual reduction in  $r_{max}$  interspersed with large jumps to smaller  $r_{max}$ . Cratering collisions – where somewhat smaller objects gradually chip away at the mass of larger objects – produce continuous mass loss from the largest objects. Thus, the average mass in the largest mass bin falls with time. Eventually, this mass falls below the mass boundary between adjacent bins (e.g.,  $\bar{m}_k < m_{k-1/2}$ ). Objects in bin  $k$  are then placed into bin  $k - 1$ . Averaging the mass of the ‘old’ objects in bin  $k - 1$  with the ‘new’ objects from bin  $k$  yields a new average mass  $\bar{m}_{k-1}$  which is smaller than the average mass of bin  $k$ . Thus, the radius (average mass) of the largest object jumps downward. Because the spacing of mass bins scales with  $\delta$ , calculations with larger  $\delta$  have larger jumps than those with smaller  $\delta$ .

Although the mass loss rate from the grid is fairly insensitive to  $\delta$  (see below), the mass of the largest object declines faster in calculations with larger  $\delta$ . Cratering collisions are responsible for this difference. For all  $\delta$ , these collisions are rare. Thus, only a few of the largest objects suffer substantial mass loss from cratering collisions every time step. When  $\delta$  is small (1.05–1.10), these objects are placed into the next smallest mass bin; the average mass of the remaining objects in the mass bin is unchanged. When  $\delta$  is large (1.41–2.00), the amount of mass loss is not sufficient to place objects into the next smallest mass bin; the average mass of all objects in the bin then decreases. As a result, the average mass of the largest objects declines faster when  $\delta = 2$  than when  $\delta = 1.05$ .

Despite this difference, other aspects of the evolution are fairly insensitive to  $\delta$ . Fig. 25 shows the relative size distributions at 1 Myr. Each curve follows a standard pattern, with an excess (deficit) of particles at 1–10  $\mu\text{m}$  (10–100  $\mu\text{m}$ ), a wavy pattern at 0.1 mm to 0.1 km, and then a rise at larger sizes. For  $\delta = 1.05$ –1.41, there is little difference between the curves. When  $\delta = 2$ , the amplitude of the waves is larger.

Fig. 26 shows a similar pattern at 100 Myr. The three curves for  $\delta = 1.05$ –1.19 are almost identical. Although the pattern for  $\delta = 1.41$  is very similar, the waviness is more pronounced for particles with sizes of 100  $\mu\text{m}$ . This waviness is even larger for  $\delta = 2$ .

To explore the evolution of the particle flux through the grid, Fig. 27 shows the production rate for particles with  $r < 1 \mu\text{m}$ . At early times, collisions among the mono-disperse set of 100 km objects produce little debris with sizes smaller than 1 mm. The mass loss rate from the grid is then zero. As each calculation proceeds, destructive collisions disperse more and more small particles. Collisions among these particles yield particles smaller than 1  $\mu\text{m}$ . The mass loss rate then rises abruptly. The timing of this rise depends on stochastic variations in the collision rates among large particles. Thus, the timing of the rise is not sensitive to



$\delta$ . The size distribution then takes awhile to reach an equilibrium which depends on  $\delta$  and on the timing of the rise in the mass loss rate. As this equilibrium is established, the mass loss rate rises slowly. Afterwards, the mass loss rate declines,  $\dot{M} \propto t^{-\alpha}$  with  $\alpha \approx 2.0$ – $2.25$ . For calculations with  $\delta = 1.05$ – $1.41$ , the long term time evolution of  $\dot{M}$  is independent of  $\delta$ . When  $\delta = 2.0$ , the decline of  $\dot{M}$  with time is more rapid at late times.

The evolution of the dust luminosity follows the evolution of  $\dot{M}$  (Fig. 28). Early on, it takes awhile for destructive collisions to produce a large ensemble of small objects. Once these objects exist, the dust luminosity rises very rapidly. As the size distribution of small particles adjusts to an equilibrium, the luminosity slowly rises to a clear maximum. Once the size distribution reaches an equilibrium, the luminosity declines roughly linearly with time. Calculations with  $\delta = 1.05$ – $1.41$  yield nearly identical solutions for the time variation of the dust luminosity. At late times, the luminosity declines more rapidly when  $\delta = 2.00$  than when  $\delta = 1.05$ – $1.41$ .

To conclude this discussion, we consider how the time evolution of  $\dot{M}$  changes in a ‘hybrid’ model, where we adopt different values of  $\delta$  for large and small particles. We adopt  $\delta = 2.0$  for particles with  $r \lesssim 0.2$ – $0.4$  km and  $\delta = 1.05, 1.10, 1.19$ , or  $1.41$  for particles with  $r \gtrsim 3$ – $5$  km. In between these limits,  $\delta$  varies linearly with particle size. This approach seeks to capture the better accuracy of small  $\delta$  models with a smaller expense of cpu time.

Fig. 29 shows the results. Aside from the magenta curve (the pure  $\delta = 2.00$  from Fig. 27), all of the hybrid models follow the time variation of  $\dot{M}$  established for models with  $\delta = 1.05$  for all particles sizes. These results demonstrate that we can follow collisional cascades with  $\delta = 2.0$  for small particles and  $\delta \lesssim 1.41$  for large particles.

## A.2. Analytic Model for Wavy Size Distributions

Wavy size distributions are characteristic of coagulation calculations with a low mass cutoff (Campo Bagatin et al. 1994; Durda et al. 1998; O’Brien & Greenberg 2003; Kral et al. 2013). To extend previous analytic and numerical studies, Wyatt et al. (2011) explore a new steady state numerical model which shows how the amplitudes and positions of the waves depend on the collision velocity. Here, we derive an analytic solution to their model and briefly illustrate how the properties of the waves depend on  $Q_D^*$ .

Following method I of the Wyatt et al. (2011) framework (see their §2.4.1), we establish a logarithmic grid of particle sizes extending from  $r_{min}$  to  $r_{max}$  with indices  $k = 1$  to  $k = N$ . Reversing the sense of the labeling from Wyatt et al. (2011), the smallest (largest) bin has  $k = 1$  ( $k = N$ ). If the mass loss rate through the grid is independent of particle size, the mass

$M_k$  contained in a mass bin is then a simple function of the rate of destructive collisions  $R_k$  summed over all particles with index  $i$  and  $i < k$ :

$$M_k = C_0 R_k^{-1} , \quad (\text{A1})$$

where  $C_0$  is an arbitrary constant (see also eq. 15 of Wyatt et al. 2011). The sum  $R_k$  is

$$R_k = C_1 \sum_{i=1}^{i=k} \epsilon_{ik} M_i (r_i + r_k)^2 / r_i^3 , \quad (\text{A2})$$

where  $C_1$  is another constant. Recalling that  $Q_c$  is the collision energy per unit mass and  $Q_D^*$  is the binding energy per unit mass,

$$\epsilon_{ik} = \begin{cases} 0 & Q_c < Q_D^* \\ 1 & Q_c \geq Q_D^* \end{cases} \quad (\text{A3})$$

Thus,  $R_k$  is the rate of collisions which disperse at least half the mass of the colliding pair of particles.

The mass conservation equation in eq. A1 has a recursive solution. For  $k = 1$ ,  $R_k$  has only one term:  $R_k = 4C_1 M_k / r_k$ . Thus,  $M_k^2 = C_0 / 4C_1 r_k$ . For  $k \geq 2$ ,  $R_k$  is a sum over terms with known  $M_i$  and one term with  $M_k$ :

$$R_k = 4C_1 M_k / r_k + C_1 \sum_{i=1}^{i=k-1} \epsilon_{ik} M_i (r_i + r_k)^2 / r_i^3 . \quad (\text{A4})$$

Setting  $R_{ki}$  equal to the second term in eq. A4 leads to a quadratic equation,

$$4C_1 M_k^2 + R_{ki} M_k - C_0 = 0 , \quad (\text{A5})$$

which has only one possible solution with  $M_k > 0$ .

To examine how steady-state mass distributions depend on  $Q_D^*$ , we consider models with  $Q_D^* = \text{constant}$  and  $Q_D^* = Q_b r^{\beta_b} + Q_g \rho_p r^{\beta_g}$  with the standard fragmentation parameters (§4.1). In these examples, the collision velocity  $v = 3 \text{ km s}^{-1}$ , the mass density  $\rho = 3 \text{ g cm}^{-3}$ , and  $\delta_r = r_{i+1}/r_i = 10^{0.01} = 1.023$ . The center-of-mass collision energy  $Q_c = v_c^2 m_i m_k / 2(m_i + m_k)^2$  then establishes the ratio  $Q_c/Q_D^*$  and  $\epsilon_{ik}$  for each pair of particles. Recursive solution of eq. A5 for  $k = 1$  ( $1 \mu\text{m}$ ) to  $k = 1101$  ( $100 \text{ km}$ ) yields  $M_k$  for each particle size. Dividing  $M_k$  by the expected  $M_k \propto r_k^\alpha$  with  $\alpha = 1/2$  for  $Q_D^* = \text{constant}$  and  $\alpha = 0.32$  for  $Q_D^*(r)$  yields the relative mass in each bin.

Fig. 30 compares results for the two models. When  $Q_D^* = \text{constant}$  (violet line), the relative mass generally follows the power law. Waves with modest amplitude start at the

small-size cutoff and gradually diminish in amplitude to large sizes. Relative to the power law, there is a clear excess of particles at the smallest sizes: these bins require extra mass to generate enough collisions to maintain a constant rate of mass loss per bin.

When  $Q_D^*$  is a function of particle size, the system follows a power law from 1  $\mu\text{m}$  to 0.1 km. For larger sizes, the gravity component of the binding energy dominates; the slope of the size distribution changes from 3.68 to 3.0. Although systems where  $Q_D^*$  is a function of  $r$  still display wavy size distributions, the waves have smaller amplitude and shorter wavelength.

For both  $Q_D^*$  relations, the shape of the size distribution derived from numerical simulations is remarkably close to the analytic prediction. In particular, (i) the amplitudes of the waves at 1–10  $\mu\text{m}$  and (ii) the shape of the rise at 0.1–10 km in systems with  $Q_D^*(r)$  are very similar in the analytic and numerical calculations. In the numerical simulations, cratering produces a longer wavelength compared to the analytic model. The gradual reduction in the size of the largest object modifies the shape of the size distribution at the largest sizes.

## REFERENCES

- Absil, O., Defrère, D., Coudé du Foresto, V., et al. 2013, *A&A*, 555, A104
- Agnor, C., & Asphaug, E. 2004, *ApJ*, 613, L157
- Agnor, C. B., Canup, R. M., & Levison, H. F. 1999, *Icarus*, 142, 219
- Arakawa, M., Leliwa-Kopystynski, J., & Maeno, N. 2002, *Icarus*, 158, 516
- Asphaug, E., Agnor, C. B., & Williams, Q. 2006, *Nature*, 439, 155
- Asphaug, E., & Benz, W. 1996, *Icarus*, 121, 225
- Backman, D. E., & Paresce, F. 1993, in *Protostars and Planets III*, ed. E. H. Levy & J. I. Lunine, 1253–1304
- Ballering, N. P., Rieke, G. H., & Gáspár, A. 2014, *ApJ*, 793, 57
- Bandermann, L. W. 1972, *MNRAS*, 160, 321
- Barge, P., & Pellat, R. 1991, *Icarus*, 93, 270
- Beichman, C. A., Tanner, A., Bryden, G., et al. 2006, *ApJ*, 639, 1166
- Beichman, C. A., Lisse, C. M., Tanner, A. M., et al. 2011, *ApJ*, 743, 85

- Benz, W., & Asphaug, E. 1999, *Icarus*, 142, 5
- Booth, M., Wyatt, M. C., Morbidelli, A., Moro-Martín, A., & Levison, H. F. 2009, *MNRAS*, 399, 385
- Bromley, B. C., & Kenyon, S. J. 2006, *AJ*, 131, 2737
- . 2011a, *ApJ*, 731, 101
- . 2011b, *ApJ*, 735, 29
- . 2013, *ApJ*, 764, 192
- Burchell, M. J., Leliwa-Kopystyński, J., & Arakawa, M. 2005, *Icarus*, 179, 274
- Burke, C. J., Christiansen, J. L., Mullally, F., et al. 2015, *ApJ*, 809, 8
- Burns, J. A., Lamy, P. L., & Soter, S. 1979, *Icarus*, 40, 1
- Campo Bagatin, A., Cellino, A., Davis, D. R., Farinella, P., & Paolicchi, P. 1994, *Planet. Space Sci.*, 42, 1079
- Carpenter, J. M., Mamajek, E. E., Hillenbrand, L. A., & Meyer, M. R. 2009a, *ApJ*, 705, 1646
- Carpenter, J. M., Bouwman, J., Mamajek, E. E., et al. 2009b, *ApJS*, 181, 197
- Chambers, J. 2008, *Icarus*, 198, 256
- Chambers, J. E. 2001, *Icarus*, 152, 205
- Chen, C. H., Mamajek, E. E., Bitner, M. A., et al. 2011, *ApJ*, 738, 122
- Chiang, E., & Youdin, A. N. 2010, *Annual Review of Earth and Planetary Sciences*, 38, 493
- Cloutier, R., Currie, T., Rieke, G. H., et al. 2014, *ApJ*, 796, 127
- Currie, T., Kenyon, S. J., Balog, Z., et al. 2008, *ApJ*, 672, 558
- Currie, T., Kenyon, S. J., Rieke, G., Balog, Z., & Bromley, B. C. 2007, *ApJ*, 663, L105
- Currie, T., Lisse, C. M., Sicilia-Aguilar, A., Rieke, G. H., & Su, K. Y. L. 2011, *ApJ*, 734, 115
- Davis, D. R., Chapman, C. R., Weidenschilling, S. J., & Greenberg, R. 1985, *Icarus*, 63, 30

- Defrère, D., Hinz, P. M., Skemer, A. J., et al. 2015, *ApJ*, 799, 42
- Dohnanyi, J. S. 1969, *J. Geophys. Res.*, 74, 2531
- Dominik, C., & Decin, G. 2003, *ApJ*, 598, 626
- Durda, D. D., Greenberg, R., & Jedicke, R. 1998, *Icarus*, 135, 431
- Ertel, S., Absil, O., Defrère, D., et al. 2014, *A&A*, 570, A128
- Fogg, M. J., & Nelson, R. P. 2009, *A&A*, 498, 575
- Foreman-Mackey, D., Hogg, D. W., & Morton, T. D. 2014, *ApJ*, 795, 64
- Fujiwara, H., Ishihara, D., Onaka, T., et al. 2013, *A&A*, 550, A45
- Gáspár, A., Psaltis, D., Özel, F., Rieke, G. H., & Cooney, A. 2012a, *ApJ*, 749, 14
- Gáspár, A., Psaltis, D., Rieke, G. H., & Özel, F. 2012b, *ApJ*, 754, 74
- Gáspár, A., Rieke, G. H., & Balog, Z. 2013, *ApJ*, 768, 25
- Genda, H., Kobayashi, H., & Kokubo, E. 2015, *ArXiv e-prints*, arXiv:1508.00977
- Genda, H., Kokubo, E., & Ida, S. 2012, *ApJ*, 744, 137
- Giblin, I., Davis, D. R., & Ryan, E. V. 2004, *Icarus*, 171, 487
- Glaschke, P., Amaro-Seoane, P., & Spurzem, R. 2014, *MNRAS*, 445, 3620
- Goldreich, P., Lithwick, Y., & Sari, R. 2004, *ARA&A*, 42, 549
- Gorlova, N., Balog, Z., Rieke, G. H., et al. 2007, *ApJ*, 670, 516
- Greenberg, R., Hartmann, W. K., Chapman, C. R., & Wacker, J. F. 1978, *Icarus*, 35, 1
- Greenberg, R., Weidenschilling, S. J., Chapman, C. R., & Davis, D. R. 1984, *Icarus*, 59, 87
- Greenzweig, Y., & Lissauer, J. J. 1990, *Icarus*, 87, 40
- Grigorieva, A., Artymowicz, P., & Thébault, P. 2007, *A&A*, 461, 537
- Grogan, K., Dermott, S. F., & Durda, D. D. 2001, *Icarus*, 152, 251
- Hansen, B. M. S., & Murray, N. 2012, *ApJ*, 751, 158
- . 2013, *ApJ*, 775, 53

- Hayashi, C. 1981, Progress of Theoretical Physics Supplement, 70, 35
- Hellyer, B. 1970, MNRAS, 148, 383
- Holsapple, K. A. 1994, Planet. Space Sci., 42, 1067
- Holsapple, K. A., & Housen, K. R. 2007, Icarus, 191, 586
- Housen, K. R., & Holsapple, K. A. 1999, Icarus, 142, 21
- Jackson, A. P., & Wyatt, M. C. 2012, MNRAS, 425, 657
- Johansen, A., Mac Low, M.-M., Lacerda, P., & Bizzarro, M. 2015, Science Advances, 1, 15109
- Kennedy, G. M., & Wyatt, M. C. 2010, MNRAS, 405, 1253
- . 2011, MNRAS, 412, 2137
- . 2012, MNRAS, 426, 91
- . 2013, MNRAS, 433, 2334
- Kennedy, G. M., Wyatt, M. C., Sibthorpe, B., et al. 2012, MNRAS, 426, 2115
- Kennedy, G. M., Wyatt, M. C., Su, K. Y. L., & Stansberry, J. A. 2011, MNRAS, 417, 2281
- Kenyon, S. J., & Bromley, B. C. 2001, AJ, 121, 538
- . 2002a, AJ, 123, 1757
- . 2002b, ApJ, 577, L35
- . 2004a, AJ, 127, 513
- . 2004b, ApJ, 602, L133
- . 2005, AJ, 130, 269
- . 2006, AJ, 131, 1837
- . 2008, ApJS, 179, 451
- . 2010, ApJS, 188, 242
- . 2012, AJ, 143, 63

- . 2014, *AJ*, 147, 8
- . 2015, *ApJ*, 806, 42
- Kenyon, S. J., Currie, T., & Bromley, B. C. 2014, *ApJ*, 786, 70
- Kenyon, S. J., & Luu, J. X. 1998, *AJ*, 115, 2136
- . 1999, *AJ*, 118, 1101
- Kobayashi, H., & Dauphas, N. 2013, *Icarus*, 225, 122
- Kobayashi, H., & Löhne, T. 2014, *MNRAS*, 442, 3266
- Kobayashi, H., & Tanaka, H. 2010, *Icarus*, 206, 735
- Kobayashi, H., Tanaka, H., Krivov, A. V., & Inaba, S. 2010, *Icarus*, 209, 836
- Kokubo, E., & Ida, S. 1996, *Icarus*, 123, 180
- Kokubo, E., Kominami, J., & Ida, S. 2006, *ApJ*, 642, 1131
- Kominami, J., & Ida, S. 2002, *Icarus*, 157, 43
- . 2004, *Icarus*, 167, 231
- Kral, Q., Thébault, P., & Charnoz, S. 2013, *A&A*, 558, A121
- Krivov, A. V., Löhne, T., & Sremčević, M. 2006, *A&A*, 455, 509
- Krivov, A. V., Eiroa, C., Löhne, T., et al. 2013, *ApJ*, 772, 32
- Lee, M. H. 2000, *Icarus*, 143, 74
- Leinhardt, Z. M., & Stewart, S. T. 2009, *Icarus*, 199, 542
- . 2012, *ApJ*, 745, 79
- Leinhardt, Z. M., Stewart, S. T., & Schultz, P. H. 2008, in *The Solar System Beyond Neptune*, ed. Barucci, M. A., Boehnhardt, H., Cruikshank, D. P., & Morbidelli, A. (University of Arizona Press, Tucson, AZ), 195–211
- Levison, H. F., Duncan, M. J., & Thommes, E. 2012, *AJ*, 144, 119
- Levison, H. F., & Morbidelli, A. 2007, *ArXiv Astrophysics e-prints*, astro-ph/0701544
- Löhne, T., Krivov, A. V., & Rodmann, J. 2008, *ApJ*, 673, 1123

- Löhne, T., Augereau, J.-C., Ertel, S., et al. 2012, *A&A*, 537, A110
- Love, S. G., & Ahrens, T. J. 1996, *Icarus*, 124, 141
- Luhman, K. L., & Mamajek, E. E. 2012, *ApJ*, 758, 31
- Lunine, J. I., O’Brien, D. P., Raymond, S. N., et al. 2011, *Advanced Science Letters*, 4, 325
- Mamajek, E. E., Meyer, M. R., Hinz, P. M., et al. 2004, *ApJ*, 612, 496
- Matthews, B. C., Krivov, A. V., Wyatt, M. C., Bryden, G., & Eiroa, C. 2014, ArXiv e-prints, arXiv:1401.0743
- Melis, C., Zuckerman, B., Rhee, J. H., & Song, I. 2010, *ApJ*, 717, L57
- Melis, C., Zuckerman, B., Rhee, J. H., et al. 2012, *Nature*, 487, 74
- Meng, H. Y. A., Rieke, G. H., Su, K. Y. L., et al. 2012, *ApJ*, 751, L17
- Meng, H. Y. A., Su, K. Y. L., Rieke, G. H., et al. 2014, *Science*, 345, 1032
- . 2015, *ApJ*, 805, 77
- Mennesson, B., Millan-Gabet, R., Serabyn, E., et al. 2014, *ApJ*, 797, 119
- Meyer, M. R., Carpenter, J. M., Mamajek, E. E., et al. 2008, *ApJ*, 673, L181
- Moór, A., Apai, D., Pascucci, I., et al. 2009, *ApJ*, 700, L25
- Morbidelli, A., Bottke, W. F., Nesvorný, D., & Levison, H. F. 2009, *Icarus*, 204, 558
- Mustill, A. J., & Wyatt, M. C. 2009, *MNRAS*, 399, 1403
- Nagasawa, M., Lin, D. N. C., & Thommes, E. 2005, *ApJ*, 635, 578
- Nesvold, E. R., Kuchner, M. J., Rein, H., & Pan, M. 2013, *ApJ*, 777, 144
- O’Brien, D. P., & Greenberg, R. 2003, *Icarus*, 164, 334
- O’Brien, D. P., Morbidelli, A., & Levison, H. F. 2006, *Icarus*, 184, 39
- Ohtsuki, K. 1992, *Icarus*, 98, 20
- . 1999, *Icarus*, 137, 152
- Ohtsuki, K., & Nakagawa, Y. 1988, *Progress of Theoretical Physics Supplement*, 96, 239



- Ohtsuki, K., Stewart, G. R., & Ida, S. 2002, *Icarus*, 155, 436
- Olofsson, J., Juhász, A., Henning, T., et al. 2012, *A&A*, 542, A90
- Ormel, C. W., Dullemond, C. P., & Spaans, M. 2010, *Icarus*, 210, 507
- Patel, R. I., Metchev, S. A., & Heinze, A. 2014, *ApJS*, 212, 10
- Petigura, E. A., Howard, A. W., & Marcy, G. W. 2013, *Proceedings of the National Academy of Science*, 110, 19273
- Plavchan, P., Jura, M., & Lipsky, S. J. 2005, *ApJ*, 631, 1161
- Raymond, S. N., Kokubo, E., Morbidelli, A., Morishima, R., & Walsh, K. J. 2014, *Protostars and Planets VI*, 595
- Raymond, S. N., Quinn, T., & Lunine, J. I. 2005, *ApJ*, 632, 670
- Raymond, S. N., Armitage, P. J., Moro-Martín, A., et al. 2011, *A&A*, 530, A62
- . 2012, *A&A*, 541, A11
- Rhee, J. H., Song, I., & Zuckerman, B. 2008, *ApJ*, 675, 777
- Ribas, Á., Merín, B., Ardila, D. R., & Bouy, H. 2012, *A&A*, 541, A38
- Rieke, G. H., Su, K. Y. L., Stansberry, J. A., et al. 2005, *ApJ*, 620, 1010
- Rodríguez, D. R., Duchêne, G., Tom, H., et al. 2015, *MNRAS*, 449, 3160
- Rodríguez, D. R., & Zuckerman, B. 2012, *ApJ*, 745, 147
- Ryan, E. V., Davis, D. R., & Giblin, I. 1999, *Icarus*, 142, 56
- Safronov, V. S. 1969, *Evolutsiia doplanetnogo oblaka*. (Evolution of the Protoplanetary Cloud and Formation of the Earth and Planets, Nauka, Moscow [Translation 1972, NASA TT F-677] (1969.))
- Schneider, A., Song, I., Melis, C., et al. 2013, *ApJ*, 777, 78
- Shannon, A., Wu, Y., & Lithwick, Y. 2015, *ApJ*, 801, 15
- Siegler, N., Muzerolle, J., Young, E. T., et al. 2007, *ApJ*, 654, 580
- Silverstone, M. D., Meyer, M. R., Mamajek, E. E., et al. 2006, *ApJ*, 639, 1138

- Smith, R., Jeffries, R. D., & Oliveira, J. M. 2011, *MNRAS*, 411, 2186
- Smith, R., Wyatt, M. C., & Dent, W. R. F. 2008, *A&A*, 485, 897
- Smith, R., Wyatt, M. C., & Haniff, C. A. 2012, *MNRAS*, 422, 2560
- Song, I., Zuckerman, B., Weinberger, A. J., & Becklin, E. E. 2005, *Nature*, 436, 363
- Spangler, C., Sargent, A. I., Silverstone, M. D., Becklin, E. E., & Zuckerman, B. 2001, *ApJ*, 555, 932
- Spaute, D., Weidenschilling, S. J., Davis, D. R., & Marzari, F. 1991, *Icarus*, 92, 147
- Stark, C. C., & Kuchner, M. J. 2009, *ApJ*, 707, 543
- Stauffer, J. R., Rebull, L. M., Carpenter, J., et al. 2005, *AJ*, 130, 1834
- Stauffer, J. R., Rebull, L. M., James, D., et al. 2010, *ApJ*, 719, 1859
- Stern, S. A., & Colwell, J. E. 1997, *AJ*, 114, 841
- Tanaka, H., Inaba, S., & Nakazawa, K. 1996, *Icarus*, 123, 450
- Thébault, P., & Augereau, J.-C. 2007, *A&A*, 472, 169
- Trilling, D. E., Stansberry, J. A., Stapelfeldt, K. R., et al. 2007, *ApJ*, 658, 1289
- Trilling, D. E., Bryden, G., Beichman, C. A., et al. 2008, *ApJ*, 674, 1086
- Urban, L. E., Rieke, G., Su, K., & Trilling, D. E. 2012, *ApJ*, 750, 98
- Weidenschilling, S. J. 1977, *Ap&SS*, 51, 153
- . 1980, *Icarus*, 44, 172
- . 1989, *Icarus*, 80, 179
- . 1994, *Nature*, 368, 721
- . 2010a, *ApJ*, 722, 1716
- . 2010b, *ApJ*, 722, 1716
- . 2011, *Icarus*, 214, 671
- Weidenschilling, S. J., Spaute, D., Davis, D. R., Marzari, F., & Ohtsuki, K. 1997, *Icarus*, 128, 429

- Weinberger, A. J., Becklin, E. E., Zuckerman, B., & Song, I. 2004, *AJ*, 127, 2246
- Wetherill, G. W. 1980, *ARA&A*, 18, 77
- . 1990, *Icarus*, 88, 336
- Wetherill, G. W., & Stewart, G. R. 1989, *Icarus*, 77, 330
- . 1993, *Icarus*, 106, 190
- Williams, D. R., & Wetherill, G. W. 1994, *Icarus*, 107, 117
- Wurz, P. 2012, in *Astrophysics and Space Science Library*, Vol. 385, *Astrophysics and Space Science Library*, ed. I. Mann, N. Meyer-Vernet, & A. Czechowski, 161
- Wyatt, M. C. 2008, *ARA&A*, 46, 339
- Wyatt, M. C., Booth, M., Payne, M. J., & Churcher, L. J. 2010, *MNRAS*, 402, 657
- Wyatt, M. C., Clarke, C. J., & Booth, M. 2011, *Celestial Mechanics and Dynamical Astronomy*, 111, 1
- Wyatt, M. C., & Dent, W. R. F. 2002, *MNRAS*, 334, 589
- Wyatt, M. C., Smith, R., Greaves, J. S., et al. 2007a, *ApJ*, 658, 569
- Wyatt, M. C., Smith, R., Su, K. Y. L., et al. 2007b, *ApJ*, 663, 365
- Youdin, A. N. 2011, *ApJ*, 742, 38
- Youdin, A. N., & Kenyon, S. J. 2013, *From Disks to Planets*, ed. T. D. Oswalt, L. M. French, & P. Kalas (Dordrecht: Springer Science & Business Media), 1
- Zuckerman, B., Melis, C., Rhee, J. H., Schneider, A., & Song, I. 2012, *ApJ*, 752, 58
- Zuckerman, B., Rhee, J. H., Song, I., & Bessell, M. S. 2011, *ApJ*, 732, 61
- Zuckerman, B., & Song, I. 2004, *ApJ*, 603, 738

Table 1. List of Variables

Variable	Definition
$a$	semimajor axis, radial coordinate
$A_d$	cross-sectional area of particles
$b_d$	exponent in relation for debris from collisions
$b_l$	exponent in relation for mass of largest particle in debris
$e$	eccentricity
$e_H$	Hill eccentricity
$f_c$	fraction of solids converted into small particles ejected by radiation pressure
$f_d$	detection frequency of dust emission
$f_g$	gravitational focusing factor
$F$	radiation flux emitted by a particle or a star at a specific wavelength
$h$	horizontal velocity
$H$	vertical scale height
$i$	inclination
$L_d$	luminosity of particles
$L_\star$	stellar luminosity
$m$	particle mass
$\bar{n}$	average mass of particle in a mass bin
$m_l$	mass of largest particle in debris
$m_{l,0}$	coefficient in relation for mass of largest particle in debris
$m_{max}$	mass of largest particle
$m_{min}$	mass of smallest particle
$M_d$	total mass in particles
$\dot{M}$	mass loss rate
$M_\star$	stellar mass
$n$	exponent of power law or particle number density
$N$	particle number
$N(> r)$	cumulative number of particles larger than $r$
$N_{max}$	number of largest particles
$q$	exponent of power law size distribution
$q_c, q_r$	exponents for cumulative and relative cumulative size distribution
$q_d$	exponent of power law size distribution for debris
$Q_b, Q_g$	coefficients in $Q_D^\star$ relation
$Q_c$	center of mass collision energy

Table 1—Continued

Variable	Definition
$Q_D^*$	collision energy required to eject 50% of the mass
$r$	particle radius
$\bar{r}$	average radius of particle in a mass bin
$r_{brk}$	radius of particles destroyed in equal mass collisions
$r_{max}$	radius of largest particle
$r_{min}$	radius of smallest particle
$r_Q$	particle size with smallest $Q_D^*$
$t$	time
$t_c$	collision time
$T$	temperature
$v$	relative collision velocity
$v_h$	horizontal velocity
$v_K$	orbital velocity
$v_z$	vertical velocity
$V$	volume
$\alpha$	correction factor for collision time
$\beta$	ratio of the radiation force to the gravitational force
$\beta_b, \beta_g$	exponents in $Q_D^*$ relation
$\delta$	mass spacing factor
$\delta a$	width of annulus
$\xi$	ratio of mass in small particles ( $r < 1$ mm) to total mass
$\rho$	particle mass density
$\sigma$	geometric cross section
$\Sigma$	surface density
$\Omega$	angular velocity

Note. — Variables with a subscript ‘0’ refer to initial conditions; e.g.,  $e_0$  is the initial eccentricity

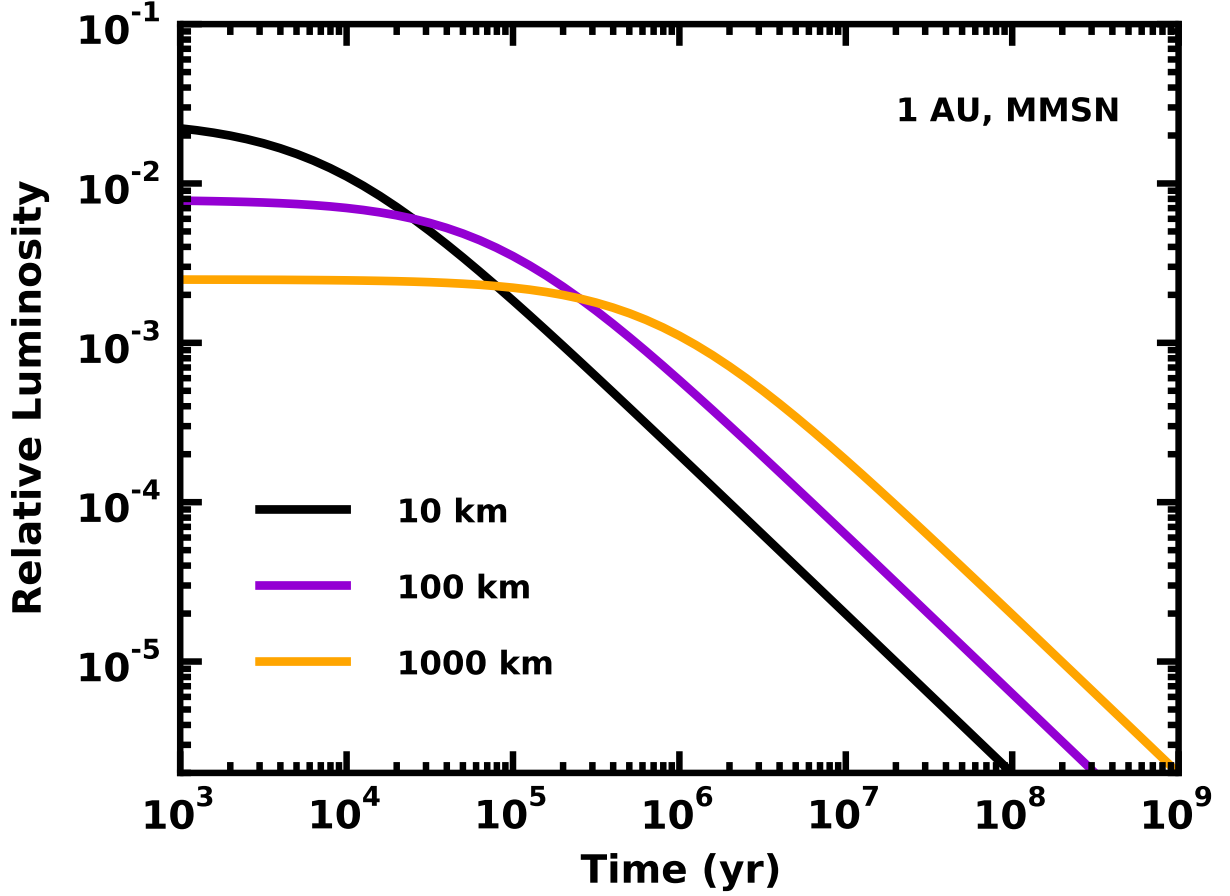


Fig. 1.— Time evolution of the relative luminosity  $L_d/L_*$  derived from the analytic model for a collisional cascade. Material orbits a  $1 M_\odot$  star inside a cylindrical annulus with  $a = 1$  AU,  $\delta a = 0.2$  AU, and  $\Sigma = 10 \text{ g cm}^{-2}$ . Solid curves plot the evolution of  $L_d/L_*$  for cascades with  $r_{max} = 10$  km (black curve), 100 km (violet curve), and 1000 km (orange curve). Cascades with smaller  $r_{max}$  have larger initial luminosity which declines on much shorter time scales.

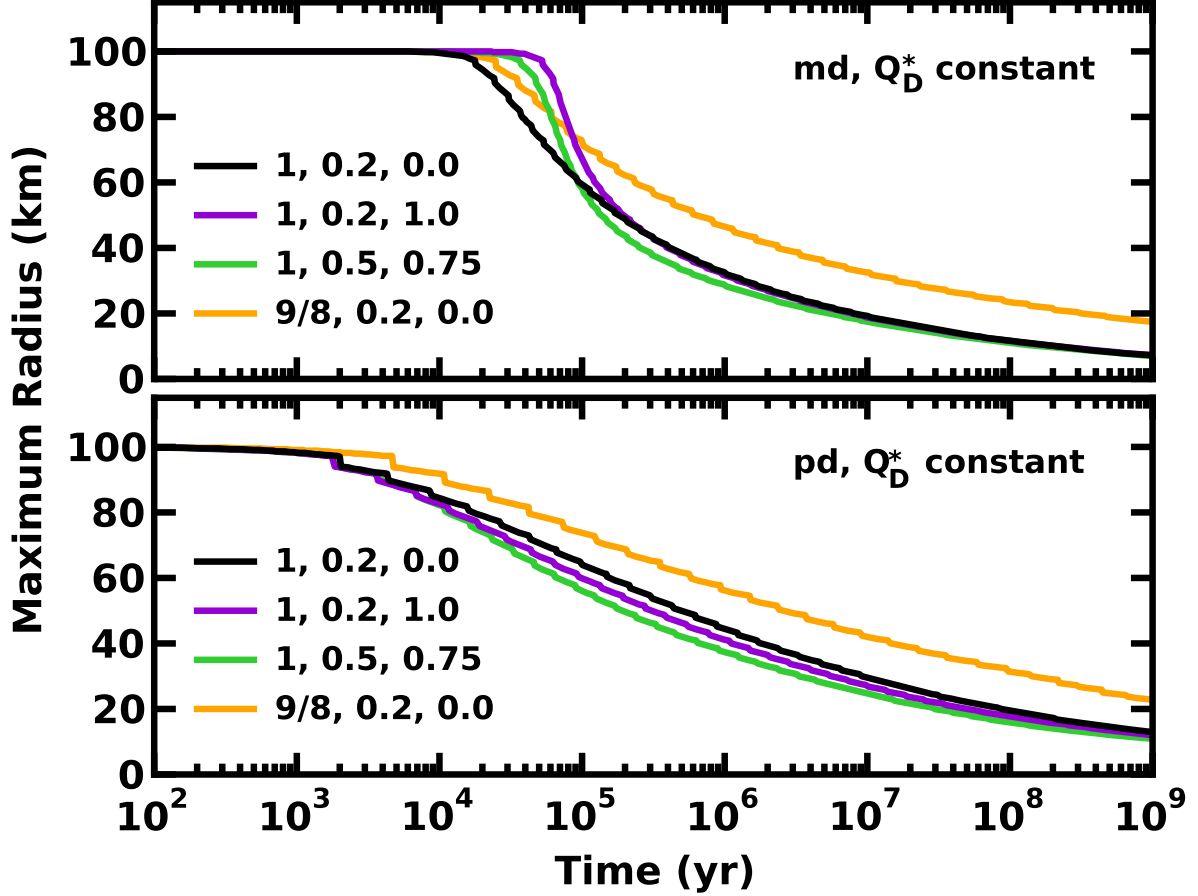


Fig. 2.— Time evolution of  $r_{max}$  in collisional cascades with  $e = 0.1$ ,  $Q_D^* = 6 \times 10^7 \text{ erg g}^{-1}$  and various initial conditions and input parameters. The legend indicates  $b_d$ ,  $m_{l,0}$ , and  $b_l$  for each curve. *Upper panel:* results for calculations with a single initial particle size (‘md’;  $r_0 = 100 \text{ km}$ ); after  $10^4 - 10^5 \text{ yr}$ , the maximum particle size rapidly evolves from 100 km to 10–20 km. *Lower panel:* results for calculations with a power law initial size distribution having  $q_0 = 3.5$  from  $1 \mu\text{m}$  to 100 km (‘pd’); the largest particles gradually diminish in size from 100 km to 20–30 km.

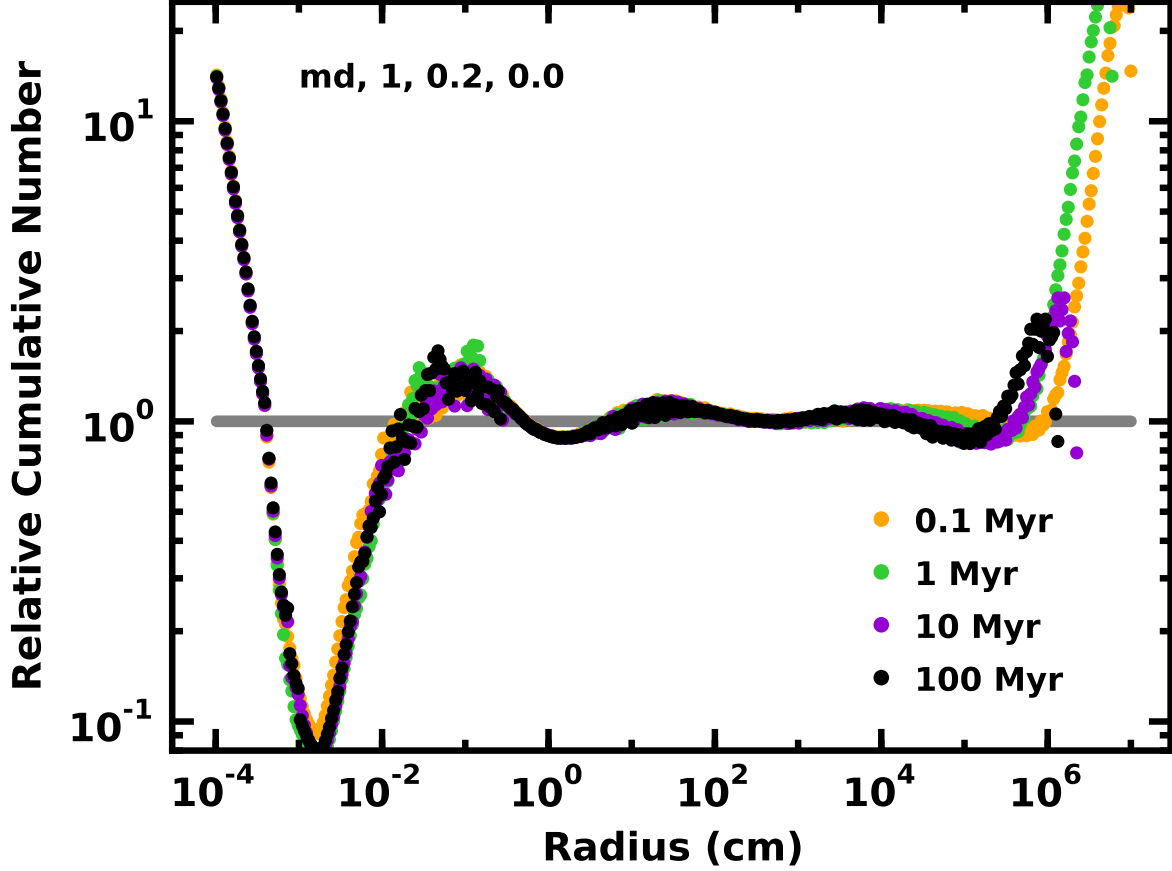


Fig. 3.— Time evolution of the relative cumulative size distribution  $N(> r)/r^{-2.5}$  for a collisional cascade starting with a mono-disperse (‘md’) set of planetesimals with  $r_0 = 100$  km,  $Q_D^* = 6 \times 10^7$  erg g $^{-1}$ ,  $b_d = 1$ ,  $m_{l,0} = 0.2$ , and  $b_l = 0$  (as indicated in the upper left corner for this and subsequent plots). The legend in the lower right corner indicates the evolution time in Myr. The grey line shows the predicted relative size distribution when  $N(> r) \propto r^{-2.5}$ . Aside from the gradual loss of large objects ( $r \gtrsim 1$  km) due to collisional erosion, the cumulative relative size distribution is nearly independent of time.



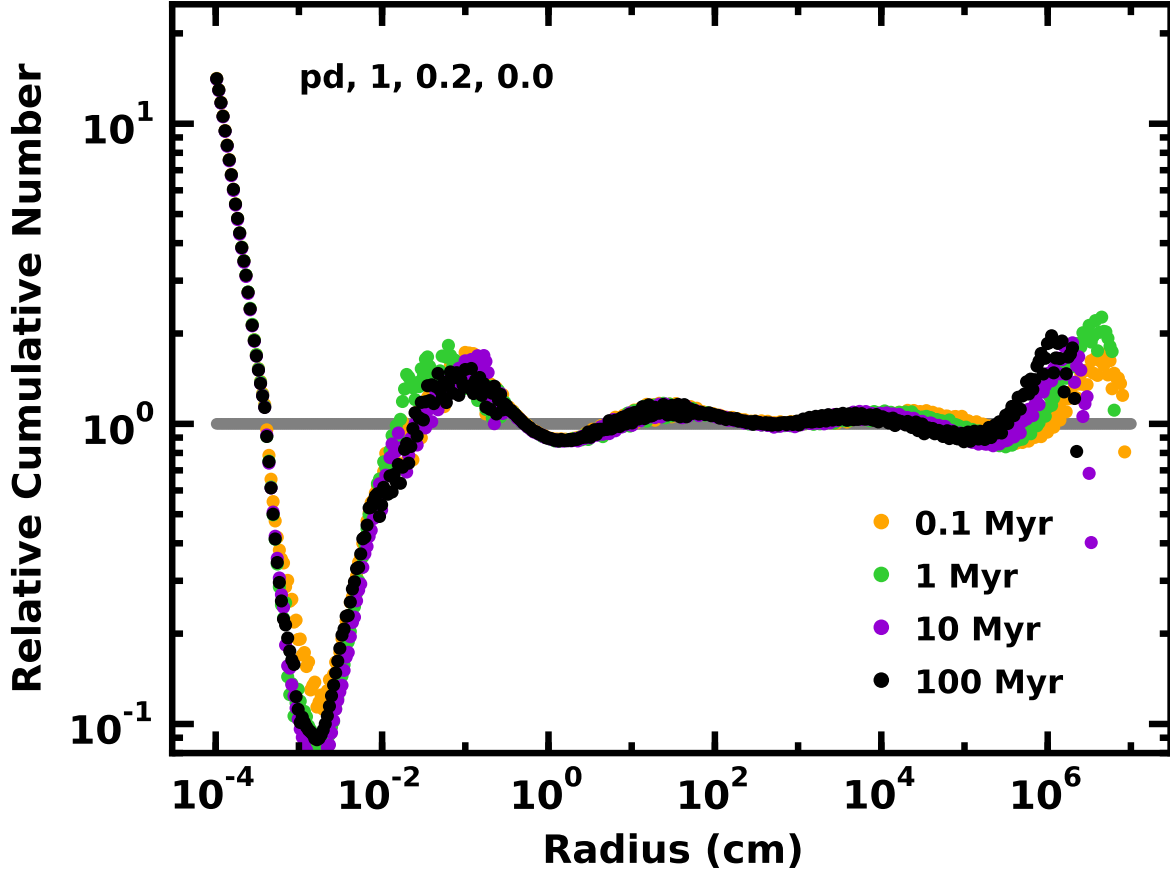


Fig. 4.— As in Fig. 3 for a cascade with an initial power-law size distribution (‘pd’,  $q_0 = 3.5$ ) from  $1 \mu\text{m}$  to  $100 \text{ km}$ . Compared to calculations starting with a mono-disperse set of large objects, the amplitude of the wave at  $r \approx 10 \text{ km}$  is smaller.

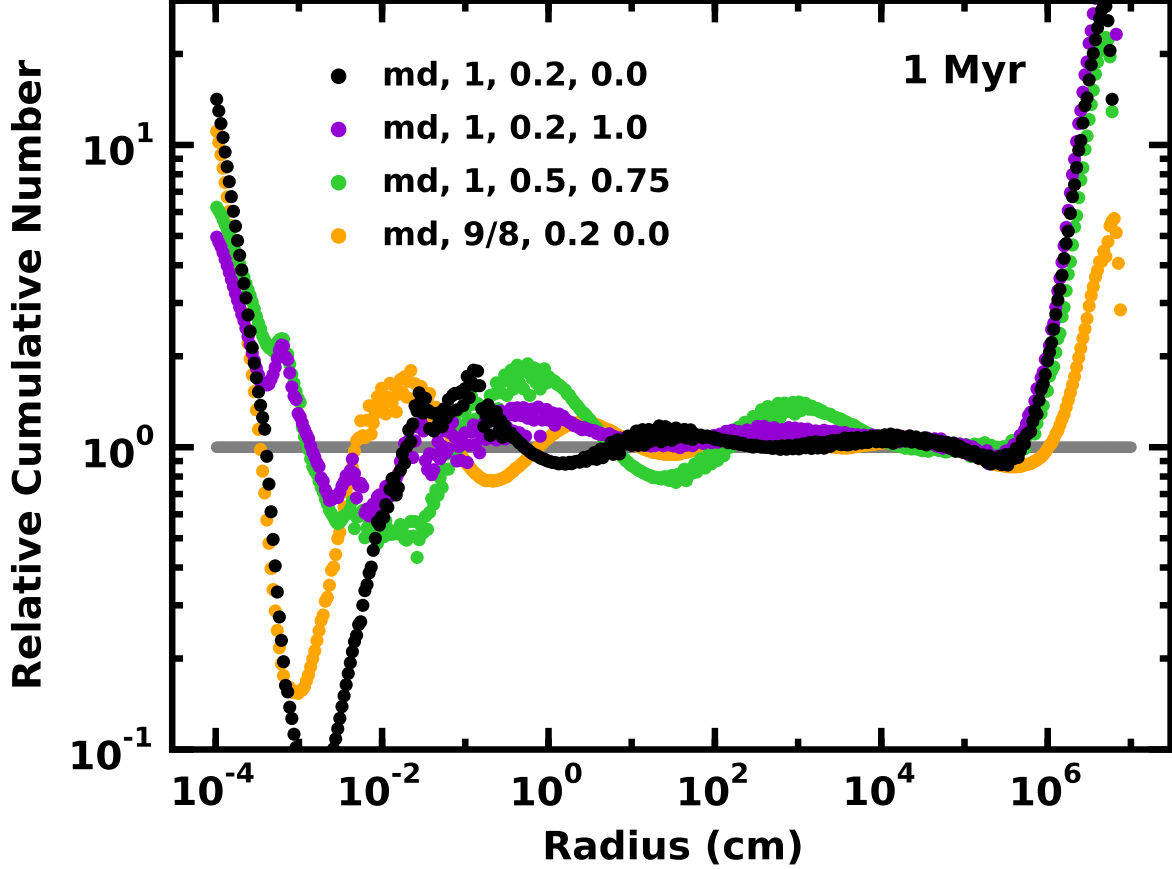


Fig. 5.— Comparison of  $n_{rel}( > r )$  at 1 Myr for calculations with a mono-disperse set of large planetesimals ( $r_0 = 100\ \text{km}$ ) and  $Q_D^* = 6 \times 10^7\ \text{erg g}^{-1}$ . The legend indicates the type of initial size distribution and values for the input parameters  $b_d$ ,  $m_{l,0}$ , and  $b_l$ . Relative to a power-law size distribution with  $N(> r) \propto r^{-2.5}$ , all curves have a similar morphology at 1 Myr: an excess of  $1\text{--}10\ \mu\text{m}$  particles, a deficit of  $10\text{--}100\ \mu\text{m}$  particles, a wavy behavior from  $100\ \mu\text{m}$  to  $10\ \text{km}$ , an excess of  $10\text{--}30\ \text{km}$  particles, and a deficit of  $30\text{--}100\ \text{km}$  particles. Although the fine details of the shape depend on the input parameters, the shape for each set of input parameters is independent of time (see also Figs. 3–4).

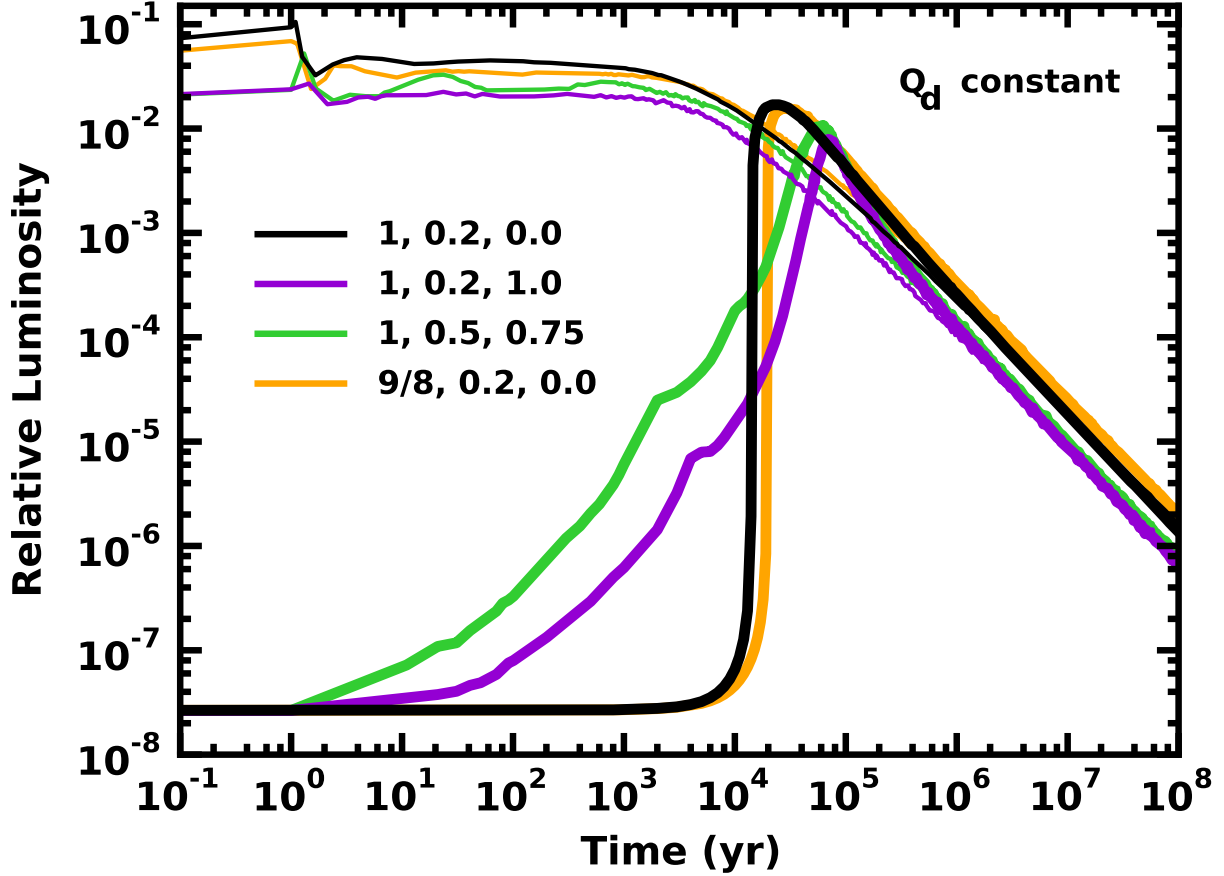


Fig. 6.— Evolution of the relative dust luminosity  $L_d/L_*$  for the calculations in Fig. 2. Starting from a mono-disperse ensemble of planetesimals (thick lines),  $L_d/L_*$  rises rapidly from roughly zero to  $\sim 10^{-2}$  and then declines roughly linearly with time. When calculations begin with a power-law size distribution of planetesimals (thin lines),  $L_d/L_*$  fluctuates about a constant as the size distribution reaches an equilibrium and then declines roughly linearly with time. Although the evolution of  $L_d/L_*$  at late times depends on  $b_d$ ,  $m_{l,0}$ , and  $b_l$  (as indicated in the legend), it is insensitive to the shape of the initial size distribution.

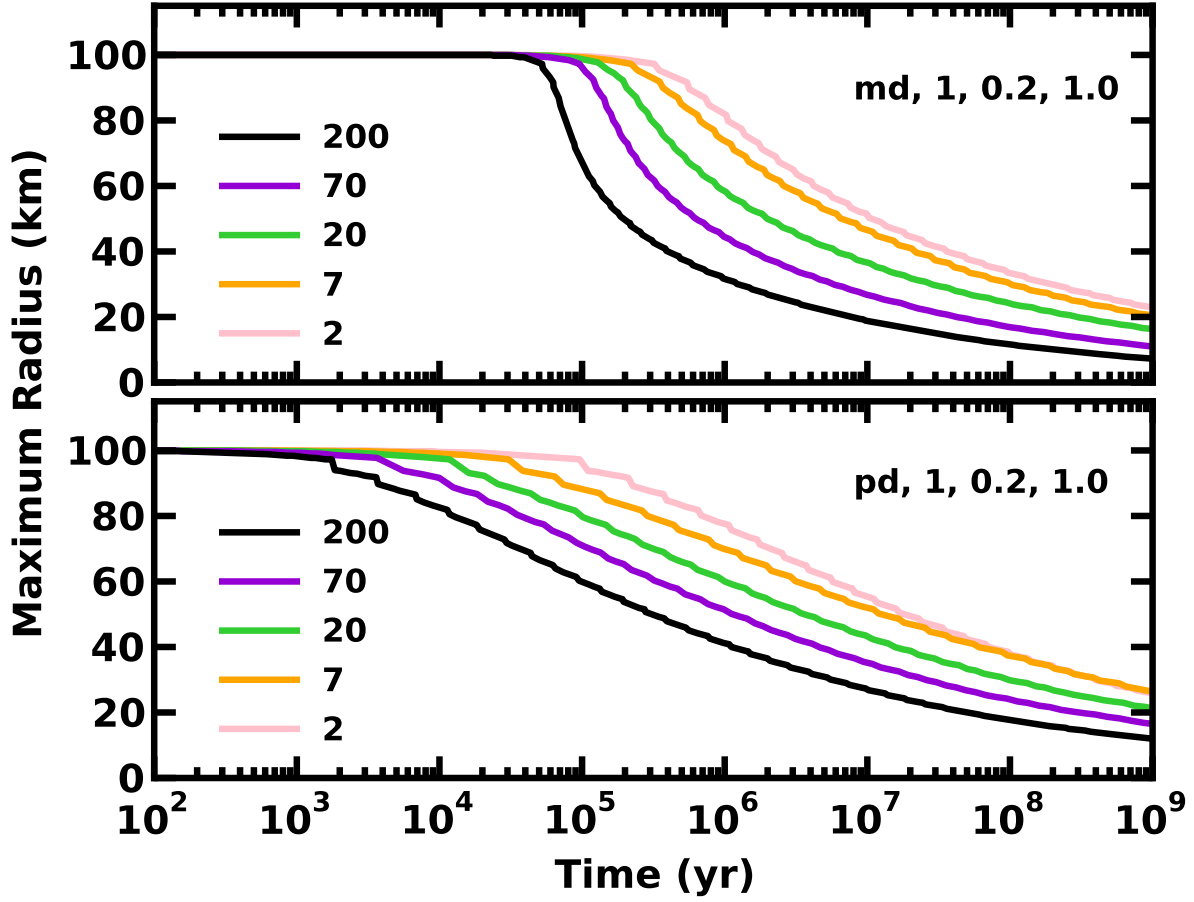


Fig. 7.— Evolution of  $r_{max}$  for cascade models with constant  $Q_D^*$ ,  $b_d = 1$ ,  $m_{l,0} = 0.2$ ,  $b_l = 1.0$ , initially mono-disperse (‘md’, upper panel) or power-law (‘pd’, lower panel) size distributions, and various ratios  $v^2/8Q_D^*$  as indicated in the legend on the left side of each panel. Systems with larger  $v^2/8Q_D^*$  have shorter collision time scales.

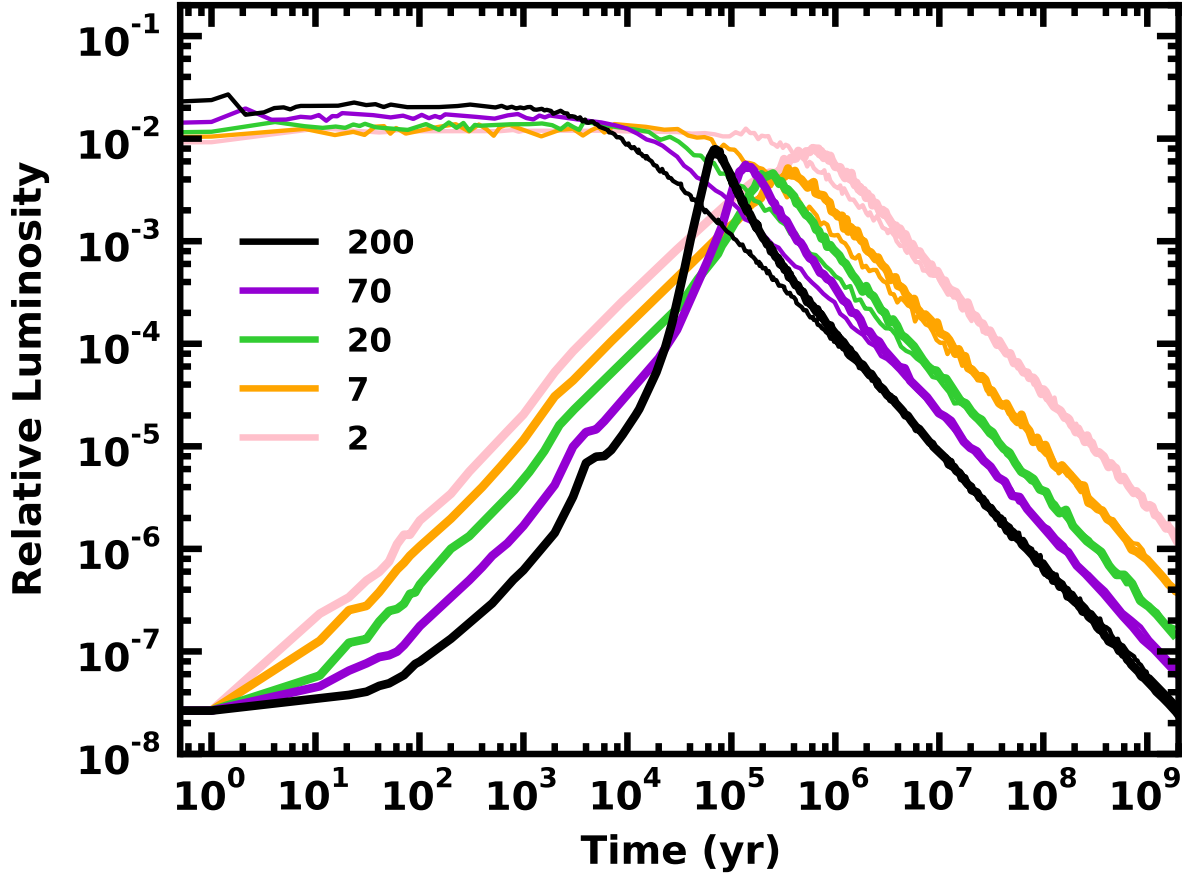


Fig. 8.— Evolution of  $L_d/L_\star$  for cascade models with various ratios  $v^2/8Q_D^*$  as in Fig. 7. Although the peak luminosity is fairly independent of  $v^2/8Q_D^*$ , systems with larger ratios reach peak luminosity earlier in time. Independent of the initial size distribution, systems with smaller  $v^2/8Q_D^*$  ratios have larger relative luminosity at late times.

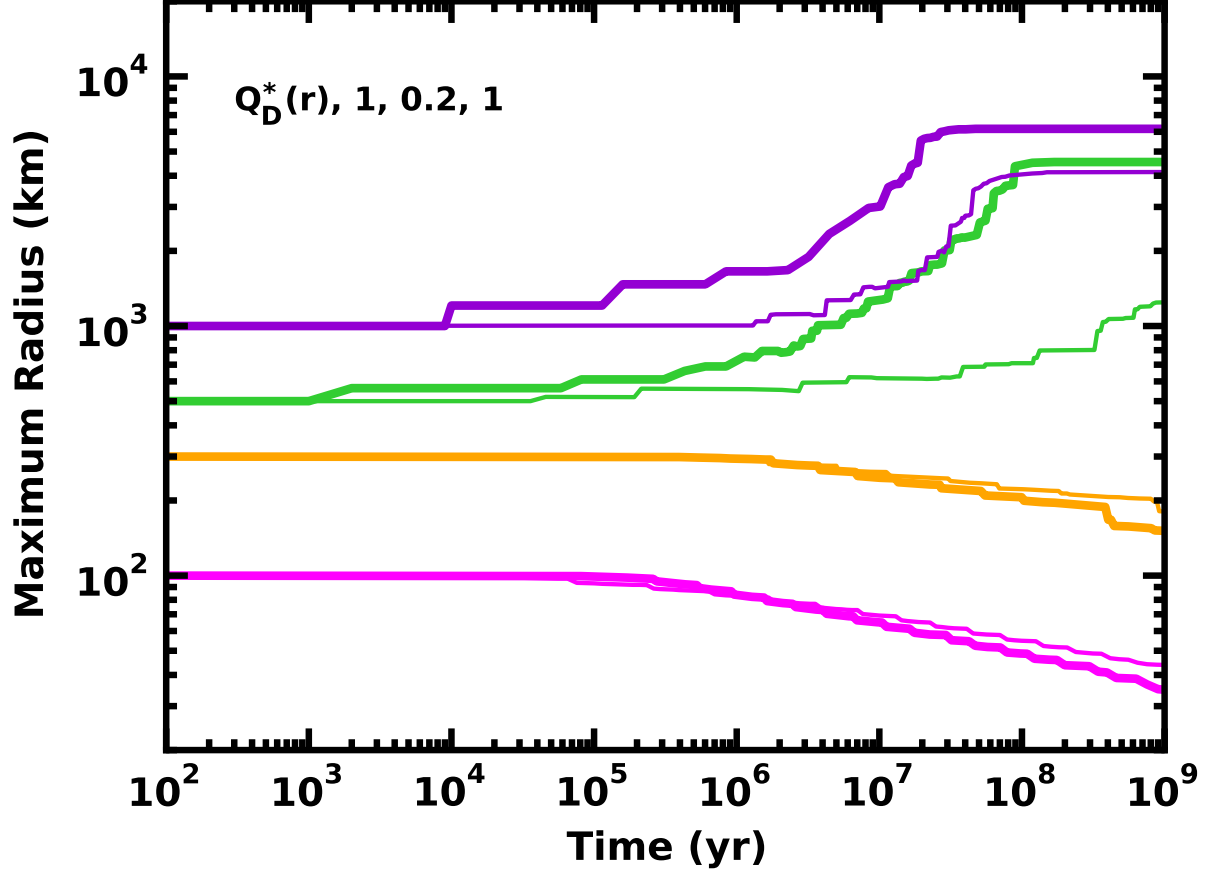


Fig. 9.— Evolution of  $r_{max}$  for cascade models with  $Q_D^*(r)$ ,  $b_d = 1$ ,  $m_{l,0} = 0.2$ ,  $b_l = 1$ , initially mono-disperse (thick lines) or power-law (thin lines) size distributions, and various  $r_0$ . The boundary between growth and destructive evolution is at  $r_0 \approx 400$  km.

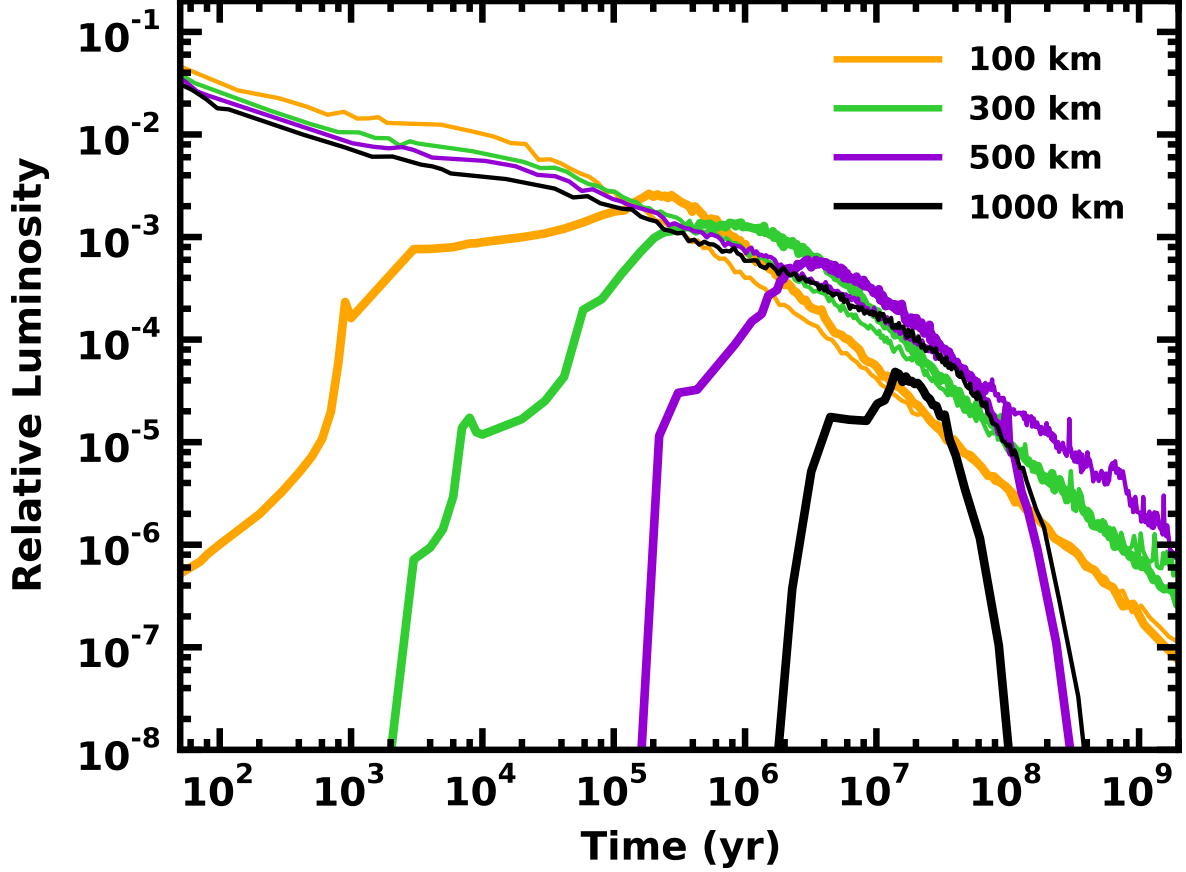


Fig. 10.— Evolution of  $L_d/L_*$  for cascade models with various  $r_0$  (in km) as indicated in the legend and mono-disperse (thick lines) or power-law (thin lines) initial size distributions. When the largest objects grow through mergers, originally mono-disperse swarms have minimal  $L_d$  for short periods of time. In swarms with an power law initial size distribution,  $L_d$  is fairly well-correlated with  $r_0$ .

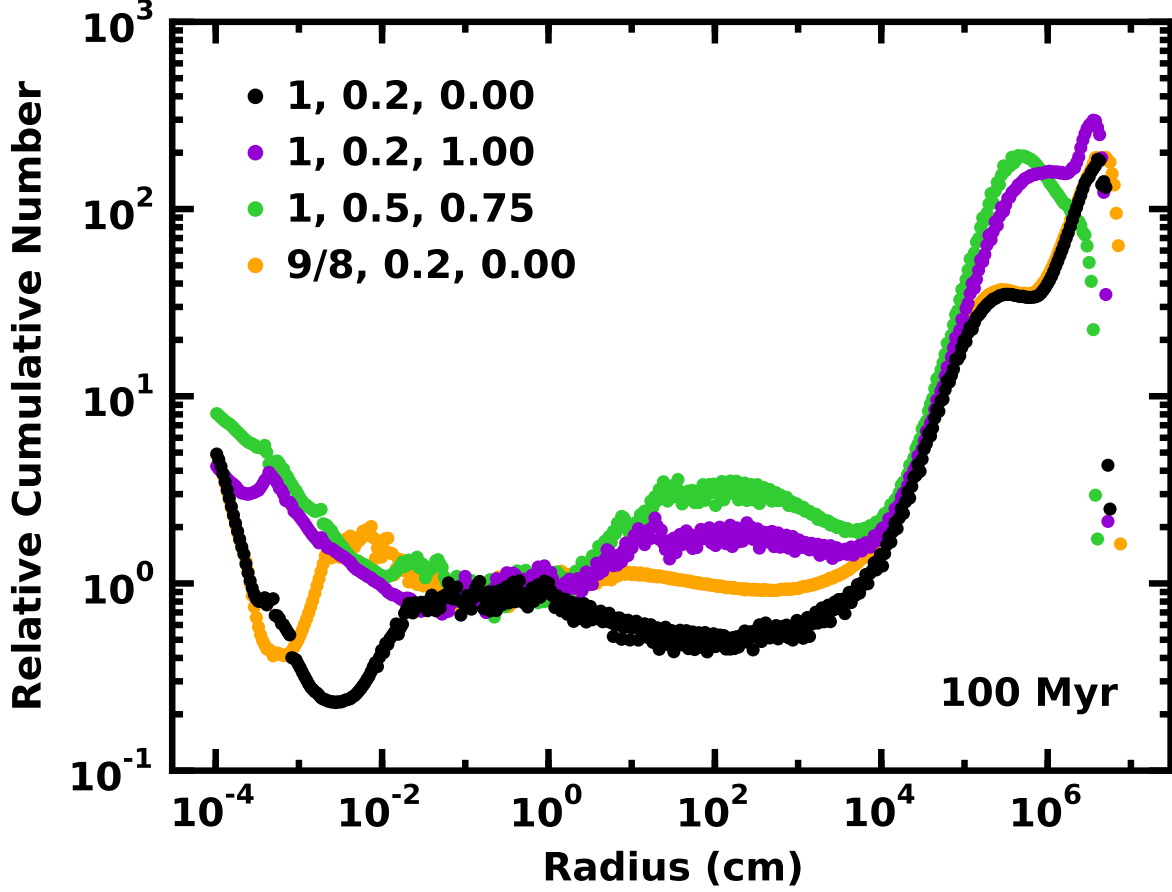


Fig. 11.— Relative cumulative size distributions at 100 Myr for cascade models with a mono-disperse initial size distribution,  $Q_D^*(r)$ ,  $r_0 = 100$  km, and various  $b_d$ ,  $m_{l,0}$ , and  $b_l$  as indicated in the legend. Relative to a power-law size distribution with  $N(> r) \propto r^{-2.68}$ , all curves have a wavy morphology with distinct excesses of particles at  $r \approx 1\text{--}10 \mu\text{m}$  and  $r \gtrsim 0.1$  km. The rise in the relative cumulative size distribution occurs at the minimum in  $Q_D^*$  at 0.1 km. Although the fine details of the shape depend on the input parameters, the shape for each set of input parameters is independent of time for  $t \gtrsim 1$  Myr (see also Figs. 3–5).



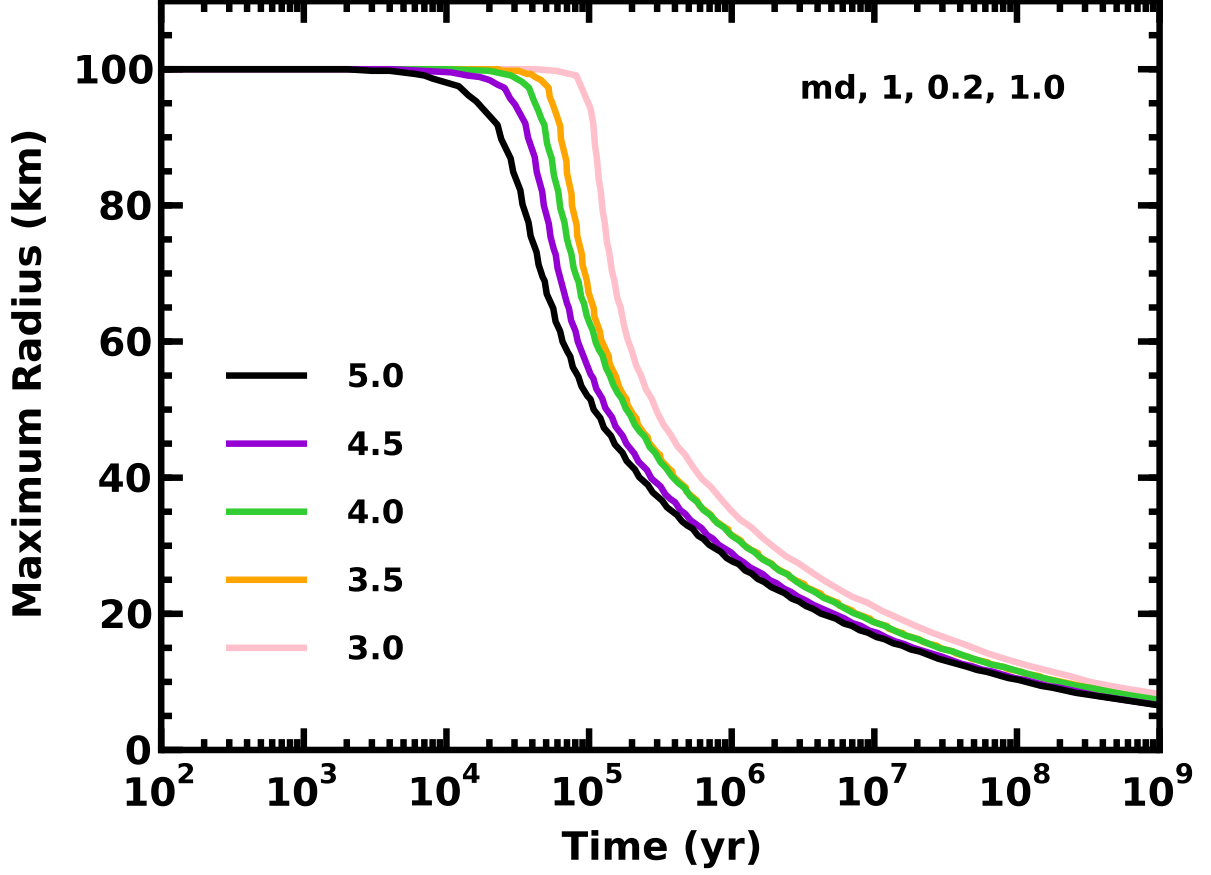


Fig. 12.— Evolution of  $r_{max}$  for cascade models with a mono-disperse initial size distribution,  $b_d = 1$ ,  $m_{l,0} = 0.2$ , and  $b_l = 1.0$  (as indicated in the legend in the upper right corner) and various  $q_d$  as indicated in the legend in the lower left corner. In simulations with larger  $q_d$ , the largest objects reach smaller sizes at late times.

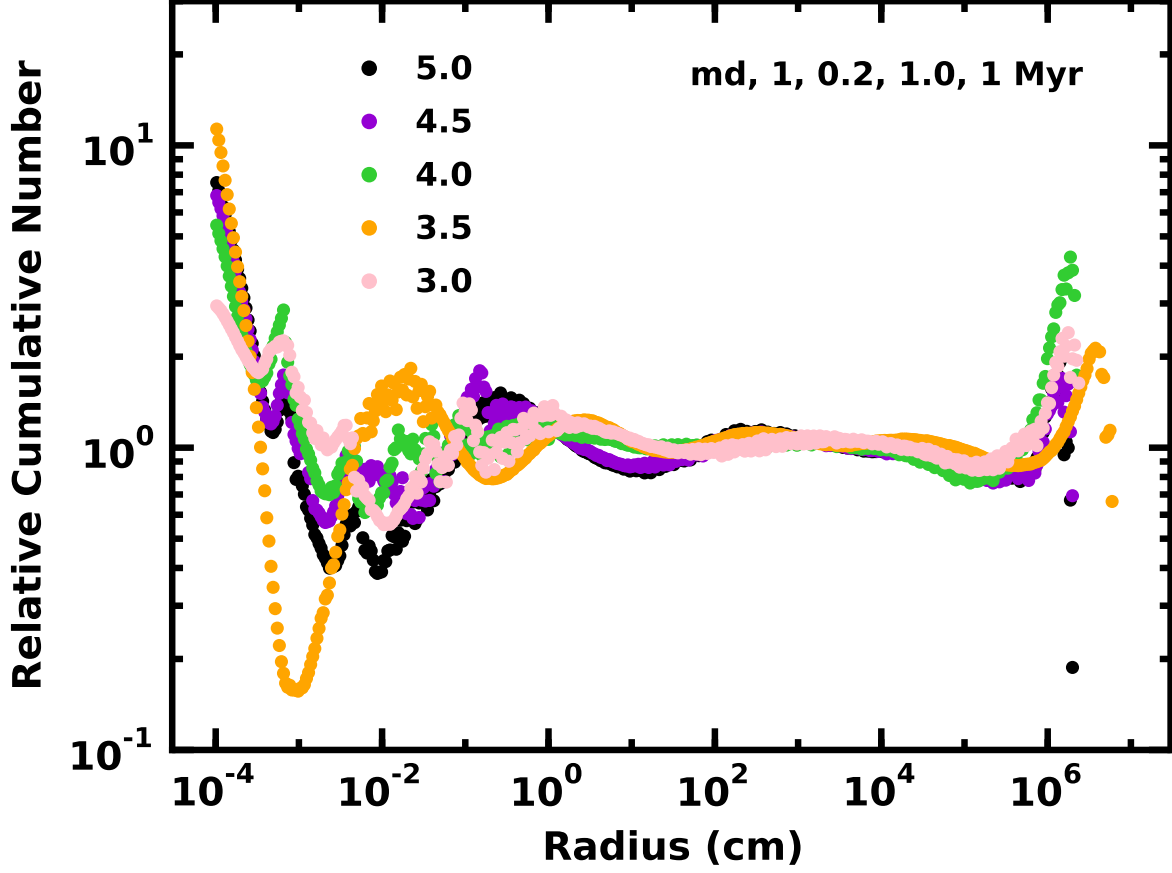


Fig. 13.— Relative cumulative size distributions at 1 Myr for mono-disperse cascade models with  $b_d = 1$ ,  $m_{l,0} = 0.2$ ,  $b_l = 0.1$  and various  $q$  as indicated in the legend. Aside from the morphology of the waviness for  $r \approx 1 \mu\text{m}$  to 10–100 cm, the size distribution is independent of  $q$ .

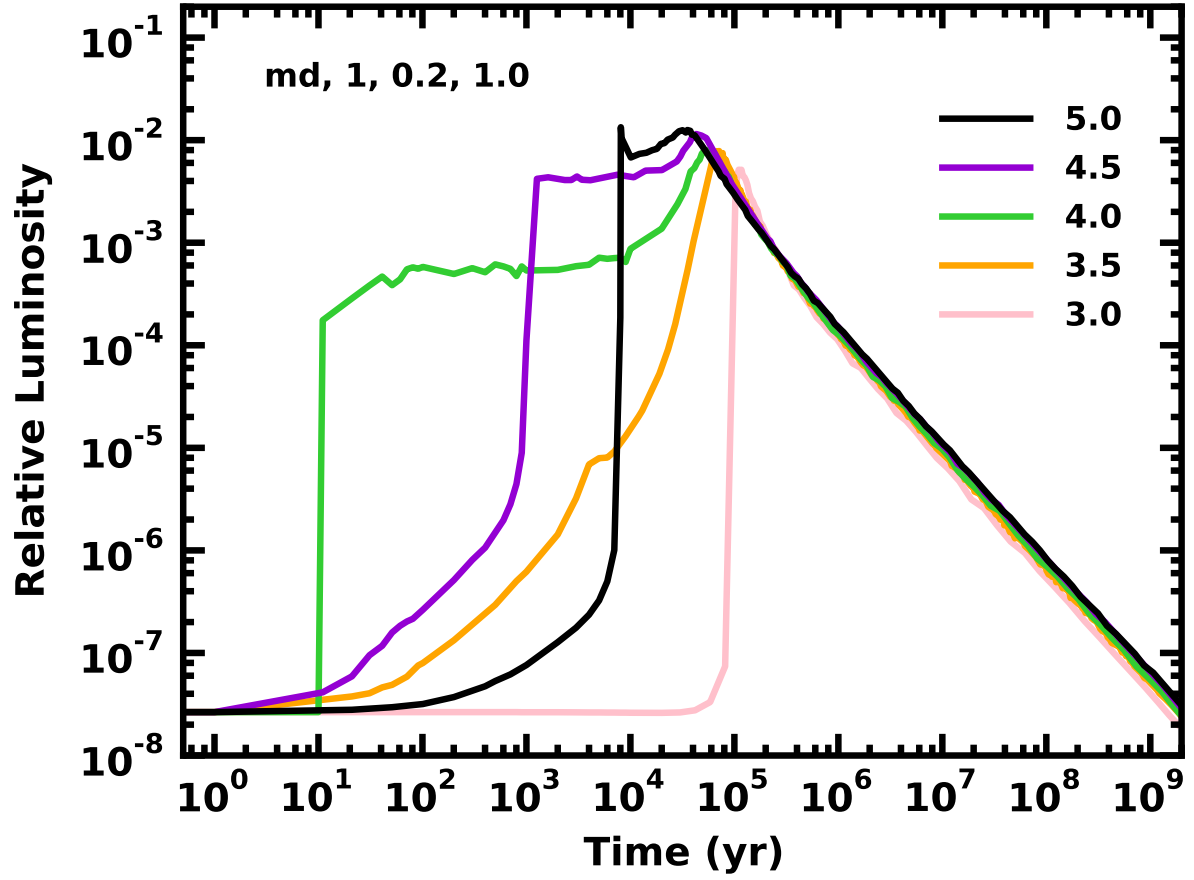


Fig. 14.— Evolution of  $L_d/L_\star$  for the mono-disperse cascade models in Figs. 12– 13. Systems with larger  $q_d$  reach larger  $L_d$  and decline more slowly than systems with smaller  $q_d$ .

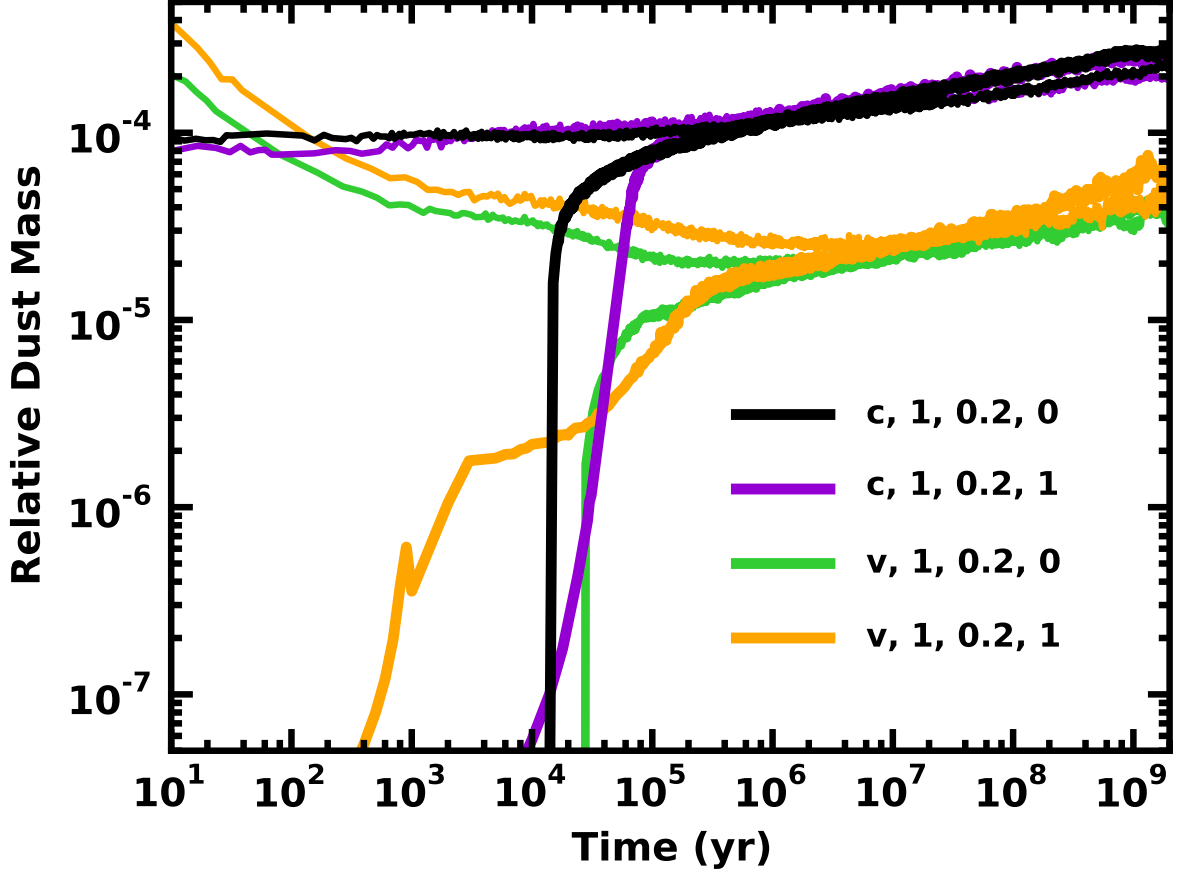


Fig. 15.— Time evolution of the relative dust mass  $\xi$  for collisional cascades with mono-disperse (thick lines) and power law (thin lines) initial size distributions. The legend indicates the prescription for  $Q_D^*$  ('c' for constant and 'v' for  $Q_D^*(r)$ ) and values for  $b_d$ ,  $m_{l,0}$ , and  $b_l$ . On time scales longer than the collision time, the relative dust mass slowly grows with time. Although  $\xi$  depends on  $Q_D^*$ , it is fairly independent of the initial size distribution and other fragmentation parameters.

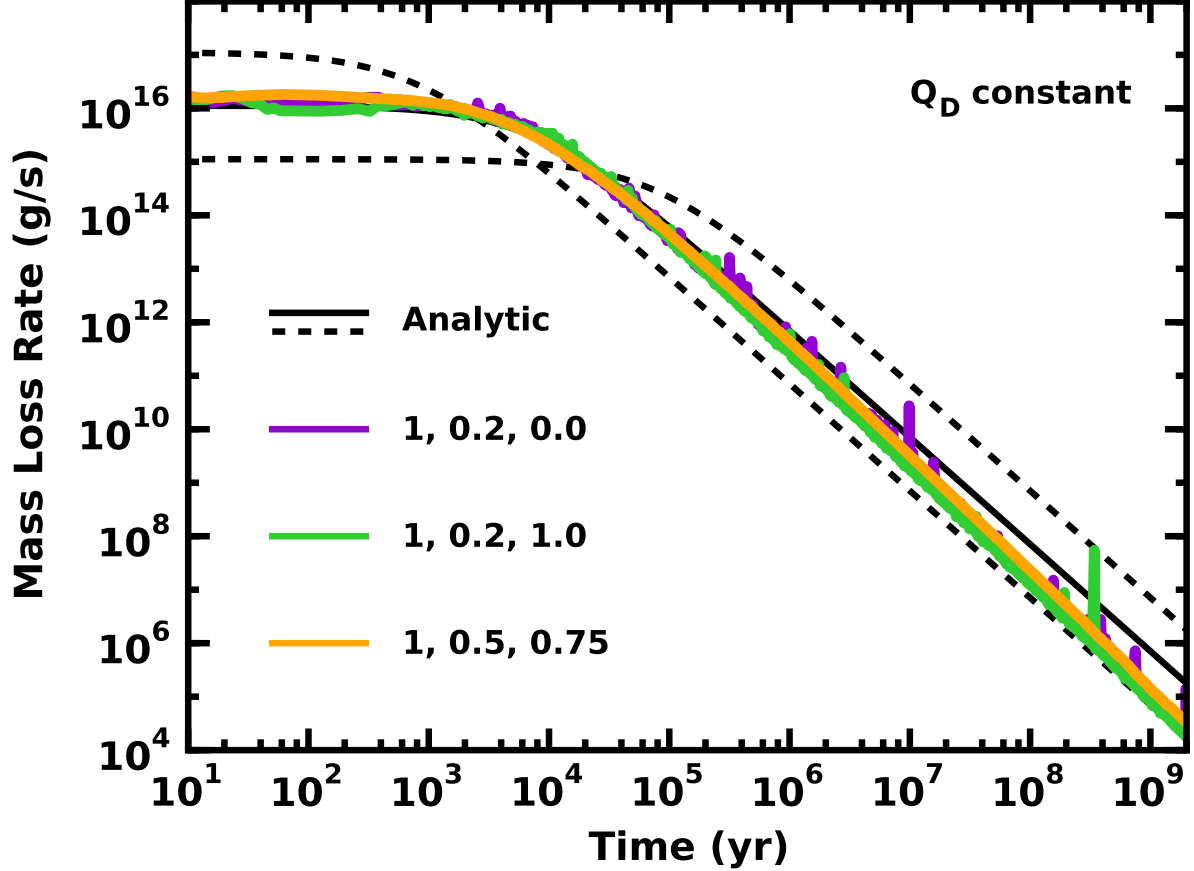


Fig. 16.— Comparison of the mass loss rate from numerical simulations with the analytic model. The legend indicates values of  $b_d$ ,  $m_{l,0}$ , and  $b_l$  for simulations with a constant  $Q_D^* = 6 \times 10^7 \text{ erg g}^{-1}$ . The black lines plot predictions from the analytic model for  $\alpha = 1$  (upper dashed), 0.1 (solid), and 0.01 (lower dashed). Colored lines plot results for calculations with an initial power law size distribution. Although the numerical estimates match the analytic prediction for the mass loss rate with  $\alpha = 0.1$  at early times, they decline with time more rapidly than the analytic result. Occasional spikes in the mass loss rate result from occasional collisions of large objects.

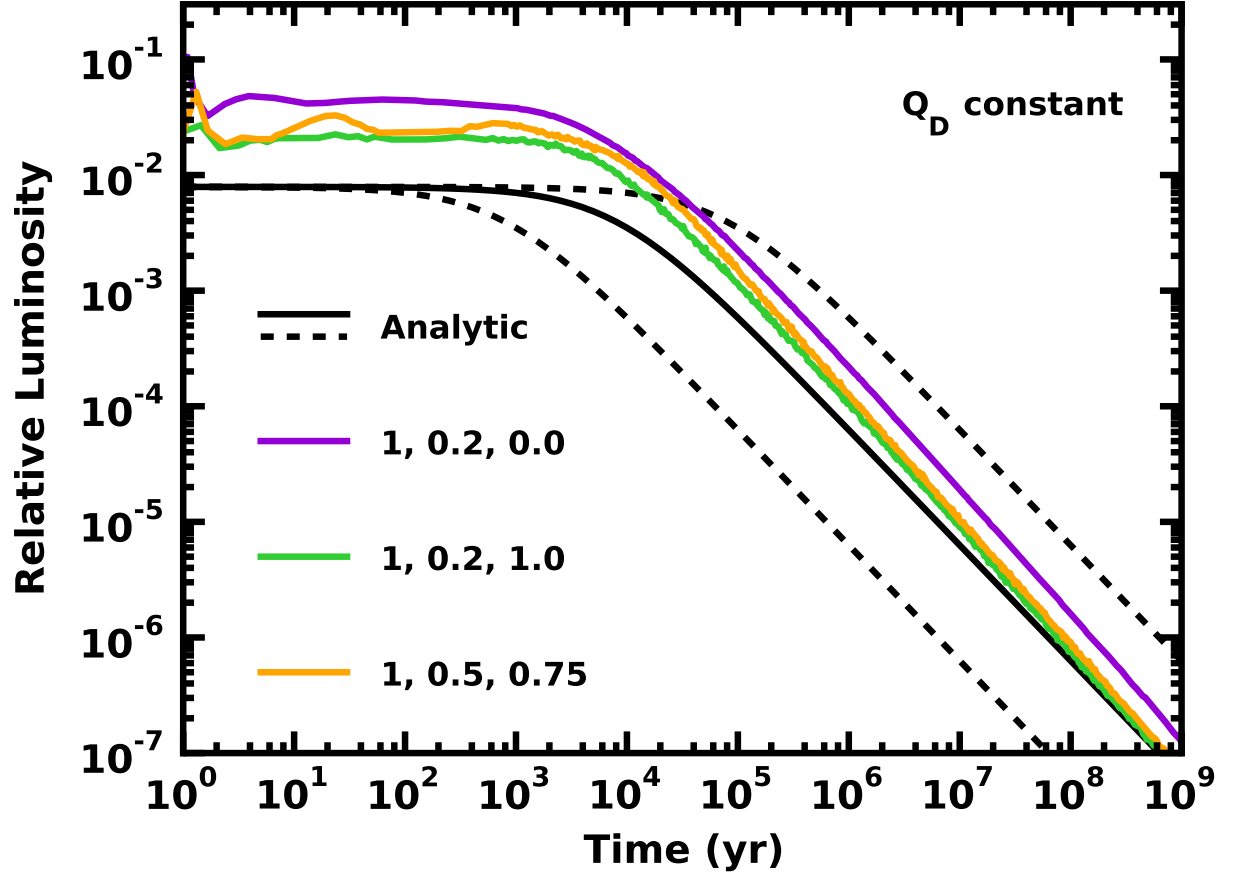


Fig. 17.— Comparison of the relative luminosity  $L_d/L_*$  from numerical simulations with the analytic model. Despite the random spikes in the mass loss rate (see Fig. 16), the luminosity declines smoothly with time.

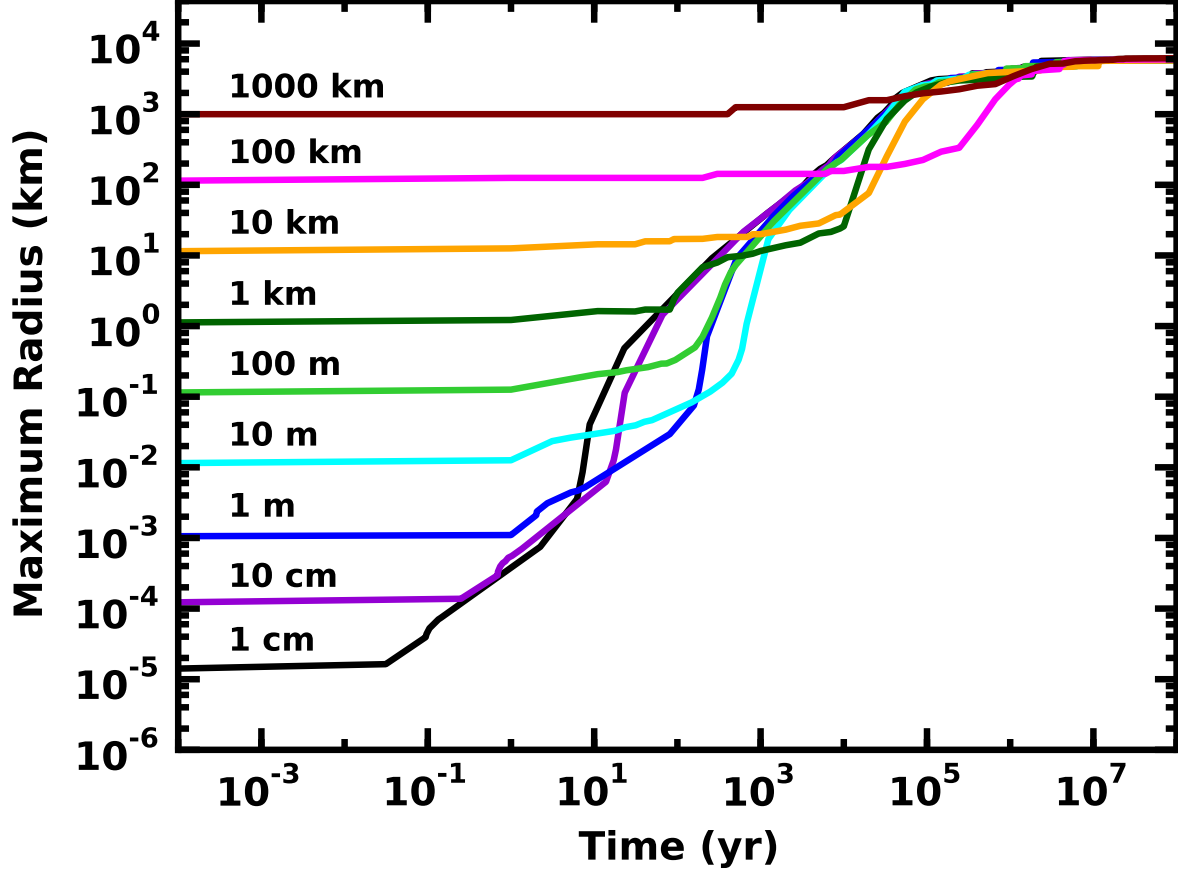


Fig. 18.— Growth of the largest object in a suite of planet formation calculations with  $\Sigma_0 = 10 \text{ g cm}^{-2}$  in an annulus with  $\delta a = 0.2 \text{ AU}$  at  $a = 1 \text{ AU}$ . Labels indicate the initial radius  $r_0$  of a mono-disperse set of objects. Swarms with small  $r_0$  evolve more rapidly than those with large  $r_0$ . After 0.1–1 Myr, all swarms produce a few objects with radii exceeding 3000 km. This final radius is independent of  $r_0$ .

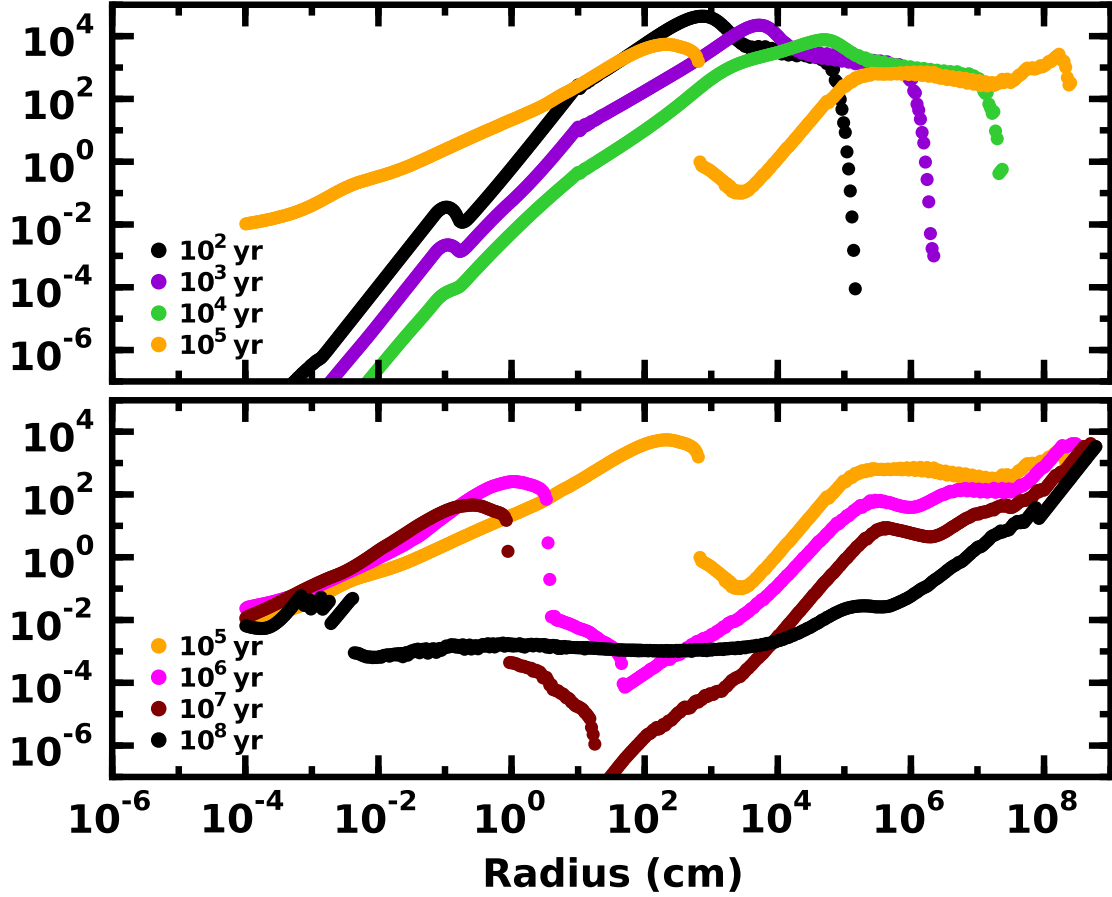


Fig. 19.— Evolution of the relative cumulative size distribution ( $N(> r)/n_0 r^{-2.5}$ , with  $n_0 = 10^{20}$ ) for a planet formation calculation with  $\Sigma_0 = 10 \text{ g cm}^{-2}$  and  $r_0 = 10 \text{ cm}$ . In each panel, the legend indicates the evolution time in yr. To aid in the comparison at late times, both panels include the size distribution at  $10^5 \text{ yr}$  (orange points). From  $10^2 \text{ yr}$  to  $10^4 \text{ yr}$  (upper panel; black, violet, and green points), the largest object grows from 1 km to 100 km and sweeps up smaller particles in the debris tail. As objects grow from 100 km to 1000 km (0.01–1 Myr, green, orange, and magenta points), collisions produce a prominent debris tail at sizes of 100 cm and smaller. Continued evolution produces a significant deficit of particles at sizes ranging from 1 cm to 1 km (1–10 Myr; magenta and maroon points). Eventually collisions remove most particles smaller than  $\sim 100 \text{ km}$  (100 Myr; black points).



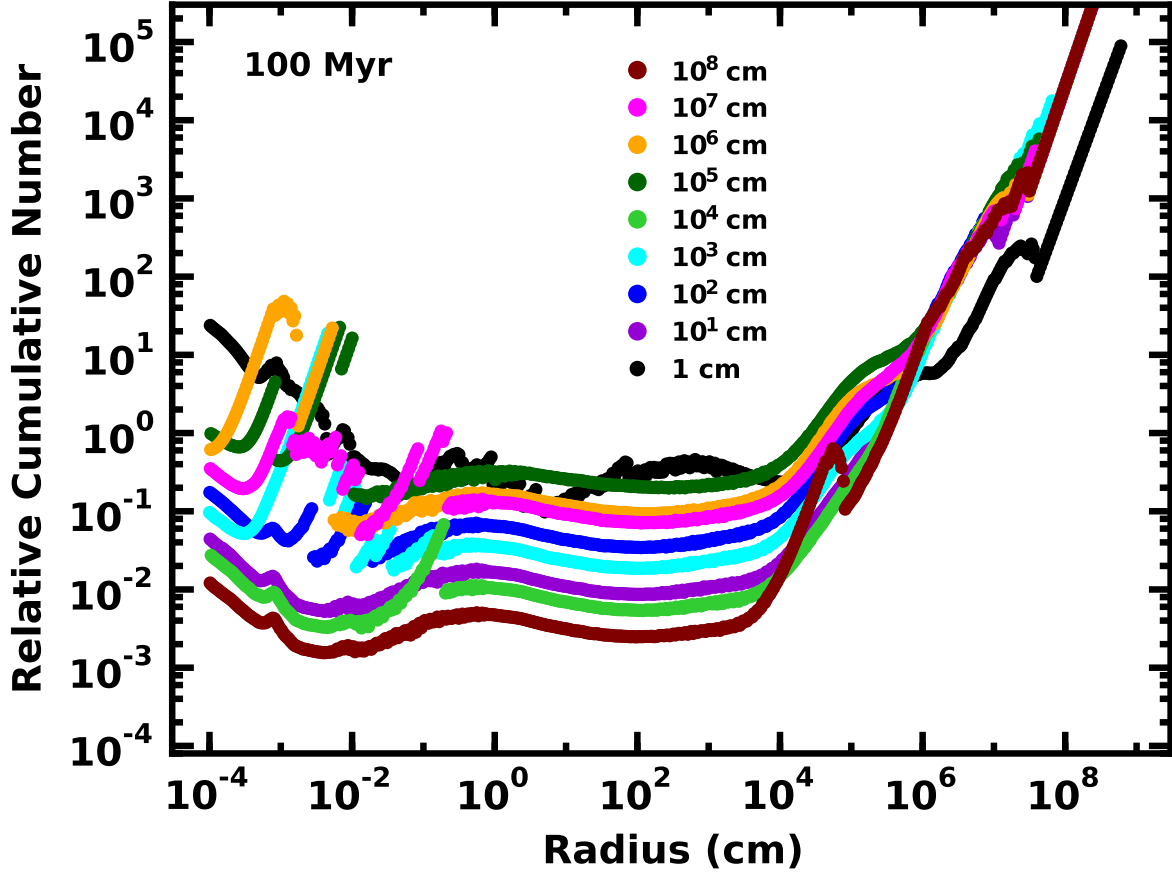


Fig. 20.— Comparison of relative cumulative size distributions at 100 Myr for calculations with  $\Sigma_0 = 10 \text{ g cm}^{-2}$  at 1 AU for various  $r_0$  (in cm) as indicated in the legend. At  $r \gtrsim 10 \text{ km}$ , all starting points lead to the same size distribution. For 0.1 cm to 10 km, the size distributions are nearly identical except for a modest offset which depends on the complete collision history but not on  $r_0$ . The relative abundance of particles with sizes smaller than 0.1 cm depends on the recent history of collisions between large objects with radii of 10–1000 km.

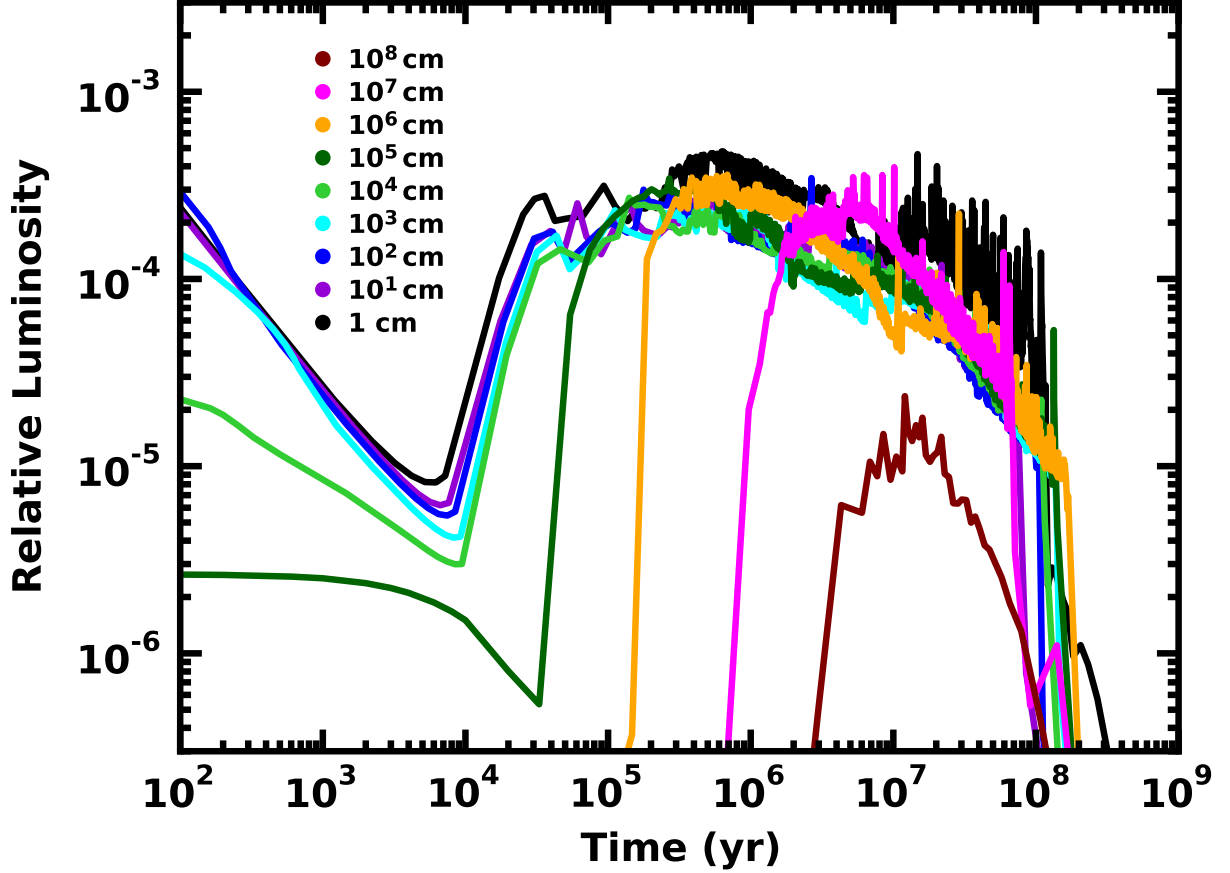


Fig. 21.— Evolution of the dust luminosity for the calculations in Fig. 18. The legend indicates  $r_0$  (in cm) for each calculation. At early times, particle growth dramatically reduces the ratio of the surface area to the mass for the entire swarm. The dust luminosity declines. Once the collisional cascade begins, the dust luminosity rises rapidly. Despite different rise times for calculations with different  $r_0$ , the maximum dust luminosity is fairly independent of  $r_0$ . At late times, the evolution consists of spikes from giant impacts superposed on a slow decline in  $L_d$ .

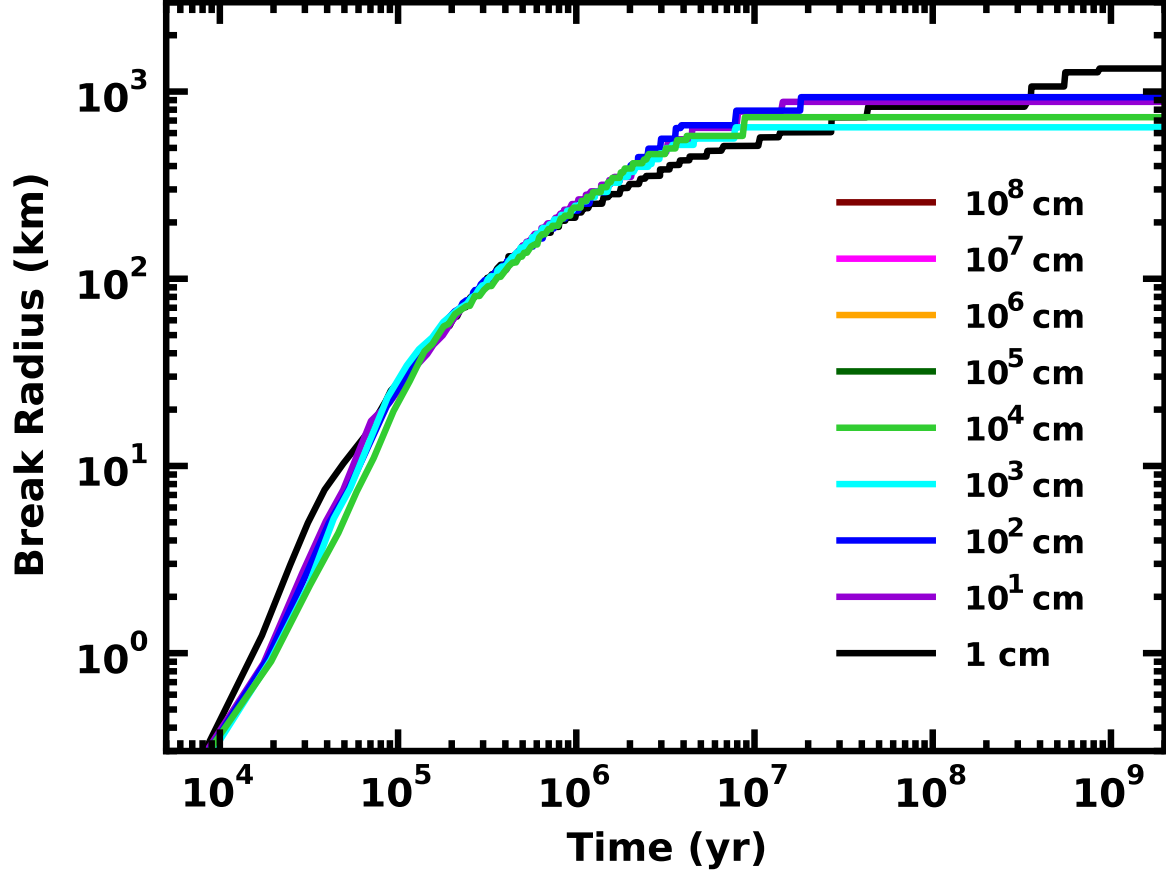


Fig. 22.— Time evolution of  $r_{brk}$  for planet formation simulations with various  $r_0$  as indicated in the legend. Independent of  $r_0$ ,  $r_{brk}$  gradually increases with time and then reaches a plateau at  $r_{brk} \approx 1000$  km.

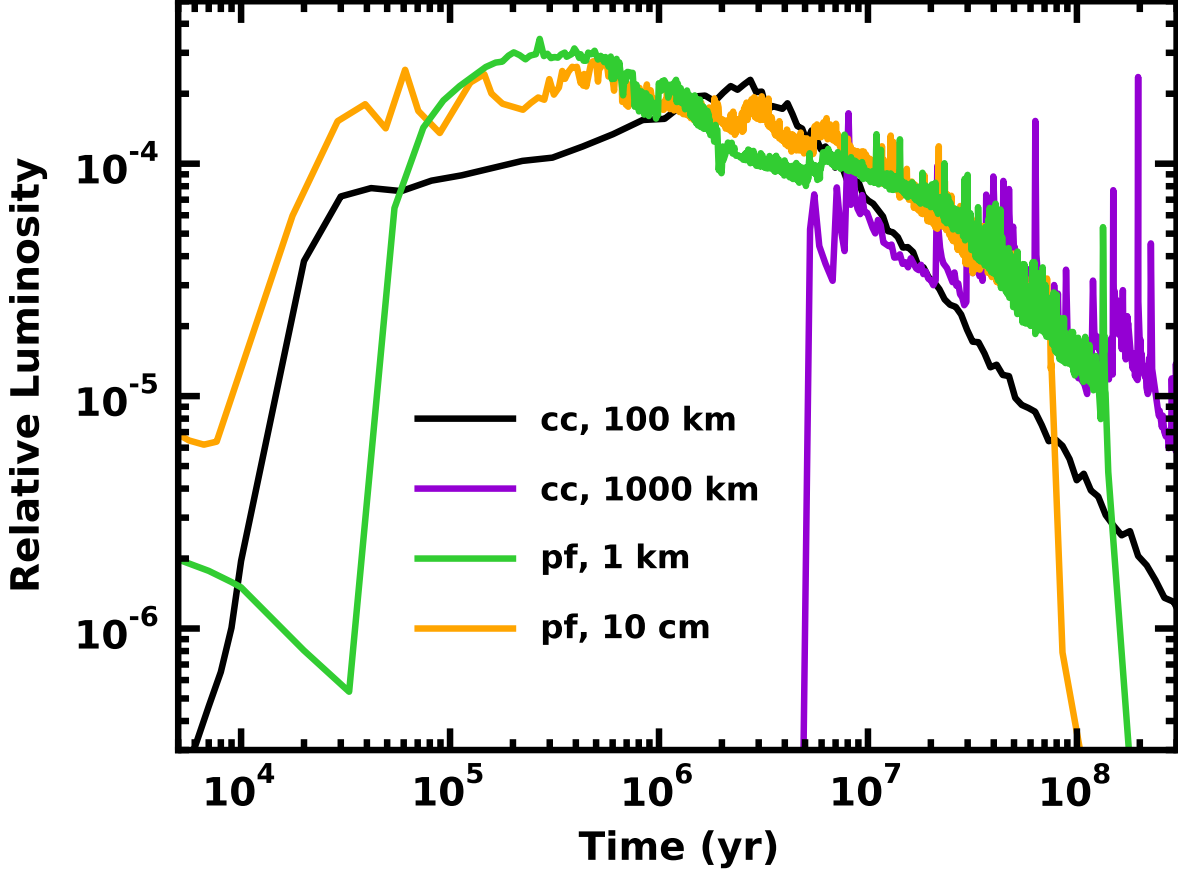


Fig. 23.— Comparison of  $L_d/L_\star$  for two collisional cascade calculations (black and violet curves, with  $r_0$  listed in the legend) and two planet formation calculations from Fig. 21 (green and orange curves, with  $r_0$  listed in the legend). At early times ( $\lesssim 10$  Myr), three calculations produce similar  $L_d$ . When  $t = 10$ – $100$  Myr,  $L_d$  from the cascade with  $r_0 = 100$  km is considerably smaller than from the two planet formation models. Despite negligible  $L_d$  at early times, the cascade with  $r_0 = 1000$  km achieves a dust luminosity similar to the planet formation calculations after 30–40 Myr. Once  $t \gtrsim 100$  Myr, planets have removed all of the smaller particles from the annulus;  $L_d$  for these simulations then lies well below the predictions of cascade models.

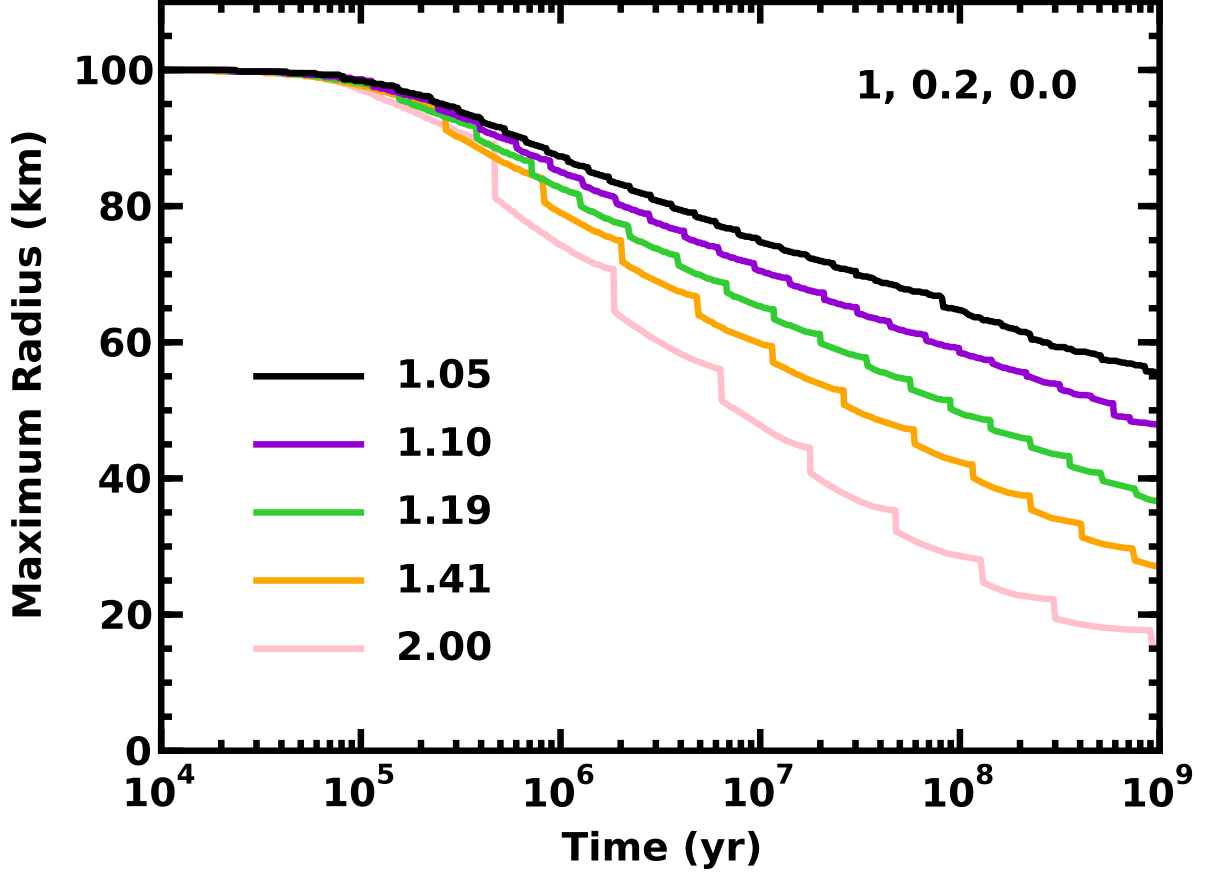


Fig. 24.— Time evolution of  $r_{max}$  in collisional cascades with a mono-disperse ensemble of 100 km objects and no velocity evolution. The legend in the lower left corner indicates the mass spacing factor  $\delta$  for each calculation. In the upper right corner, the legend indicates adopted values for  $b_d$ ,  $m_{l,0}$ , and  $b_l$ . Continuous cratering collisions produce a gradual decline in  $r_{max}$ . Downward jumps in  $r_{max}$  occur when mass loss moves the largest objects into the next smallest mass bin. Calculations with larger  $\delta$  produce larger and less frequent jumps.

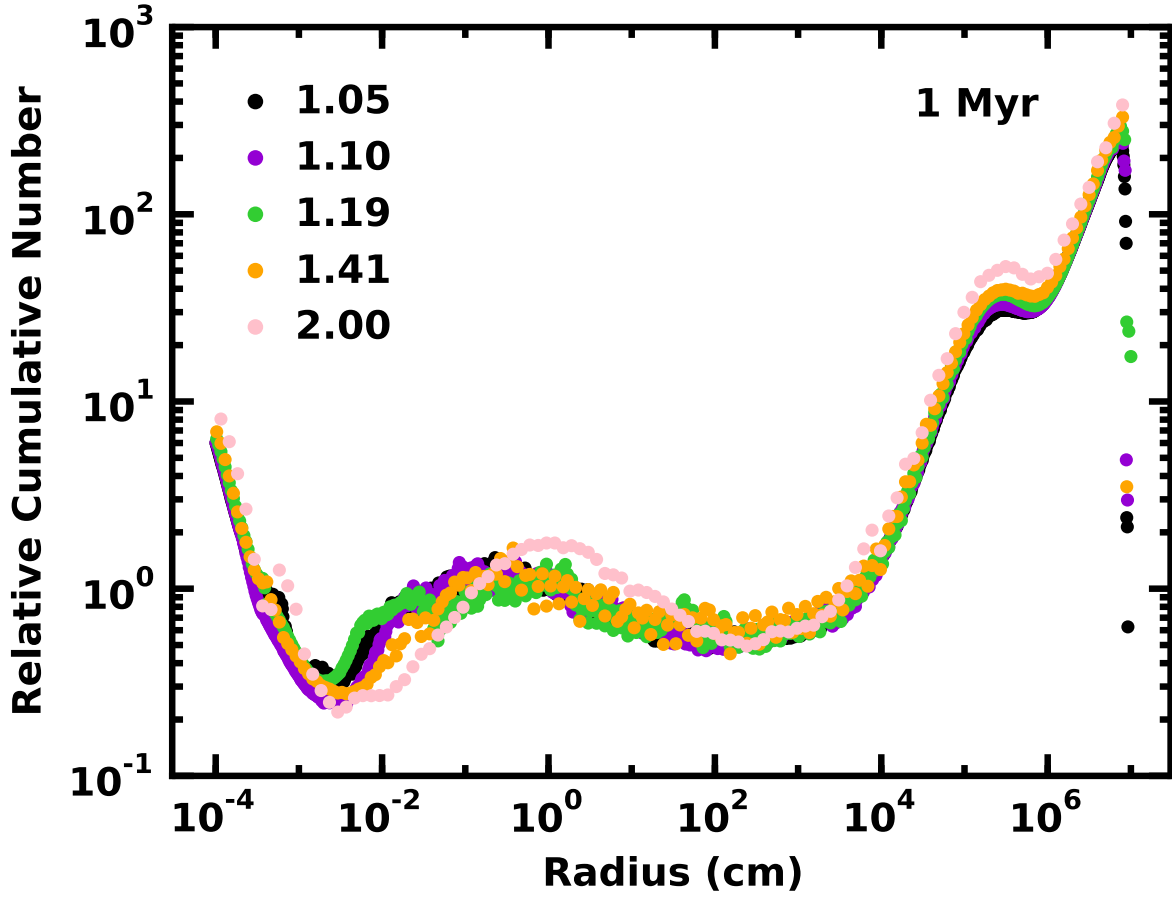


Fig. 25.— Relative cumulative size distributions  $N(> r)/r^{-2.5}$  for collisional cascades at 1 Myr. All of the curves have a similar morphology: (i) an excess for particle sizes  $r \approx 1\text{--}5 \mu\text{m}$ , (ii) a deficit for  $r \approx 5\text{--}50 \mu\text{m}$ , (iii) a constant part for  $r \approx 0.01 \text{ cm}$  to  $0.1 \text{ km}$ , and (iv) a steep rise for  $r \gtrsim 0.1 \text{ km}$  with a small shoulder at  $r \approx 1\text{--}3 \text{ km}$ . Calculations with larger  $\delta$  (as indicated in the legend) have larger fluctuations (waves) about a smooth curve.

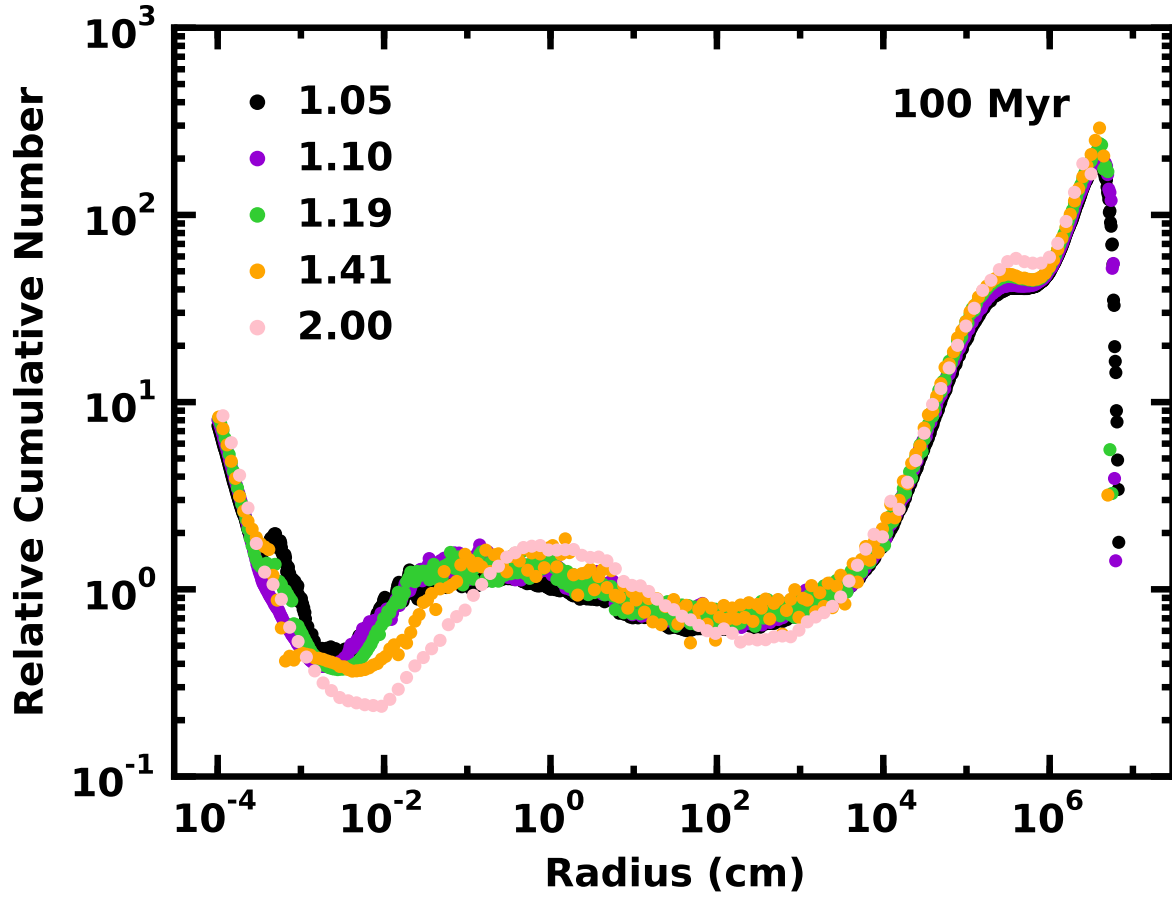


Fig. 26.— As in Fig. 25 for 100 Myr. At later times, calculations with smaller  $\delta$  still have smaller fluctuations relative to calculations with larger  $\delta$ .

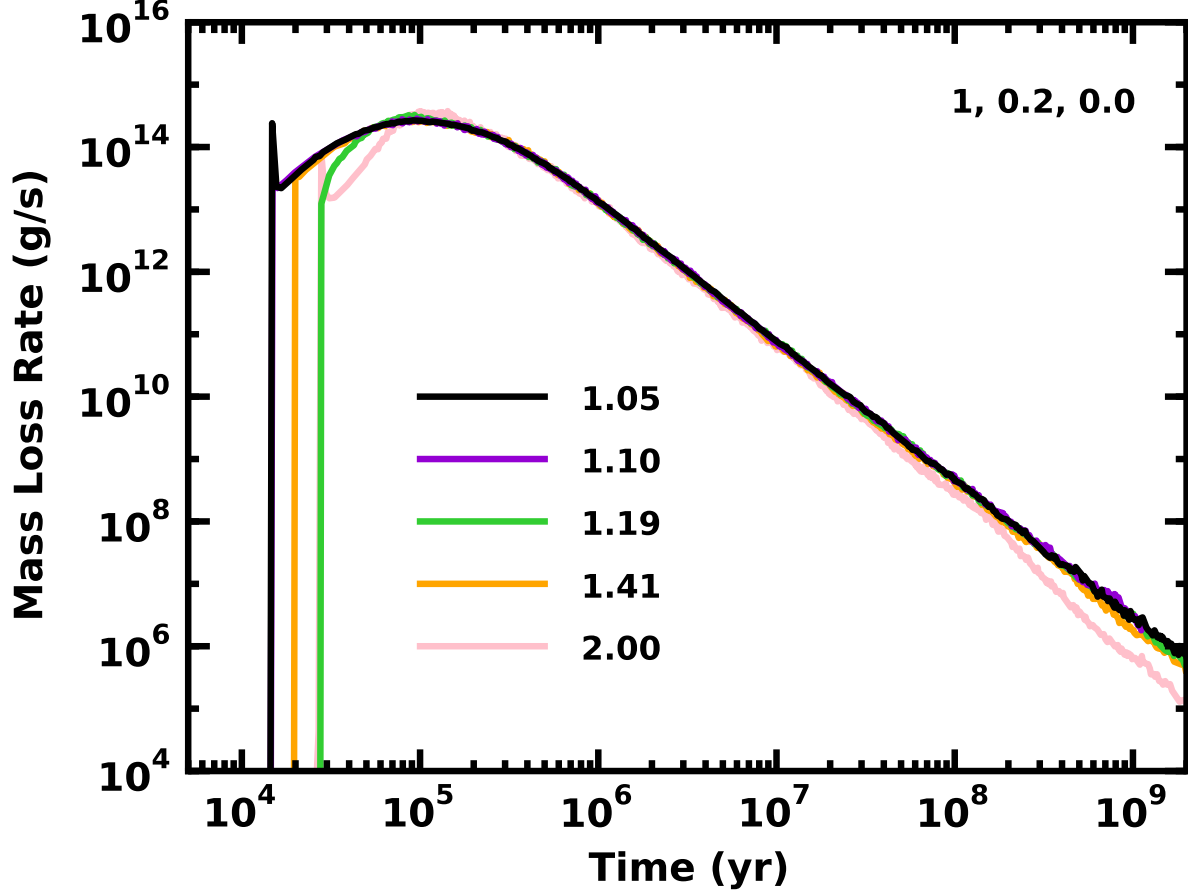


Fig. 27.— Time evolution of the mass loss rate for collisional cascade calculations with a mono-disperse swarm of 100 km particles, no velocity evolution, and different  $\delta$  (as indicated in the legend in the lower left corner). The legend in the upper right corner indicates adopted values for  $b_d$ ,  $m_{l,0}$ , and  $b_l$ . The mass loss rate measures the production rate of objects with  $r < 1 \mu\text{m}$  from collisions between objects with typical radii of 1–100  $\mu\text{m}$ . Starting from an ensemble of 100 km planetesimals, the production rate is initially zero. Destructive collisions among large objects eventually produce sufficient numbers of small particles; the mass loss rate then rises abruptly. Within  $\sim 0.1$  Myr, the mass loss reaches a clear peak and then declines linearly with time.



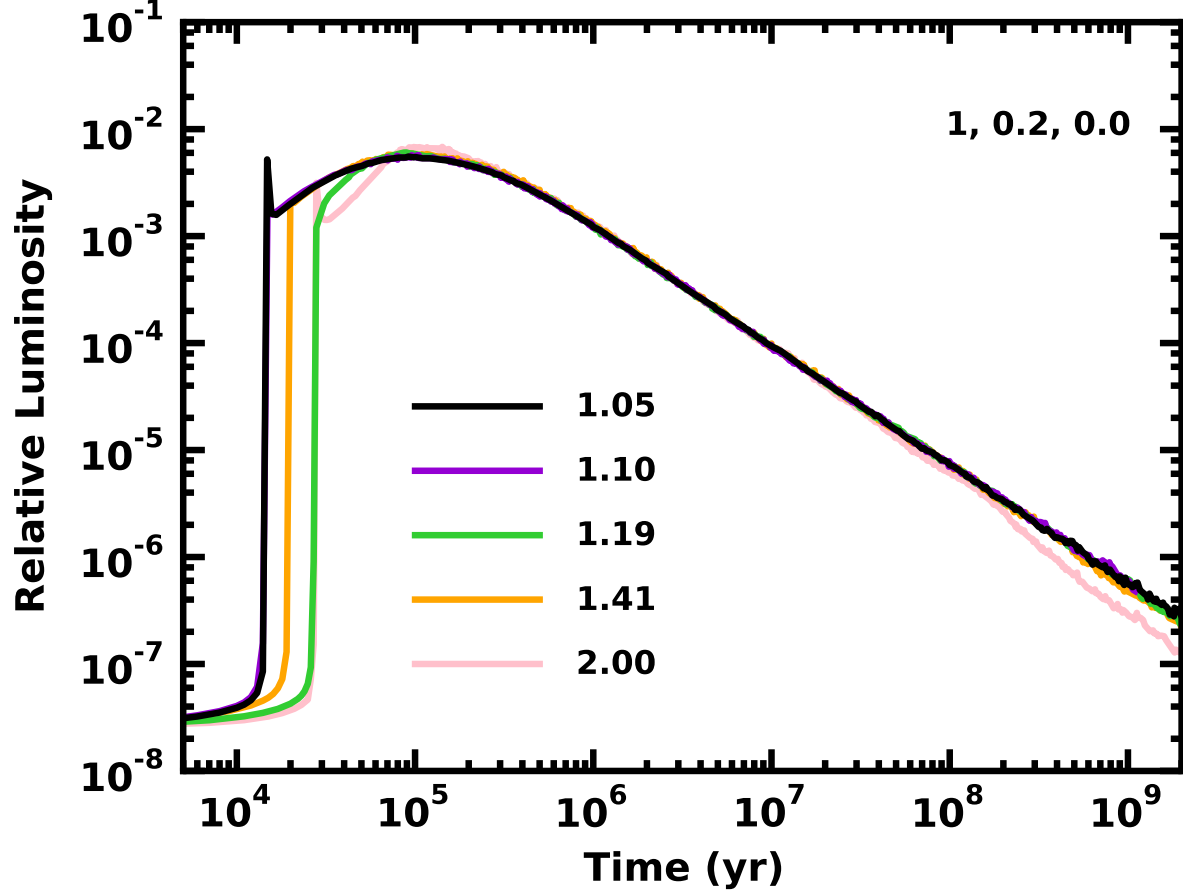


Fig. 28.— As in Fig. 27 for the dust luminosity  $L_d/L_\star$ . Rare destructive collisions among 100 km objects gradually produce debris. When the debris contains sufficient numbers of 1–100  $\mu\text{m}$  objects, the dust luminosity rises. For all calculations, the dust luminosity reaches a peak at 0.1 Myr and then declines roughly linearly with time.

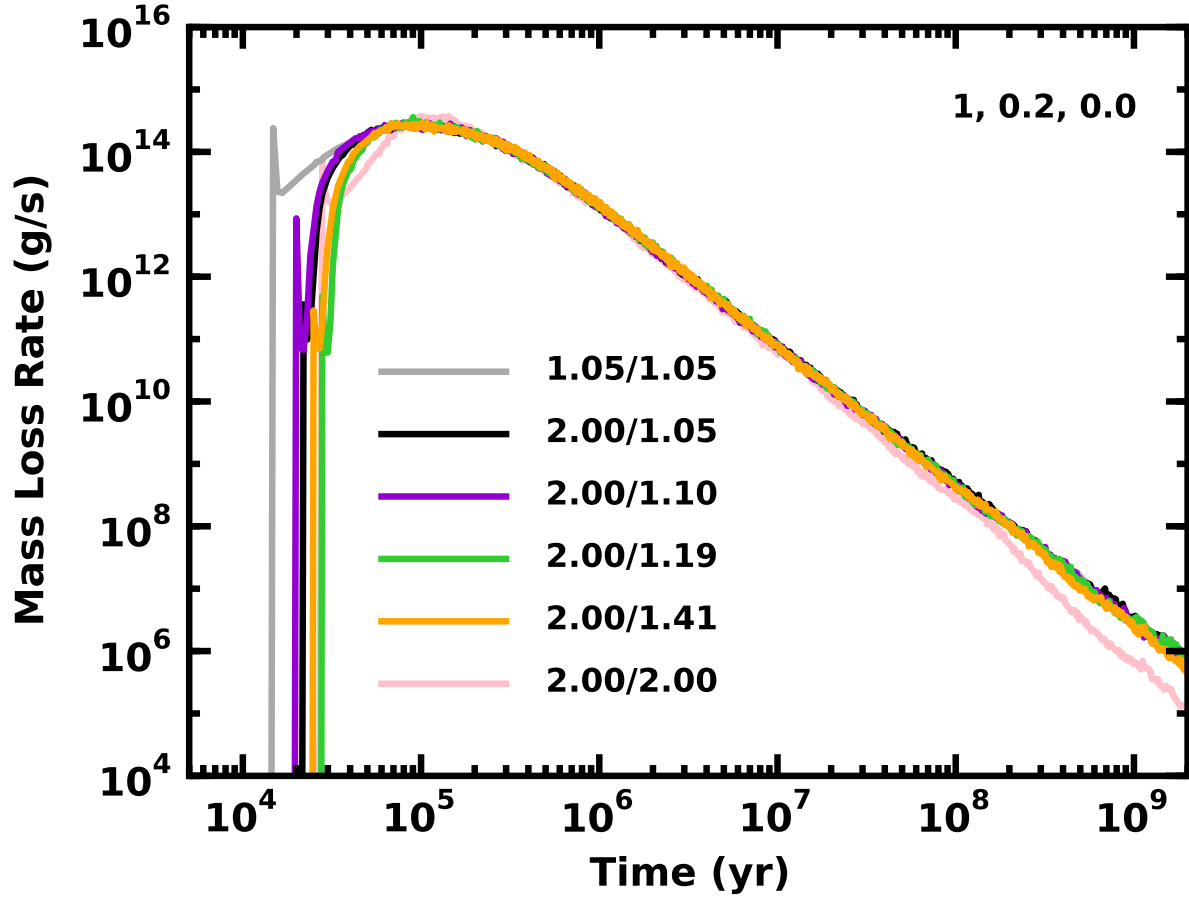


Fig. 29.— As in Fig. 27 for hybrid models where  $\delta$  varies with particle size. As indicated in the legend, we adopt one  $\delta$  for  $r \lesssim 0.2\text{--}0.4$  km and a smaller  $\delta$  for  $r \gtrsim 3\text{--}5$  km.

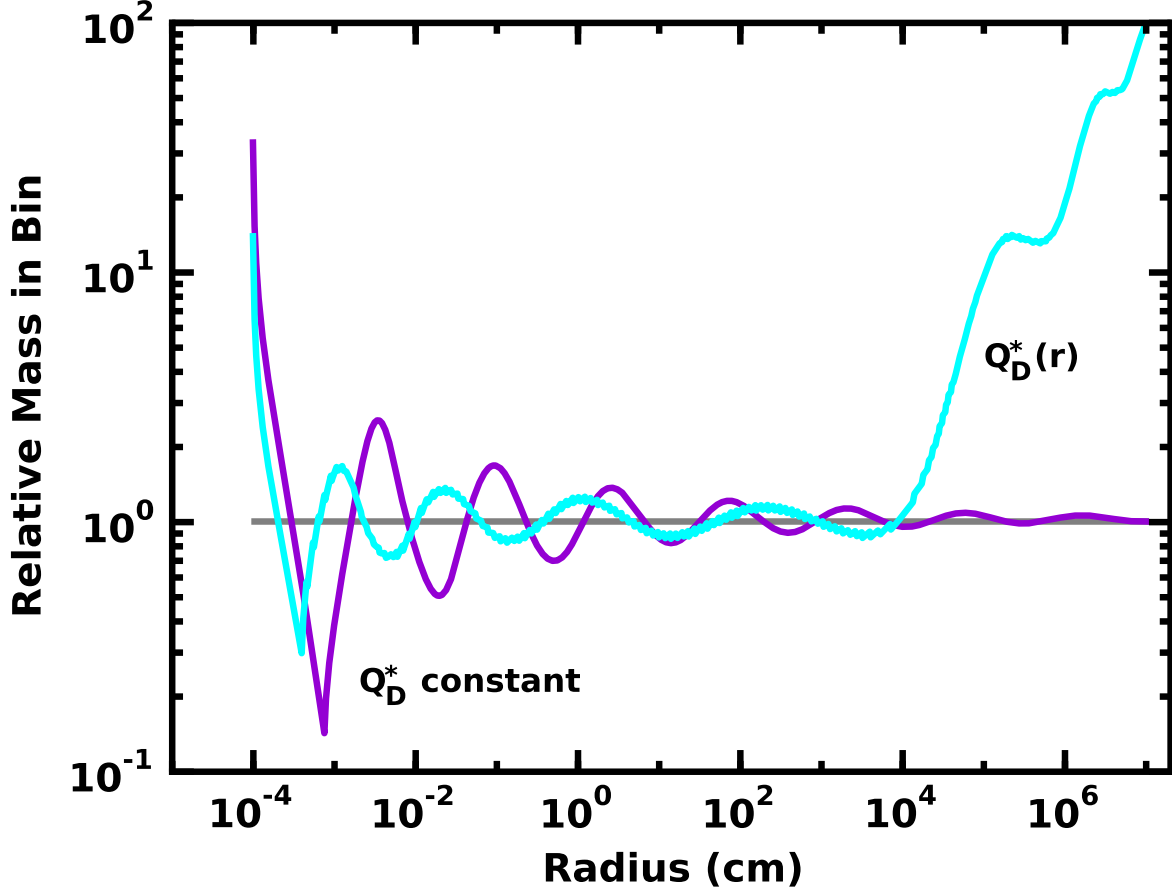


Fig. 30.— Relative mass distributions derived from the analytic model described by eqs. A1–A5 with  $v = 3 \text{ km s}^{-1}$ . The relative mass in each bin is  $M_k/r^{1/2}$  ( $Q_D^* = \text{constant}$ , violet curve) or  $M_k/r^{0.34}$  ( $Q_D^*(r)$ , cyan curve). Systems with  $Q_D^* = \text{constant}$  have size distributions with larger amplitude and longer wavelength waves than systems with  $Q_D^*(r)$ . When  $Q_D^*$  is a function of particle size, the change in slope at large sizes produces a corresponding change in the slope of the size distribution.